Towards ferromagnet/superconductor junctions on graphene

Dissertation zur Erlangung des
naturwissenschaftlichen Doktorgrades
der Julius-Maximilians-Universität Würzburg

vorgelegt von
Shijin Babu Pakkayil
aus vatakara, India

Würzburg, 2015

cc BY ND

Eingereicht am: ...

bei der Fakultät für Physik und Astronomie

1. Gutachter: PD. Dr. Charles Gould

2. Gutachter: Prof. Dr. Matthias Bode

3. Gutachter:

der Dissertation.

Vorsitzende(r) ...

1. Prüfer: PD. Dr. Charles Gould

2. Prüfer: Prof. Dr. Matthias Bode

3. Prüfer: Prof. Dr. Haye Hinrichsen

im Promotionskolloquium.

Tag des Promotionskolloquiums: ...

Doktorurkunde ausgehändigt am: ...

Contents

Zusammenfassung **1**

Summary **5**

1 Introduction **7**
1.1 Motivation . . . 7
1.2 Graphene . . . 8

2 Fabrication **11**
2.1 Introduction . . . 11
2.2 Graphene production . . . 11
2.3 Contacting graphene with ferromagnet . . . 13
2.4 Ferromagnet/superconductor junctions . . . 16
2.4.1 Fabrication process . . . 17
2.4.2 Challenges in fabrication . . . 20

3 Spin transport in graphene **25**
3.1 Introduction . . . 25
3.2 Spin of electron . . . 25
3.3 Magnetic materials . . . 26
3.3.1 Ferromagnetic materials and spontaneous magnetisation . . . 27
3.4 Magnetoresistance . . . 27
3.4.1 Giant magnetoresistance and Tunneling Mgnetoresistance . . . 29
3.5 Spin injection into semiconductors . . . 31
3.5.1 Conductance mismatch . . . 32
3.6 Spin injection to graphene . . . 32
3.7 Simple theory of spin transport in graphene . . . 36
3.7.1 Gate tunable spin transport . . . 39
3.8 Experimental results . . . 41
3.8.1 Spin injection using ALD grown Al_2O_3 tunnel barrier . . . 42
3.8.2 Spin valve device 03.26_S . . . 43
3.8.3 Spin valve device 07.30_S2 . . . 45
3.8.4 Spin valve 04.16_S and 04.18_S . . . 47
3.9 Spin injection using additional Ti seed layer . . . 49

3.9.1 Spin valve 01.24_S 50
3.9.2 Device 08.08_S1 51
3.10 Conclusion and Outlook 52

4 Ferromagnet-superconductor junctions on graphene 55
4.1 Introduction 55
4.2 Basics of superconductivity 55
4.3 Andreev reflection 57
4.3.1 Multiple Andreev reflection and Andreev bound states 59
4.4 Specular and retro reflections 60
4.5 Ferromagnet-superconductor junction 61
4.5.1 Crossed Andreev reflection 64
4.5.2 Spin imbalance 66

5 Characterisation of ferromagnet/superconductor junctions on graphene 71
5.1 Introduction 71
5.2 Josephson junction 72
5.2.1 150 nm long junction 74
5.2.2 200 nm junction 76
5.2.3 250 nm junction 77
5.3 Device 08.08_S1 77
5.4 Conclusion and outlook 85

6 Conclusion and Outlook 87

A Fabrication processes 89
A.1 Preparation of substrates 89
A.2 Contacting graphene with ferromagnet 89
A.3 Fabrication of ferromagnet-superconducting junctions 90

B Picture gallery 93
B.1 Ferromagnet-superconductor junctions on graphene 93
B.2 Other devices 95

Bibliography 106

Zusammenfassung

Seit A. Aspect *et al.* [1] in Experimenten an verschränkten Photonen eine Verletzung der Bellschen Ungleichung nachgewiesen haben, wird angestrebt dieses Experiment auch in einem Festkörpersystem durchzuführen. In einigen dieser Vorhaben wird die Verwendung von Supraleitern als Quelle für die verschränkten Elektronenpaare, sowie spin-sensitive Grenzflächen als Ersatz für die optischen Polarisatoren und Filter vorgeschlagen. Aufgrund ihrer langen Spin-Relaxationslängen bieten sich Halbleiter für die Umsetzung dieses Experimentes an. Im Gegensatz zu rein metallischen Systemen, in welchen dies bereits erfolgreich umgesetzt wurde, ist bisher noch von keiner Implementierung auf Halbleiterbasis berichtet worden. Die vorliegende Arbeit beschreibt die erfolgreiche Herstellung, sowie Charakterisierung von auf Graphen basierenden Ferromagnet/Supraleiter Hybrid-Strukturen.

Seit seiner Entdeckung in 2004 [2] haben die einzigartigen Eigenschaften von Graphen sowohl in der Wissenschaft als auch in der Industrie, ein gewaltiges Interesse hervorgerufen. Diese umfassen unter anderem eine sehr hohe Elektronenbeweglichkeit, eine hohe thermische und elektrische Leitfähigkeit, ein hohes Elastizitätsmodul und eine vollständige Impermeabelität gegenüber Flüssigkeiten und Gasen. Des Weiteren wird erwartet, dass Graphen aufgrund seiner schwachen Spin-Bahn-Kopplung lange Spin-Relaxationslängen und eine hohe Spin Lebensdauer aufweist. Basierend auf diesen Gründen, in Kombination mit dem steten Interesse an neuartigen Materialien und Bauelementen, um den hohen Ansprüchen an verbesserten und schnelleren Speicherbauelementen gerecht zu werden, hat sich Graphen zu einem brandneuen Materialsystem für Spintronik-Bauelemente entwickelt. Die erste Demonstration von Spininjektion und Spindetektion in Graphen wurde 2007 [3] realisiert. Seither ist die Verbesserung der Spin-Transport-Eigenschaften ein wichtiger Forschungsschwerpunkt.

Ein Teil dieser Arbeit beschreibt eine neu entwickelte Herstellungsmethode für ferromagnetische Kontakte auf Graphen. Die Besonderheit dieser Methode ist deren hohe Zuverlässigkeit und Erfolgsrate. Diese ist eine unabdingbare Bedingung für die erfolgreiche Kombination von ferromagnetischen und supraleitenden Kontakten zur Herstellung von F/S Hybridbauteilen auf Graphen-Basis.

Ein fundamentales Problem bei der Herstellung von ferromagnetischen Kontakten auf Graphen, wie auch auf jedem anderen beliebigen Halbleiter ist das sogenannte conductance mismatch [4]. Zur Lösung dieses Problems, welches den Fortschritt in diesem Gebiet für viele Jahre aufgehalten hat, wird zwischen die Grenzschicht von Ferromagnet und Graphen eine dünnen Al2O3 Schicht eingefügt. Diese isolierende Schicht wird mittels sogenannter Atomlagenabscheidung (eng. atomic layer depostion, ALD) hergestellt. Für einen besseren Wachstumsstart wird zunächst eine dünne Startschicht aus Ti aufgebracht. Diese Methode unterscheidet sich grundlegend von einer in der Literatur beschriebenen Methode [5], die für ein besseres Wachstum zunächst die vollständige Graphenoberfläche mit PTCA (3,4,9,10-perylene tetracarboxylicacid)) vorbehandelt. Diese Art von chemischer Vorbehandlung wird in unserem Prozess nicht angewendet.

Darüber hinaus übersteigt die erzielte Rate an erfolgreich hergestellten Proben den in der Literatur zu findenden Bestwert deutlich (30% [6]). Der zweite Teil der Arbeit beschreibt die Integration von supraleitenden Kontakten in den Herstellungsprozess, sowie weitere wichtige vorgenommene Verbesserungsmanahmen auf dem Weg zur Herstellung von Graphen basierenden Ferromagnet/Supraleiter Hybrid-Strukturen.

In Kapitel 4 werden die mittels des neuentwickelten Prozesses hergestellten Spin-Ventil-Strukturen, sowie eine einfache Theorie zum Spin-Transport in Graphen präsentiert. Einige der diskutierten Bauteile wurden mit einer Startschicht aus Ti (für die Atomlagenabscheidung), einige ohne diese zusätzliche Schicht hergestellt. Darüber hinaus wird der Einfluss der Anzahl an verwendeten ALD Zyklen auf die Performance der Bauteile diskutiert. Basierend auf diesen Ergebnissen wird auf die optimale Anzahl an Zyklen geschlossen. Bauteile die mit einer extra Schicht aus Ti hergestellt wurden zeigen hierbei eine deutlich höhere Reproduzierbarkeit hinsichtlich des Kontaktwiderstandes und der allgemeinen Performance. Des Weiteren lässt das Verhalten einer der ferromagnetischen Kontakte darauf schließen, dass es sich dabei um eine perfekte Tunnelbarriere handelt.

Kapitel 5 diskutiert zum gröten Teil die Messergebnisse die an einem Bauteil bestehend aus vier ferromagnetischen und vier supraleitenden Kontakten erzielt wurden. Die Anordnung der einzelnen Kontakte ist so gewählt, dass mehrere Ferromagnet/Supraleiter Hybridstrukturen gebildet werden. Des Weiteren ermöglicht die gewählte Anordnung die unabhängige überprüfung der Funktionalität der einzelnen Komponenten in Form von reinen Spin-Ventilen bzw. Josephson-Kontakten. Transportmessungen an den Josephson-Kontakten zeigen einen Verlauf des Leitwertes unterhalb der Bandlücke der supraleitenden Kontakte, welcher charakteristisch ist für das Auftreten von Vielfach-Andreev-Reflexionen. Dies ist als Indiz für eine hohe Transparenz der Grenzschicht zwischen Supraleiter und Graphen zu werten. Das in diesem Bauteil ermittelte untere Limit der supraleitenden Kohärenzlänge (L) ist größer als der Abstand zweier benachbarter supraleitender, bzw. ferromagnetischer Kontakte (100 nm) und erfüllt somit die Grundvoraussetzung um auftre-

tende Wechselwirkungen zwischen diesen beiden zu beobachten.

Die Funktionalität aller Kontakte wird durch sogenannte nicht-lokale Messungen an Spin-Ventilen bestätigt. Hierbei wird zudem deren Effizienz zu ca. 10-12% abgeschätzt. Messungen in einer quasi nicht-lokalen Geometrie, bestehenden aus Ferromagnet/Graphen/Supraleiter/Graphen/Ferromagnet (F/G/S/G/F) weien eine Struktur mit zwei Peaks auf. Dieses Ergebnis deutet darauf hin, dass ein Ungleichgewicht in der Quasiteilchen Zustandsdichte des Supraleiters vorliegt. Das Verschwinden dieses Verhaltens oberhalb der Sprungtemperatur des Supraleiters ist als ein weiterer Hinweis darauf zu werten, dass dieses Ergebnis auf den supraleitenden Zustand der Kontakte zurückzuführen ist. Der zu beobachtende Anstieg der Amplitude der beiden Peaks, ist wahrscheinlich auf die größere Anzahl an diffundierenden Spins, bedingt durch die gröeren AC Ströme, zurückzuführen. Ein Umdrehen der Magnetisierungsrichtung eines der Ferromagneten (Injektor oder Detektor), hat entgegen der Erwartungen keinen Einfluss auf die Position der beiden Peaks. Es sind daher weitere Messungen an ähnlichen Proben durchzuführen. Diese sollten vorzugsweise bei der Basistemperatur eines Mischungskryostaten vorgenommen werden, um eindeutig die Existenz eines Ungleichgewichts in der Besetzungzahl der Spinzustände im Supraleiter nachzuweisen.

Summary

Ever since A. Aspect *et al.* [1] performed the famous 1982 experiment to prove the violation of Bell's inequality, there have been suggestions to conduct the same experiment in a solid state system. Some of those proposals involve superconductors as the source of entangled electron pair and spin depended interfaces as the optical analogue of polariser/filter. Semiconductors can serve as the best medium for such an experiment due to their long relaxation lengths. So far there are no reports on a ferromagnet/superconductor junctions on a semiconductor even though such junctions has been successfully realised in metallic systems. This thesis reports the successful fabrication of ferromagnet/superconductor junction along with characterising measurements in a perfectly two dimensional zero-gap semiconductor known as graphene.

Since it's discovery in 2004 [2], graphene has attracted prodigious interest from both academia and industry due to it's inimitable physical properties: very high mobility, high thermal and electrical conductivity, a high Young's modulus and impermeability. Graphene is also expected to have very long spin relaxation length and high spin life time because of it's low spin orbit coupling. For this reason and since researchers are are always looking for novel materials and devices to comply with the high demands for better and faster data storage devices, graphene has emanated as a brand new material system for spin based devices. The very first spin injection and detection in graphene was realised in 2007 [3] and ever since, the focal point of the research has been to improve the spin transport properties. A part of this thesis discusses a new fabrication recipe which has a high yield for successfully contacting graphene with a ferromagnet. A high starting yield for ferromagnetic contacts is a irremissible condition for combining superconducting contacts to the device to fabricate ferromagnet/superconductor junctions.

Any fabrication recipe to contact graphene or any other semiconductor with a ferromagnet has to overcome one important problem known as "Conductance mismatch" [4]. To solve the conductance mismatch problem, which had stalled the injection of spin polarised electrons to a semiconductor for many years, in our fabrication method, a thin Al_2O_3 layer is introduced between the ferromagnet and graphene. The insulating layer is grown using Atomic layer deposition (ALD) with the help of a thin Ti seed layer. Unlike the previously reported method [5], which treats the entire graphene flake with PTCA

(3,4,9,10-perylene tetracarboxylic acid) prior to the ALD process, no such chemical treatment occurs in our fabrication process. Also, the yield of successful devices are higher than the highest yield reported so far (∼30% [6]). The later part of the thesis discusses how this fabrication recipe is further developed to contact graphene with superconducting contacts to produce ferromagnet/superconductor junctions on graphene.

The successful spin valve devices produced using the new fabrication process are discussed in chapter 4 along with a simple theory of spin transport in graphene. Some of the spin valve devices discussed are fabricated with the help of Ti seed layer (for growing Al_2O_3) and some of them are without. Also, measurement results on devices with varying number of ALD cycles are shown and discussed which helps to decide the optimum number of ALD cycles needed for the best yield and performance. The devices made using Ti seed layer shows better consistency in terms of contact resistances and device performance. Also, ferromagnetic contacts from one device showed perfect tunnel barrier behaviour.

Chapter 5 mainly discusses the results of the measurements done on a device which has 4 ferromagnetic contacts and 4 superconducting contacts arranged in a fashion that it forms multiple ferromagnet/superconductor junctions on graphene. Lateral spin valves and Josephson junctions are also part of the design which makes it possible to verify the quality of both type of contacts independently. The Josephson junction formed by two superconducting contacts and graphene between them shows several subgap conductance peaks corresponding to multiple Andreev reflections (MAR) taking place between the superconducting contacts. The observation of MAR shows that the superconductor has a good transparent interface with the graphene. The lower limit of the calculated superconducting coherence length (L_ϕ) in graphene is higher than the separation between the ferromagnet and the superconductor (100 nm), which is a necessary condition to observe interaction between the ferromagnet and the superconductor. Nonlocal spin valve measurements show that all four ferromagnetic contacts are spin sensitive and have a spin injection/detection efficiency of 10-12 %. Three terminal pseudo nonlocal measurements done on a ferromagnet/graphene/superconductor/graphene/ferromagnet (F/G/S/G/F) junction shows a two peak structure which suggests the occurrence of spin imbalance in the quasiparticle density of states in the superconductor. The measurements also show the disappearance of the two peak structure whenever the superconductor becomes normal. The amplitude of the peaks seems to increase with increasing ac bias current which is probably due to the higher number of diffusing spins. Reversing the magnetisation direction of one of the ferromagnet (injector or detector) however did not reverse the position of the peaks which is unusual. So further measurements need to be done on similar devices preferably at the base temperature of a dilution refrigerator to conclusively prove the existence of spin imbalance in the superconductor.

Chapter 1

Introduction

1.1 Motivation

In 1935, Einstein, B. Podolsky and N. Rosen published an article titled "Can Quantum-Mechanical Description of Physical Reality Be Considered Complete" in which they argued that the inability of quantum mechanics to give a "locally realistic" picture of the physical world is due to it's incompleteness [7]. In their article they preposed a thought experiment which later became known as the "EPR paradox" and they suggested that the quantum mechanical interpretation of the paradox has to involve a"spooky action at distance". The thought experiment involves measuring the spin state of a previously entangled particles. If one one were to separate such a two particle entangled system to arbitrary distances and measure the spin state of one of the particle, then he or she can automatically predict with 100% certainty the outcome of the same measurement done on the second particle. The paper suggested that the quantum mechanical interpretation of the physical world fails to deduce such an information due to it's incompleteness. It was John Stewart Bell in his famous paper "On the Einstein Podolsky Rosen paradox" [8], who gave an experimentally testable formalism of the EPR paradox which is later known as "Bell's inequality". The experiment to test the Bell's theorem was conducted in 1982 using entangled photons [1]. The results were in excellent agreement with quantum mechanical predictions and showed that nature is in fact non-local.

After the 1982 experiment, there has been suggestion to how the experiment can be conducted in a solid state system. One of the important part of the experiment is developing a source for the entangled particles. In condensed matter, superconductors are an excellent source for entangled pairs of electrons since inside the superconducting gap two electrons with opposite spins couple each other to forms an entangled pair known as "Cooper pair". Some of the proposals to witness Bell's inequality in condensed matter system involves a superconductor as the source of entangled pair of electrons and spin active interfaces as the optical analogue for a polariser. Due to the long relaxation lengths and the ability to control the carrier density, semiconductors are more favourable choice for

such a solid state entangler. So far there has been no report on a successful implementation of ferromagnet-superconductor junction on any semiconductor. This thesis reports a successful implementation of ferromagnetic and superconducting contacts into a zero-gap, two dimensional semiconductor known as graphene.

1.2 Graphene

Graphene, the first two dimensional material experimentally realised in 2004 [2] is an allotrope of carbon. Graphene was known to have extraordinary electronic properties for over sixty years but it was believed to be only an "academic material" and not to exist freely in nature. Graphene has perfect two dimensional honeycomb lattice and is the basic building block for all graphite materials like 0D fullerenes, 1D nanotubes and 3D graphite. Some of the exceptional properties of graphene includes very high mobility (up to 10^5cm^2/Vs [9]), high thermal conductivity (∼3000 W/mK [10]), high Young's modulus (∼ 1TPa [11]), impermeability to all gases [12], and very high electrical conductivity.

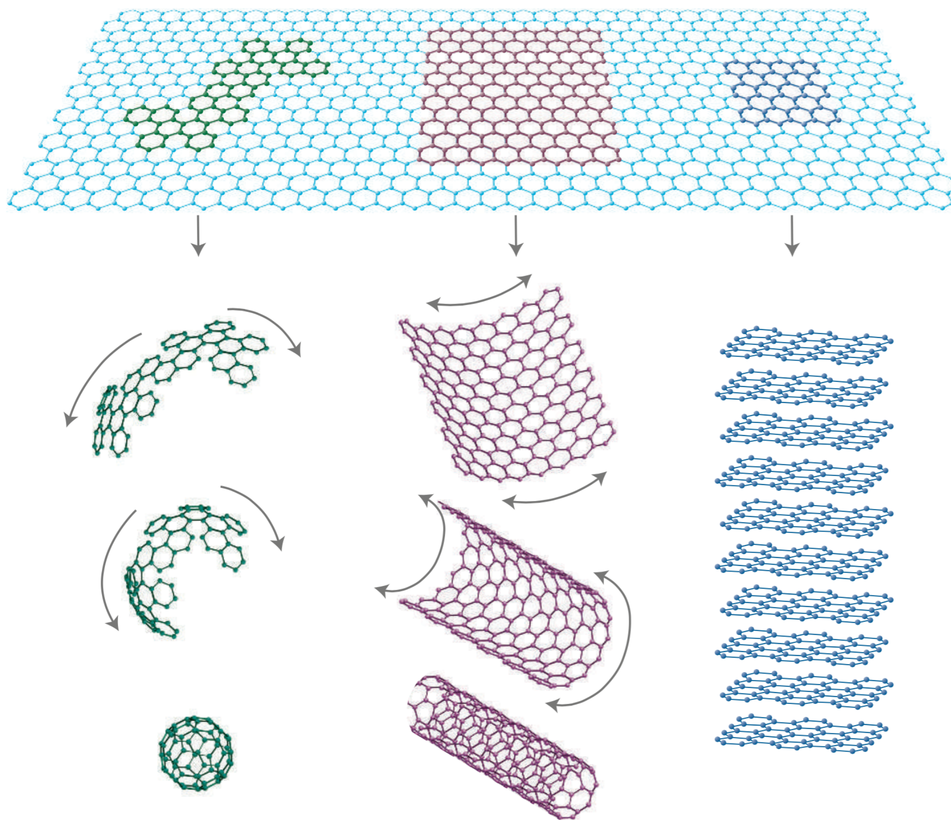

Figure 1.1: Single layer graphene is the basic building blocks for 0D fullerenes, 1D nanotubes or when stacked perpenticular, 3D graphite. Figure taken from [13]

The carbon atom has an atomic number of 6 and hence has the following electronic configuration: $1s^2 2s^2 2p^2$. In graphene the carbon atoms undergo sp^2 hybridisation to form 3 hybridised orbitals and one pure p_z orbital. The sp^2 hybridised orbitals arrange itself in the xy plane with an angle of 120° between them while the p_z orbital stays perpendicular to the xy plane and is responsible for the conduction electron. Due to this 120° between the orbitals in plane, graphene has a honeycomb lattice structure. The structure of graphene can be interpreted as a triangular lattice with each unit cell containing two carbon atoms. The two lattice vectors are

$$a_1 = \frac{a}{2}(3, \sqrt{3}) \qquad a_2 = \frac{a}{2}(3, \sqrt{-3}) \tag{1.1}$$

Where a is the distance between the adjacent carbon atoms (0.142 nm). The two inequivalent corners of the hexagonal Brillouin zone $K = (2\pi/a, 2\pi/3\sqrt{3}a)$ and $K' = (2\pi/a, -2\pi/3\sqrt{3}a)$ are called Dirac points (Figure 1.2).

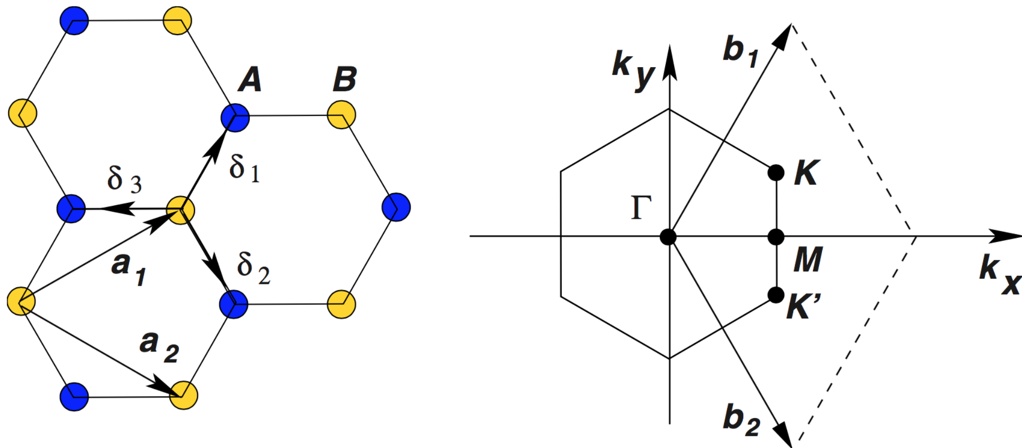

Figure 1.2: (left) The honeycomb lattice structure of graphene. a_1 and a_2 are the two lattice vectors. δ_1, δ_2 and δ_3 represents the nearest neibhour vectors. The lattice is shown as two interpenetrating triangular sublattices made of A and B. (right) Brillouin zone of the honeycomb lattice. Vectors b_1 and b_2 represent the two reciprocal lattice vectors. K and K' show the two Dirac points. Taken from [14].

The band structure of single layer graphene is shown in Figure 1.3. The conduction and valance band touch each other at the corners of Brillouin zone. So graphene is called as a zero-gap semiconductor. The dispersion relation close to the Dirac point has the form $E = \hbar \mathrm{V_F}|k|$ where $\mathrm{V_F}$ is the fermi velocity and have the value $\sim 10^8$ m/s in the case of graphene. Also unlike other materials, the fermi velocity in graphene is constant and does not depend on momentum or energy. A linear dispersion relation with zero band gap is a striking feature of graphene and all the physics discussed in thesis happens at the

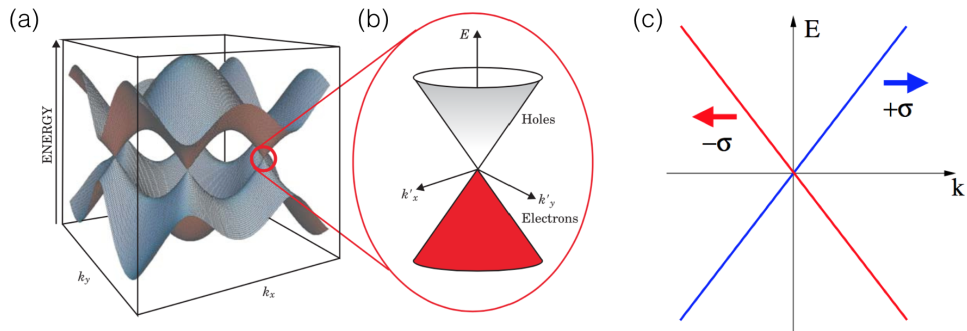

Figure 1.3: (a)Band structure of monolayer graphene. (b) Magnified band structure near the Dirac point. (c) Lenear dispersion relation of graphene carresponding to $E = \hbar V_F|k|$. Taken from [15].

vicinity of the Dirac point. The existence of two Dirac points (two valleys) imply that the valley degeneracy has to be considered during a transport experiment. In the absence of inter-valley scattering, this means adding a degeneracy factor $g_v = 2$ to the calculations.

Chapter 2

Fabrication

2.1 Introduction

This chapter discusses the production and fabrication techniques used in this thesis to produce graphene based microscopic devices. There are multiple ways to produce single layer graphene out of which the most important methods are mechanical exfoliation, chemical vapour deposition (CVD) and by synthesis of silicon carbide (S_iC) wafer. Large area graphene layers, more than a square meters has been grown using CVD [16]. Even though this method is very suitable for industrial applications, there are drawbacks. One is that the graphene layers are normally grown on top of metallic substrates and to fabricate devices, graphene needs to be transferred to non-conducting substrates which is a difficult task. Another one is the low mobility of graphene layers grown using CVD method. The highest mobility measured on CVD grown graphene is only around 37,000 cm^2/Vs [17] which is achieved by placing graphene on top of boron nitride substrate. On the other hand, mechanically exfoliated graphene shows the best quality so far reaching mobilities up to 10^6 cm^2/Vs [18]. Even though the single layer graphene obtained through mechanical exfoliation are smaller (< 1000 μm), compared to CVD grown graphene, the high structural quality makes it best candidate for research purposes.

2.2 Graphene production

All devices discussed in this thesis are made using mechanically exfoliated graphene. To produce graphene, a freshly prepared scotch tape is put on top of an HOPG graphite block to get graphite layers on the tape. Then this thick layer of graphene is made thinner by opening and closing the tape several times. Once appropriately thin graphite layer is found on the tape, it is pressed on a freshly prepared clean SiO_2/Si^{++} substrate with graphene facing the S_iO_2 side of the substrate. The substrate is then looked under an optical microscope to find and map the single graphene layers. Even though graphene is almost transparent for visible light by allowing 97.7 % of the light to pass through [19],

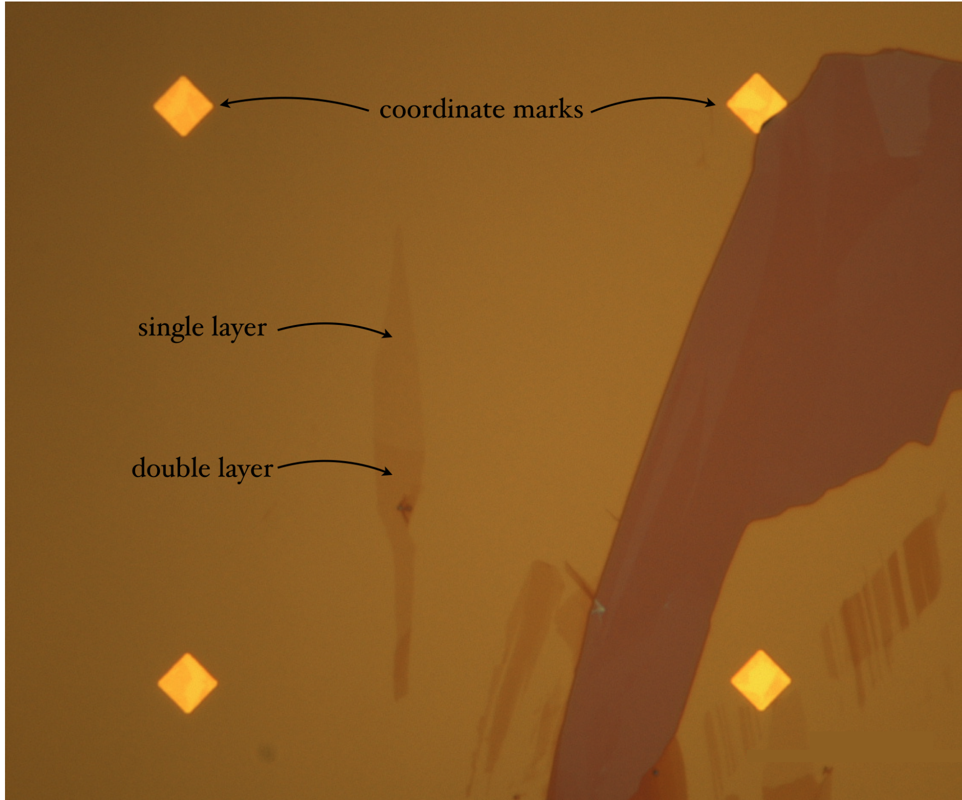

Figure 2.1: Single and double layer graphene on SiO_2/Si^{++} substrate. The width of the coordinate box is 5 μm.

upon placing on adequately thick substrate, single and double layer graphene can be distinguished. The substrate has to be prepared prior to this process which involves one step of photolithography in which Ti/Au coordinate marks are placed on the substrate. Coordinate marks are necessary to locate and map the graphene layers found using optical microscope. The preparation of the substrate starts with cutting S_i/S_iO_2 wafer in to 1cm $\times$ 1cm pieces using diamond edged cutter. The Si layer is highly "p" doped and serves as back gate during measurements. The thickness of the S_iO_2, which in our case is 285 nm, is very important since the contrast of different graphene layers depend on the thickness of S_iO_2 [13, 20]. After cutting the substrate, they are cleaned using ultrasonic agitation while immersed in acetone. Afterwards carefully designed coordinate system is printed on the substrate using photolithography and metal evaporation (details are given in appendix). After lift off, substrates are first cleaned in warm (50 °) acetone for about half an hour and then by oxygen plasma. It is important that whenever a substrate is taken out of acetone, it is flushed with iso-propanol before the acetone evaporates since evaporation of acetone may leave residues on the substrate. Since iso-propanol evaporates more slowly than acetone it can be removed using a nitrogen gun (high pressure nitrogen gas). After cleaning the substrates in oxygen plasma, the substrates are kept on hot plate at 180 ° for 15 minutes to remove any volatile contaminants. Figure 2.1 shows single

and double layer graphene. With the increasing number of graphene layers, the colour of graphene layers changes to pink and then to blue.

After locating the graphene layers on the substrate, it's exact coordinates relative to the Ti/Au marks are determined using graphic softwares like CorelDraw. These coordinates can be used to draw the geometrical shape of the graphene layer in the lithography patterning software. Afterwards, the desired design can be drawn using the software and corresponding fabrication processes are started.

2.3 Contacting graphene with ferromagnet

One of the main challenges in contacting graphene with ferromagnet is in overcoming conductance mismatch problem. In simple terms, the difference in carrier density of graphene and metallic ferromagnets like cobalt, iron, permalloy etc, damages the spin injection/detection efficiency of spin valve devices considerably, if the graphene is contacted by ferromagnets transparently. The solution to the problem is straight forward, which is to place a thin tunnel barrier between the graphene and ferromagnet. The method chosen in our case to grow thin insulator is atomic layer deposition (ALD). The ALD uses, in general, two chemicals known as precursors in gaseous state to react with the surface of the material in question one at a time in succession to grow thin oxide layers. Once both precursors have reacted in sequence, it is called one complete cycle. Due to the self limiting nature of the chemical reaction, it takes two or more cycles to produce one continuous monolayer. This makes ALD well suited for situations where sub-nanometer control of the insulating layer is desired. In our case, the insulator chosen is Al_2O_3 and the precursors used are $C_6H_{18}Al_2$ (tri-methyl aluminium) and H_2O (in gaseous state). But growing thin Al_2O_3 layer on graphene is not straight forward. Due to the inert nature of graphene and the absence of dangling bonds, the usual metal oxides can not be grown on pristine graphene [21]. This was also the case in our experiment when we tried to grow Al_2O_3 on freshly prepared graphene. The key to solve this problem is to functionalise the graphene surface using other chemicals [5, 21]. But to our surprise, unlike pristine graphene, graphene undergone e-beam exposure and development, seems to support the growth of Al_2O_3 (using ALD), partially. This accidental, un-intended functionalisation can be due to e-beam exposure, PMMA (poly-methyl methacrylate) residues, or developer residues. Nevertheless, many devices have been made successfully by making use of this process. But over the time this uncontrollable functionalisation of the graphene surface found to be unreliable and decision was made to make the functionalisation intentional and controllable by depositing a thin Ti seed layer on graphene prior to the ALD growth.

In practice, lateral spin valve devices are fabricated as follows. First, as explained in the beginning of this chapter, single graphene layers are identified using optical microscope and mapped with the help of coordinate marks on the substrate. Afterwards, PMMA resist (ARP 672.03, 950K, 3% anisol) is spin coated on the substrate at 3000 rpm and

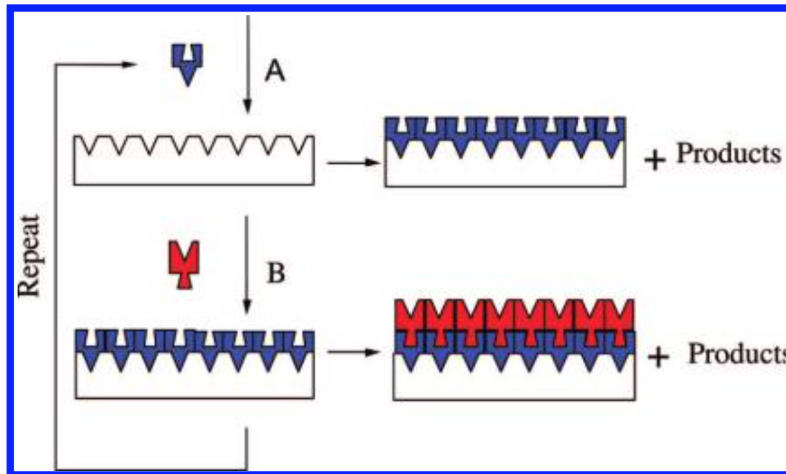

Figure 2.2: Schematic picture of ALD growth process showing the self limiting nature of the chemical reaction. 'A' and 'B' represents the two precursors and the process is repeated untill desired thickness is acheived. Figure taken from [22].

the substrates are baked at 180 °C for 2 minutes. The design of the contacts are then exposed on the PMMA using electron beam lithography (EBL). The samples are later developed using H_2O/C_3H_7OH (1:3) mixture. Here is where the difference in fabrication of intentionally functionalised and accidentally functionalised spin valve devices occur. Unlike the earlier devices with no Ti seed layer which were taken directly to ALD machine after developing for growing Al_2O_3, the later devices are taken to an e-beam deposition system, where 2 Å of Ti is deposited and oxidised at 100 mbar for 10 minutes. After the deposition of Ti, samples are taken to ALD system and the vacuum is broken. Prior to the actual growth of Al_2O_3, a "blank" (without any samples inside) process is run to make sure the chamber is free of any contaminants from previous growth since different types of oxides are deposited using our ALD system. After the fake process, the sample is placed in ALD and 9 cycles thick Al_2O_3 is grown at $80°C$ (details of the process are given in the appendix). Figure 2.3 shows the scanning electron microscope (SEM) images of Al_2O_3 on functionalised (with Ti seed layer) and un-functionalised graphene surface. The difference in surface profile is also visible in the yield of successful devices. After the ALD growth, the samples are immediately taken to an e-beam deposition system where 50 nm Co and 10 nm Au are subsequently deposited. The purpose of the Au layer deposited on top is to reduce the oxidation of the Co. Afterwards lift off is done in hot acetone (50 $°C$ for 15 minutes). In the second step of e-beam lithography, large bonding pads (100 μm $\times$ 100 μm) and the leads which connect them to the contacts are fabricated. For this, after the first lift off process, the same resist used for the previous lithography step is coated with the same parameters but the process is repeated twice to produce a thicker coating ($\sim$ 240 nm). After the lithography process and subsequent developing, 3 nm Ti and 120 nm Au are subsequently deposited. Following the lift off, the sample is cleaned in

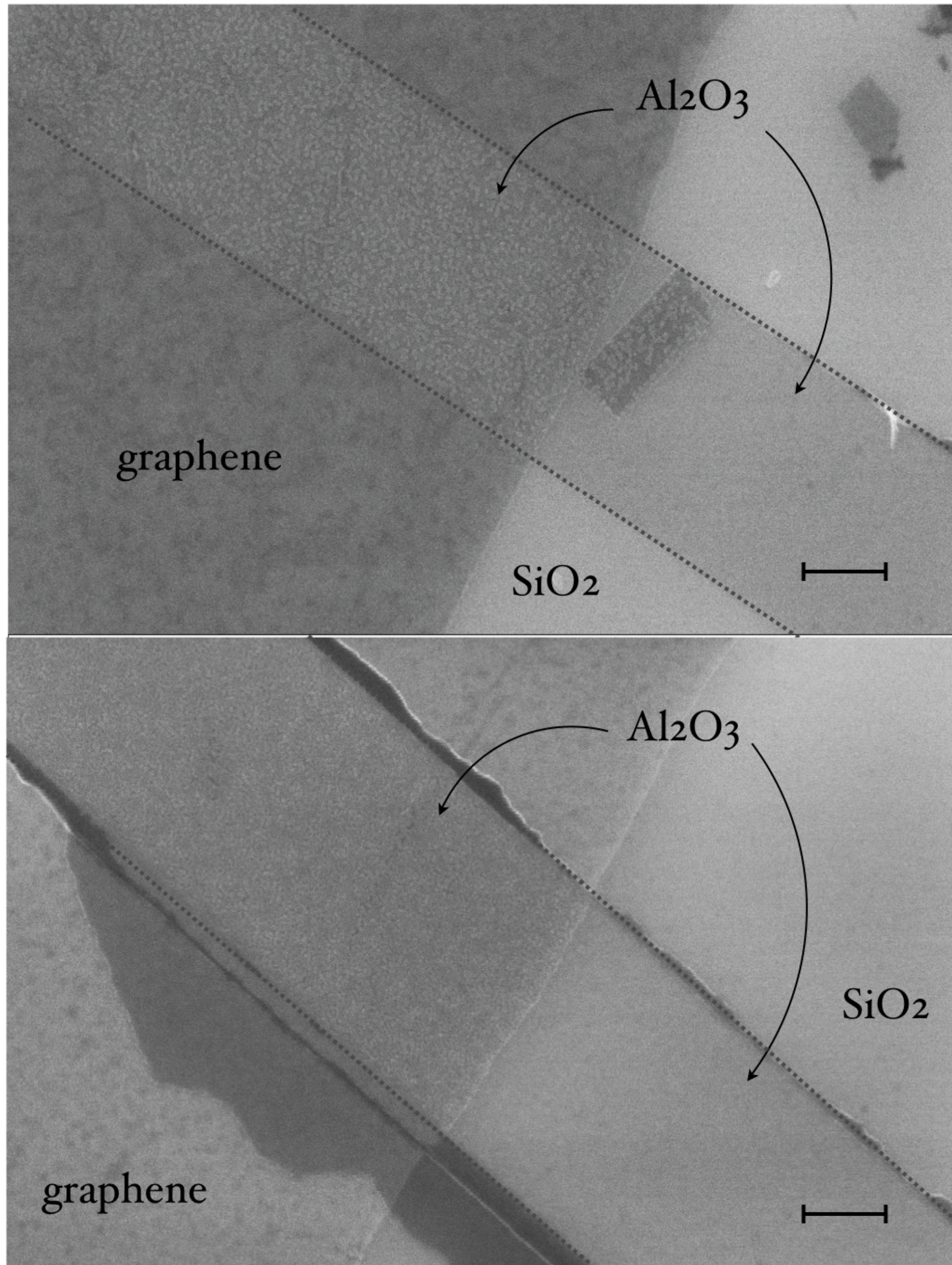

Figure 2.3: (top) Figure showing surface profile of ALD grown Al_2O_3 on graphene without Ti seed layer. The stripes are desgined by e-beam lithography and the dotted lines show the boundary. Al_2O_3 on graphene seems to form islands or grains compared to the homogeneous layer seen on S_iO_2. (bottom) Al_2O_3 grown on graphene with Ti seed layer. The Al_2O_3 layer is much more homogeneous and closely packed compared to the one without Ti seed layer. Scale bar is 300 nm.

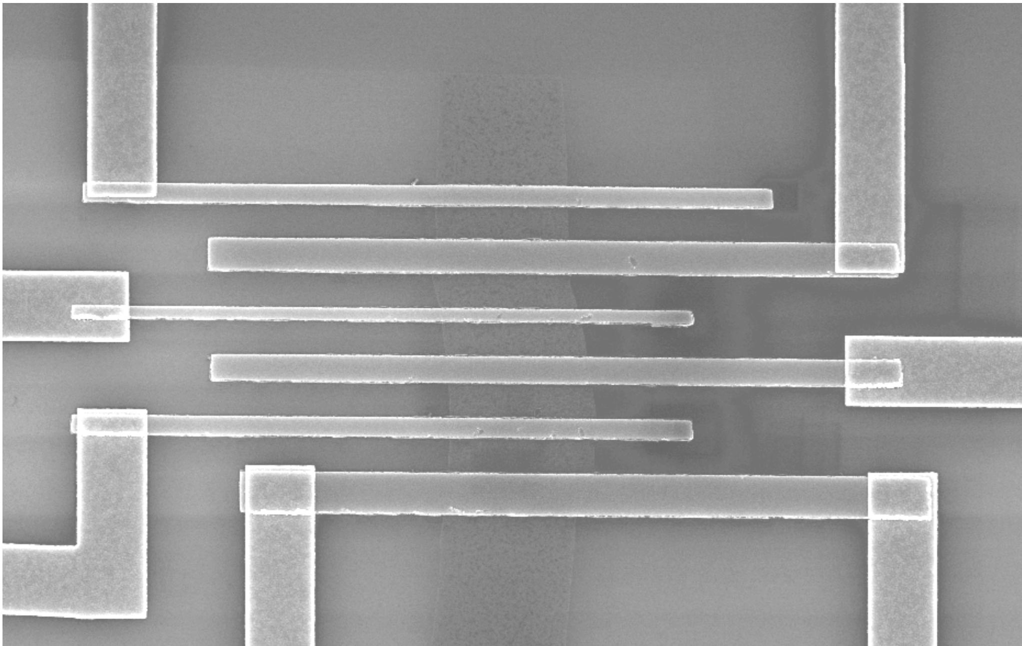

Figure 2.4: SEM image of a lateral spin valve device. The width of the contacts from top to bottom are 300 nm, 500 nm, 200 nm, 400 nm, 300 nm, 600 nm. Note that only the horizondal contacts are ferromagnetic. The connecting leads are made of Ti/Au.

NEP (n-ethyl-2-pyrrolidone) for an hour at 80 °C. Later, the sample is taken out of NEP by gently spraying isopropanol to eliminate any NEP residues on the substrate. Cleaned samples are then glued into chip carriers using electrically conducting silver glue with the silver glue connecting the edge of the substrate and the bottom of the chip carrier. The chip carrier is then heated at 180 °C for two minutes to harden the glue. This way of glueing makes sure that the highly doped silicon substrate can be used as a back gate later when the device is characterised.

2.4 Ferromagnet/superconductor junctions

After successfully developing recipe with high yield (∼50 %) for contacting graphene with ferromagnets, the process is further developed to incorporate superconducting contacts to the device. The basic design of the device is shown in Figure 2.5. In general all devices fabricated have four ferromagnetic contacts with different widths (200 nm-600 nm) and four superconducting contacts having the same width (200 nm). Some of the devices fabricated also have an extra Ti/Au normal contact for additional characterisation. The design shown in the figure is the result of three fundamental points. First, the ability of ferromagnetic contacts to inject/detect spin current should be independently testable. Placing contacts F1, F2 and F3, F4 adjacent to each other make it possible

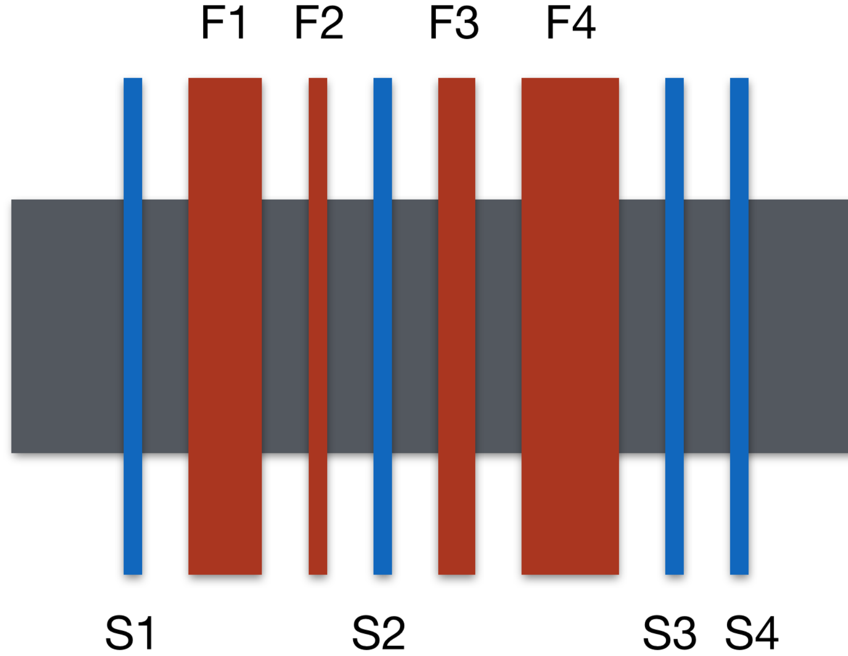

Figure 2.5: Basic design of the F/S device. The part which is painted in grey represents graphene. The four ferromagnetic contacts F1, F2, F3 and F4 have different widths so that their magnetisation direction can be independantly adjusted. The four superconducting contatcs S1, S2, S3 and S4 have the same width of 200 nm and are connected by two leads which are necessary for chrecterisation of the device.

to qualitatively check the efficiency of the contacts by performing nonlocal spin valve measurements. The same argument also applies to the superconducting contacts. Contacts S3 and S4, along with the graphene between them forms a Josephson junction with which a qualitative measure of the transparency of the contacts can be checked in a differential conductance measurement. Also for this purpose, all the superconducting contacts are connected by two leads to avoid lead resistance during measurements. Finally the device should form ferromagnet/graphene/ferromagnet (F/G/S) and ferromagnet/graphene/superconductor/graphene/ferromagnet (F/G/S/G/F) junctions to probe the local and nonlocal effects arising from injecting spin polarised current in to a superconductor. Over the time, many devices are fabricated and characterised with different contact separation distances.

2.4.1 Fabrication process

The fabrication process of Ferromagnet/Superconductor junction on graphene (F/S) starts with contacting the graphene with ferromagnetic contacts. It is important to place the

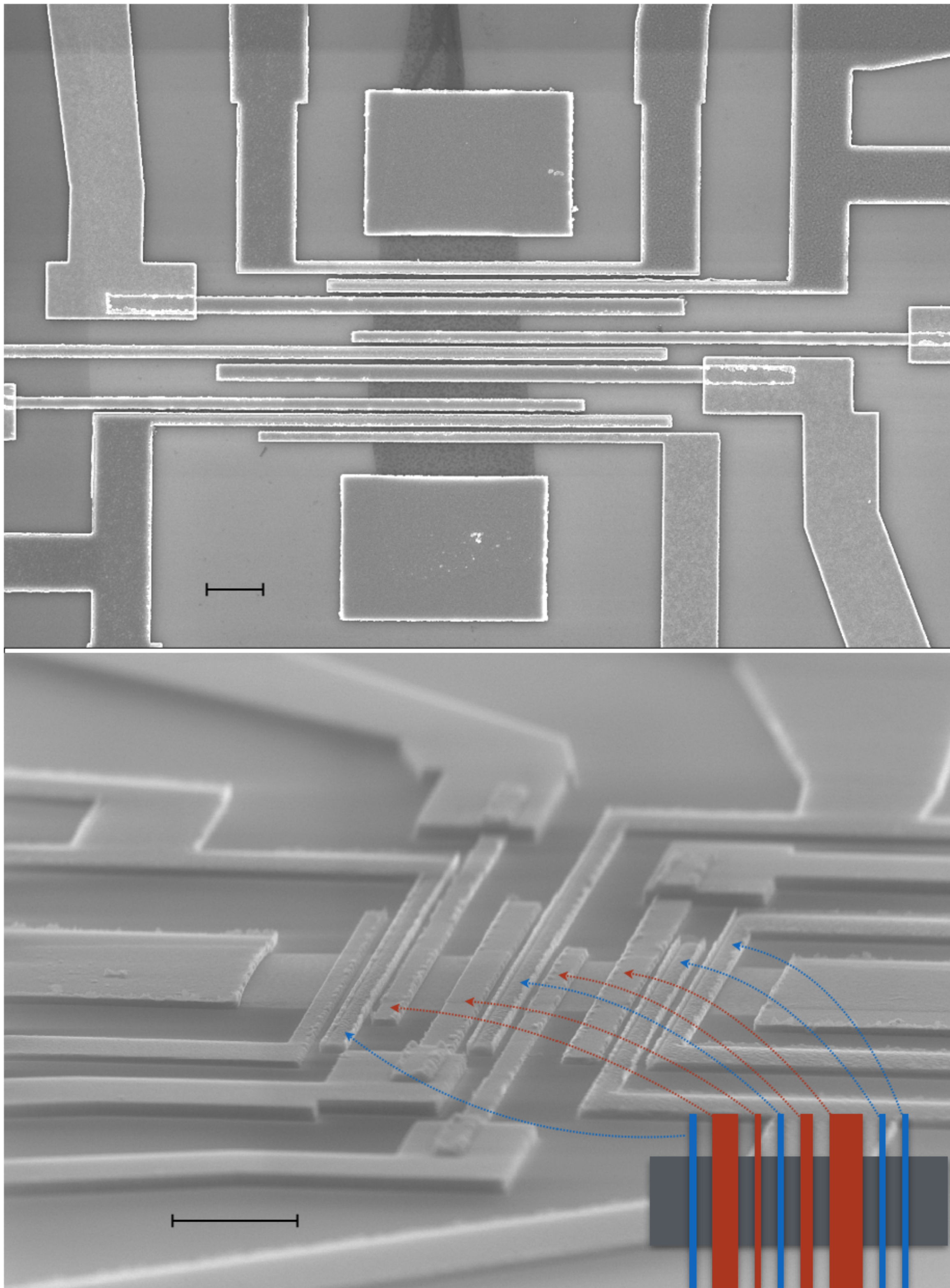

Figure 2.6: SEM image of an F/S device showing top and side views. The left most contact in the bottom image is a normal contact. The scale bar for both images are 1 μm.

ferromagnetic contacts in the first fabrication step since it has been found that, if it is not done so, the yield of the working ferromagnetic contacts goes down considerably. This could be because if other fabrication processes are performed prior to placing ferromagnetic contacts, the contaminants and residues from resists can have adverse effects on the processes involved in contacting graphene with ferromagnet, especially during the ALD process. Also for spin valve devices or F/S devices, the preferred width of graphene flake is 1-5 μm, since this reduces the chance of graphene rolling up and if there are no other flakes nearby, let us to reduce an etching step involved in the process. After placing the ferromagnetic contacts, they are not immediately connected to the bonding pads like in the case of spin valve devices. Instead leads connecting the contacts and bonding pads are done after all types of contacts (ferromagnetic, superconducting and in some case a normal contact) are placed. In the second step of lithography, e-beam exposure and developing is done using the same resist and developer to place the superconducting contacts. Afterwards, the sample is transferred to a dc sputtering system. In the sputtering system, 5 nm of Titanium, 65 nm of Niobium, 10 nm of Aluminium and 10 nm of Ruthenium are sequentially sputtered (parameters for sputtering are given in appendix). The sputtering of 65 nm Nb is done in five steps with 10 minutes gap between each step. Doing the sputtering in steps seems to increase the quality of the superconducting contacts. Even though the reason for this is not completely clear, it could be that since Nb is sputtered at high power (400 W), doing the sputtering in steps helps to cool the sample in case it is getting hot while sputtering. The aluminium layer is to separate the Ru layer from Nb since the high spin orbit coupling of Ru can affect the superconducting properties of Nb adversely. Afterwards lift off is done by placing the sample in 50 °C acetone for 30 minutes and by blowing hot acetone on the sample. If the design also includes a normal contact at the end of the device, it is done after placing superconducting contacts. To place the normal contact, the sample is cleaned after the lift off process in hot NEP (80°C) for one hour. Later the sample is taken out by spraying isopropanol and the same resist is spun again with the same parameters. After the e-beam exposure and development, 3 nm Ti and 60 nm Au are evaporated in an e-beam deposition system. Lift of is done in warm acetone similar to other lift off processes. The next step is to fabricate the bonding pads and to connect them with the contacts. For this, after the lift off process of superconducting/normal contacts, the same resist (ARP 672.03, 950k, 3 % anisol) is spun and the substrate is baked with similar parameters but the process is repeated one more time to give thicker resist. This is important since to successfully connect the 90 nm thick superconducting contacts, 120-130 nm thick Ti/Au needs to be deposited so that the Ti/Au layer on top of contact and substrate have an overlapping thickness of 30-40 nm and single layer resist is not thick enough ($<$ 120 nm). The chemical mixture used to develop is the same as before but unlike other fabrication steps, before depositing Ti/Au, the sample is taken to Reactive ion etching (RIE) setup to etch away any undeveloped resist residues on the contact edges where the Ti/Au will be deposited (process details are given in Appendix). This step is necessary because in the case of superconducting contacts, it is found that when

the connection to the contact was made without the RIE step, the interface resistance between the contact and the leads were 2-3 times higher than with RIE process. After RIE, the sample is taken to an e-beam deposition system where 3 nm Ti and 130 nm Au are sequentially deposited. After 30 minutes long lift off process, a different resist (ARP 672.04, 950 K, 4.5 % anisol) is coated at 3000 rpm and the sample is baked at 180 °C for 2 minutes. This last lithography step is to etch away unwanted graphene/graphite layers if there is any, mainly those which are short connecting the contacts or the leads. From the optical microscope images, these graphene layers are identified and their position relative to the coordinate marks are conveyed to the lithography designing software and designs are drown to etch away the unwanted layers. After e-beam exposure and developing, the sample is taken to RIE and using a mixture of Ar/O_2 gas etching is done depending on the thickness of graphene layers which needs to be removed. If it is only single or double layer, 3 seconds etching is enough to remove the layers but if it is thicker layers, up to 12 seconds etching is needed. After etching, the sample is checked under optical microscope to make sure the undesired graphene layers are etched away. If there is still layers left, the RIE process is repeated again. It is important to note that while the graphene layers are etched, part of the resist is also getting etched. So etching unnecessarily for a long time might also etch away all the resist and the graphene between the contacts. After etching, the sample is cleaned in hot (80 $°C$) NEP for 1 hour for the final cleaning before bonding. Afterwards, the substrate is cut in a way that every piece contains only one device and they are glued in to the chip carrier with the short axis of the chip carrier parallel to the length of the contacts. This is important since in most of our cryostats, there is no possibility to rotate the direction of magnetic field. It is also important to mention that all the devices including spin valve devices are kept in vacuum prior to the measurements since it is found that the oxidation of Co increases the interface resistance of the ferromagnetic contacts.

2.4.2 Challenges in fabrication

The fabrication of F/S junctions on graphene has 4 or 5 e-beam lithography steps. In this section, some problems faced during the fabrication process are briefly discussed. One problem faced was the repeated breaks in graphene between the contacts. It is normal to find find breaks in graphene devices which takes 4 or 5 lithography steps to fabricate and in each step, hot acetone is blown on the devices to lift off the unwanted metal layers. But breaks in graphene between the contacts were much more present than usual during the fabrication of F/S devices that at a point in time, it was impossible to make a device where there were no brakes between. One of such device is shown in Figure 2.7. As seen in the figure, graphene is broken between the ferromagnetic contacts which makes it impossible to verify if those ferromagnetic contacts are spin sensitive. What is also visible in the figure is the sidewalls from the superconducting contacts touching the nearest ferromagnetic contact. Even though sidewalls are normal in sputtered contacts,

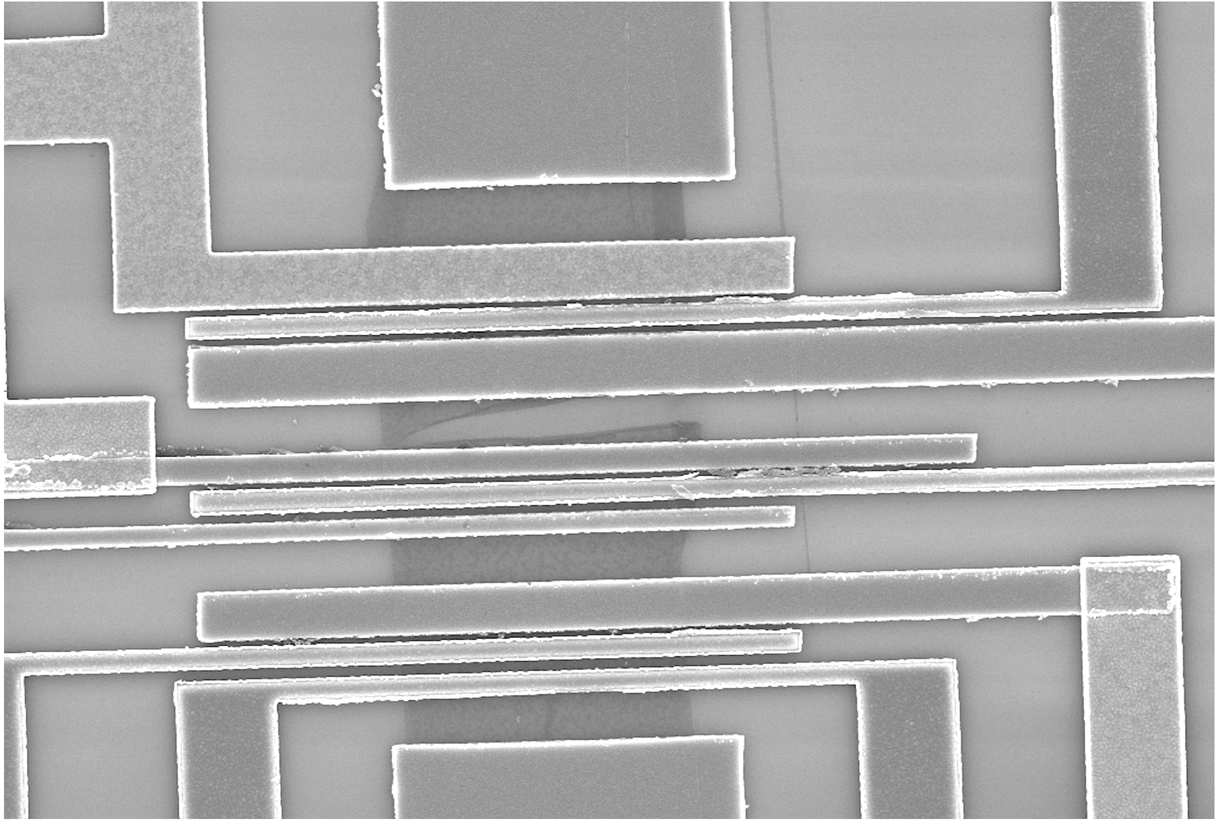

Figure 2.7: SEM image showing ripped graphene between the contacts. The shortening of the contacts by the sidewalls is due to a gentle lift off process.

usually it can be washed away during the lift off process. But in this device the lift off is done very gently to avoid the ripping of graphene but as shown in the figure, it was unsuccessful. So not only that gentle lift off process does not solve the problem, it creates other problems. In the end, even though this problem was not completely solved, but reduced considerably by putting the device in cold acetone and then heating up to 50 $°C$ to perform lift off. Prior to this change, acetone was preheated since it makes the lift off process faster.

The second problem faced was in connecting the superconducting contacts with the bonding pads. Earlier when the superconducting contacts were fabricated, as shown in the Figure 2.8, only the short contacts were superconducting and then they were connected by Ti/Au leads. When these devices were characterised, some of the superconducting contacts had no contact with graphene. Checking the continuity of the superconducting contact through the two leads connecting them showed that there was a break in the path somewhere. Careful inspection of the device under SEM revealed the problem. The superconducting contacts were in total $\sim$ 90 nm thick and the overlapping Ti/Au leads were 130 nm thick which is sufficiently high enough to make proper contact. But what is visible in Figure 2.8 is that, due to the sidewalls arising from the sputtering process, at least in some contacts, there was a break in Ti/Au layer at the edge of the contact. Due

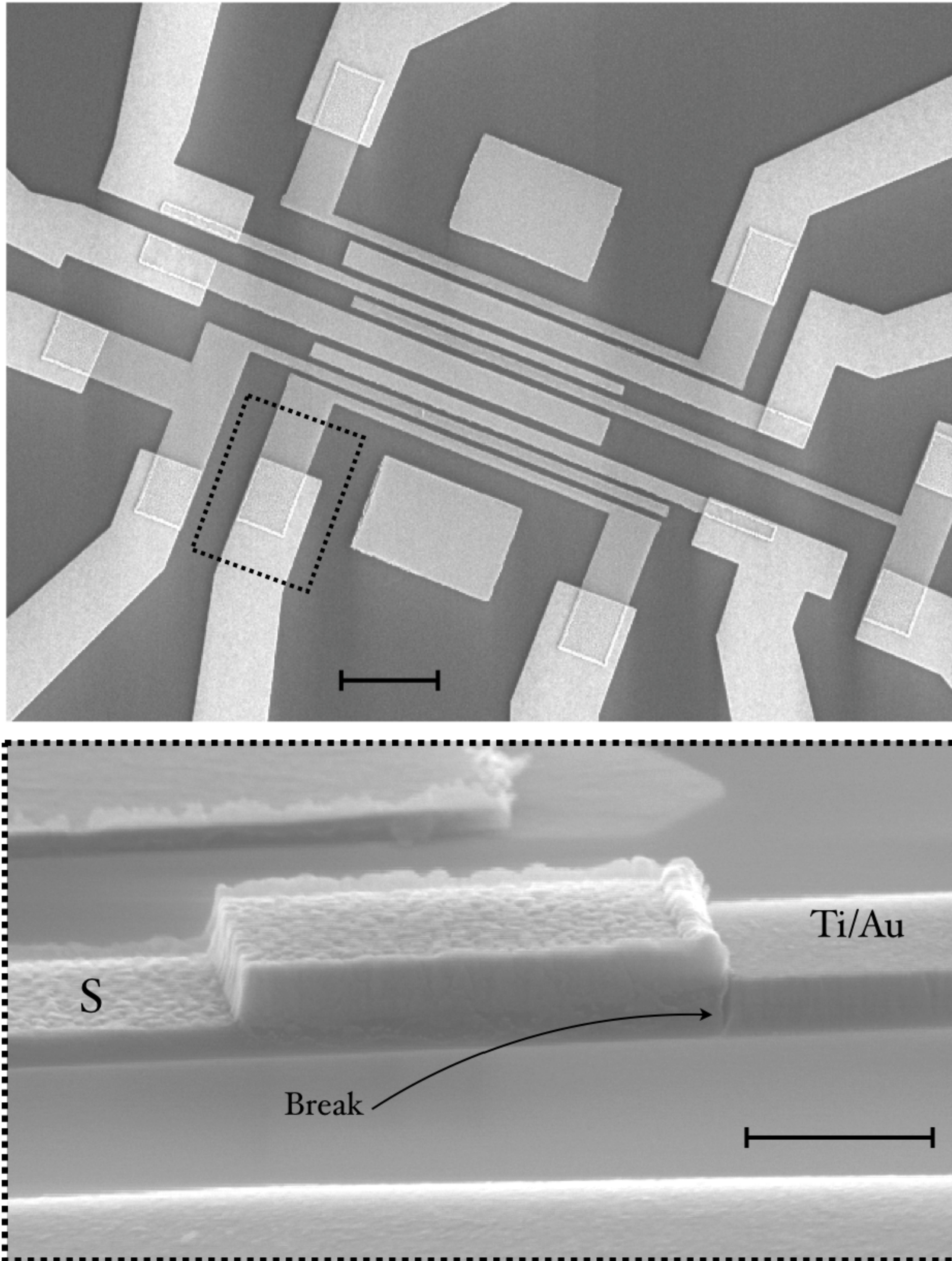

Figure 2.8: SEM images of an F/S device showing the break in Ti/Au leads at the edge of the contact due to the sidewallas. The image in the bottom is a side view of the part shown in the top image in dotted lines. Scale bar for the top and bottom images are 2 μm and 500 nm respectively

to the large number of contacts and leads, it was not possible to increase the overlapping area in this design. Later the problem was solved by fabricating superconducting contacts reaching up to the edge of small writing field (870 μm $\times$ 870 μm) where they can be contacted by Ti/Au with a large overlapping area ($\sim$ 5 μm$\times$ 2 μm).

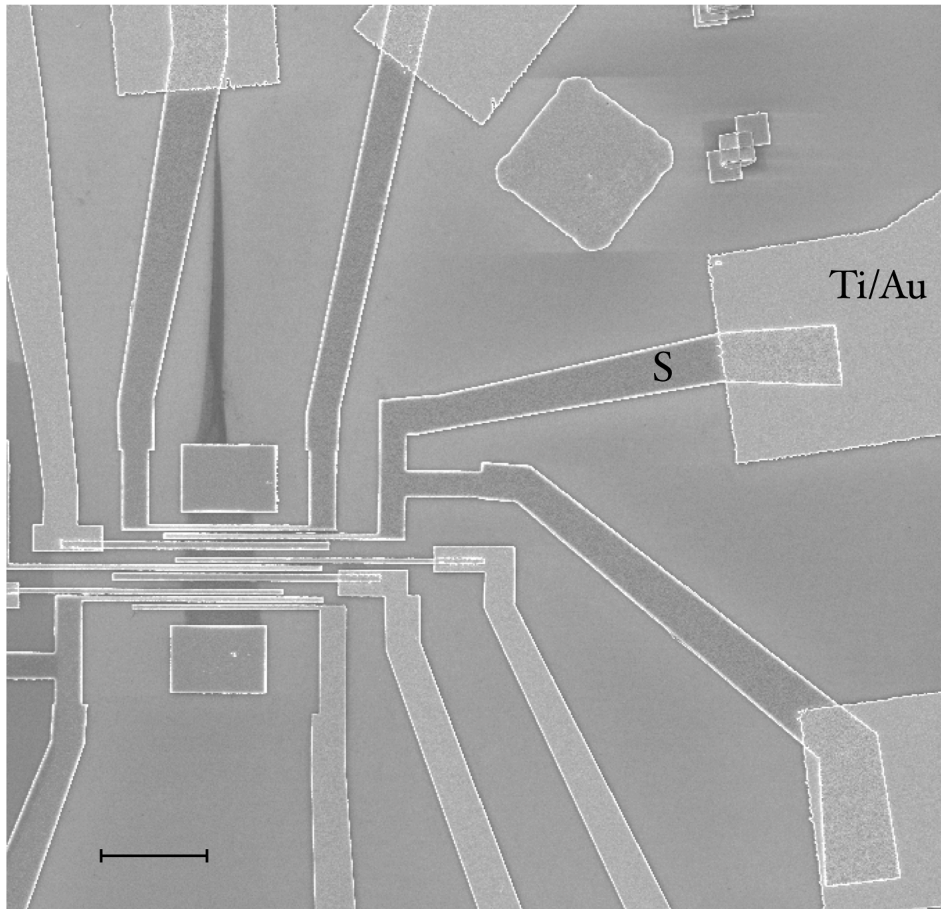

Figure 2.9: SEM image of an F/S device with longer superconducting leads and larger overlapping area with Ti/Au leads. Scale bar is 5 μm.

Chapter 3

Spin transport in graphene

3.1 Introduction

Modern life is inseparably connected to electronic gadgets and the constant drive for faster and smaller devices are propelling the technology to new horizons. All these extremely complicated devices basically do one thing. They manipulates the charge and spin of electron. Prior to the discovery of electron spin [23] and GMR [24, 25] information was based on the charge of the electron which is usually known as electronics. But after the discovery of GMR, it became possible to use the spin state of an electron instead of charge of electron as a basis for a new era of electronics which is now known as "Spintronics". Since the rate of progress in conventional electronics has been getting slower in terms of size reduction and power consumption, Spintronics has became a hot research topic in both in academia and in Industry.

3.2 Spin of electron

The spin of an electron is a quantum mechanical concept which has no classical analogue. The word "spin" can be misleading since it suggests that the spin angular momentum comes from the "spinning" of the electron. So it is important to mention that the spin of electron comes from its "intrinsic" angular momentum of the particle and has nothing to do with the word "spin"!.

It was the Stern-Gerlach experiment which experimentally demonstrated the quantised spin state of an electron for the very first time even though at the time of the experiment the concept of spin didn't exist. The experiment was carried out by sending hot silver atoms through a non uniform magnetic field with a photographic plate at the other end. Since the only outer electron in the silver atom has zero orbital magnetic momentum (l=0) and hence no magnetic moment, one would expect no interaction with external magnetic field. But to their surprise, the inhomogeneous magnetic field split the Ag beam into two distinct parts. If a stream of magnetic dipole is send through a non uniform magnetic field

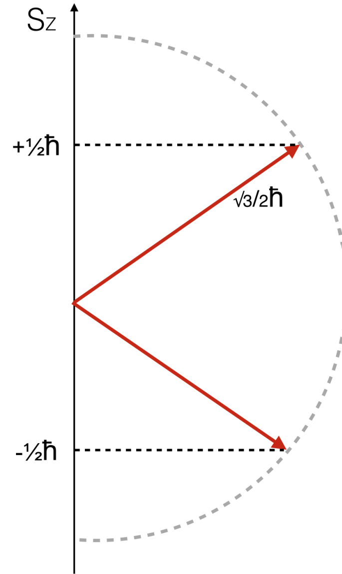

Figure 3.1: A simple diagram showing the spin angular momentum and the quantised z components. Asssigning electron's spin quantum number S=$\frac{1}{2}$ to the equation S=$\hbar\sqrt{(S(S+1))}$ gives S=$\frac{\sqrt{3}}{2}\hbar$ and the z component of angular momentum S$_z = \pm\frac{1}{2}\hbar$

and since classically it can have all possible orientations, one would expect the pattern on the photographic plate to be random and continues. So the two distinct Ag beams in the Stern-Gerlach experiment suggest that the electron has an intrinsic, independent angular momentum which has two possible orientations. This idea of electron having intrinsic angular moment was postulated by A. Goudsmit and George E. Uhlenbeck in 1925.

The spin angular momentum of an electron is given by $S = \hbar\sqrt{(S(S+1))}$. Where S is the spin quantum number and in the case of electron $S = \frac{1}{2}$. The z component of spin angular momentum is given by $S_z = m_z\hbar$ where m_z can have values $\pm\frac{1}{2}$. These two possible values for the m_z are often referred as spin"up" state and spin "down" state. Since electron has intrinsic spin angular momentum, it also displays magnetic moment. The z component of electron's magnetic moment is given by $S_z = gm_s\mu_b$, where g is the electron g factor with the value 2.00232 and μ_b is the Bohr magneton and is given by $\mu_b = \frac{e\hbar}{2m_e}$.

3.3 Magnetic materials

When a magnetic field H is applied to a material, the reaction of the material towards the external field is called magnetic Induction B. The relation between B and H is given

by

$$B = \mu_0(H + M) \tag{3.1}$$

where M is the magnetisation of the material and μ_0 is the permeability of free space. The ratio of M to H is known as susceptibility.

$$\chi = \frac{M}{H} \tag{3.2}$$

Magnetic materials can be mainly divided to three categories as diamagnets, paramagnets and ferromagnets. Atoms in diamagnetic materials have no net magnetic moment and they tend to oppose the applied external field. Diamagnetism is a residual magnetic property of all materials unless paramagnetic or ferromagnetic properties are present. Diamagnetic materials have negative susceptibility and their relation between H and M is shown in Figure 3.3. Paramagnetic materials on the other hand have partially filled electron orbitals and hence their atoms have net magnetic moment. When placed in an external magnetic field they tend to align along the direction of the field as long as the field is present. Paramagnetic materials have positive susceptibility since M increases with H. The third category of materials known as ferromagnets have strong interaction between the individual atomic magnetic moments and they retain most of the magnetisation even in the absence of field.

3.3.1 Ferromagnetic materials and spontaneous magnetisation

The spontaneous magnetisation is a result of a quantum mechanical effect called "exchange interaction". When two electrons with magnetic moment are placed next to each other then there are two types of interactions taking place. First is the relatively short ranged dipole-dipole interaction which tends to align the spins anti-parallelly. The second one is the electrostatic repulsion between electrons which tend to "push" the electron away from one another. Since Pauli's exclusion principle forbids electrons with same spins to be in the same orbital, in materials with stronger electrostatic repulsion, the electrons are aligned parallely so that they can be placed in different shells. This energy difference between parallel and anti parallel configurations is called exchange energy. In ferromagnets the exchange interaction is stronger than the dipole-dipole interaction which enable them to have spontaneous magnetisation. Ferromagnets usually have large susceptibility and their magnetic behaviour is shown in Figure 3.3.

3.4 Magnetoresistance

The name"Magnetoresistance" refers to the change in resistance of a material in the presence of an external magnetic field. The fact that the resistance of a material can be

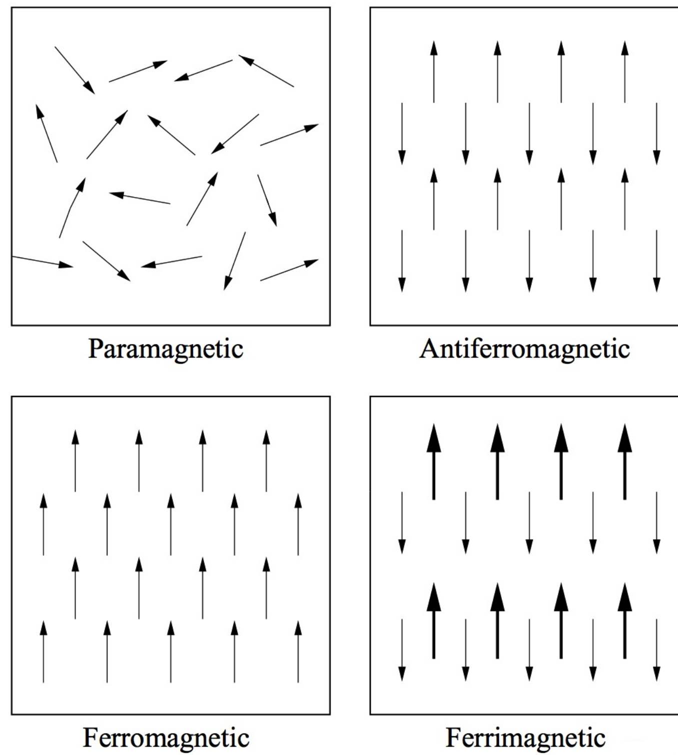

Figure 3.2: A simple schematic picture showing the differnt types of magnetic dipole allignment in differnet magnetic materials. The arrows represent magnetic moments. Taken from [26].

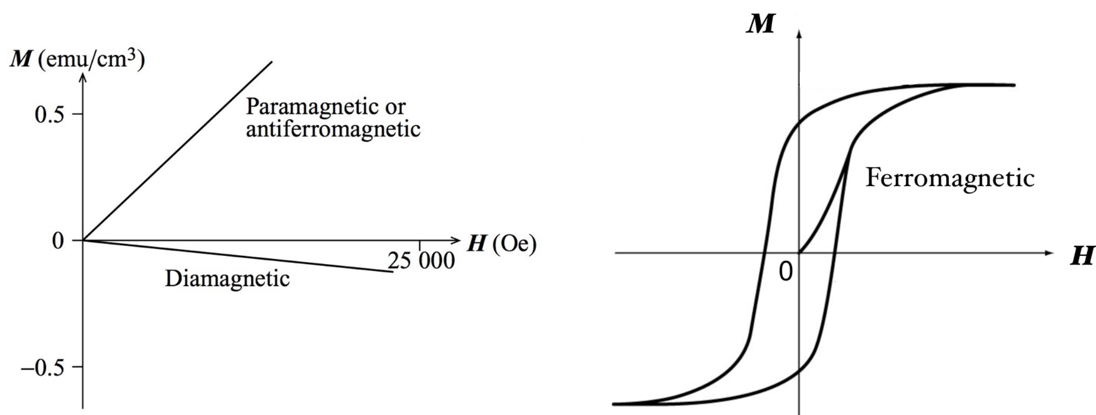

Figure 3.3: (left) Relation between M and H for paramagnetic and diamagnetic materials. Figure taken from [26]. (right) The same for a ferromagnetic material. Note that the ferromagnetic material retains significant amount of magnetisation even when H is zero.

changed simply by applying magnetic field is the working principle of all the hard disk drives and many other electronic devices. The ratio of change in resistance to original resistance is called Magnetoresistance (MR) ratio. MR along with the field required to change the resistance level represent in general the quality of a magnetic device.

$$MR = \frac{\Delta R}{R_0} \tag{3.3}$$

The first observation of Magnetoresistance was in 1850s by Lord Kelvin [27]. which is now known as anisotropic magnetoresistance (AMR). He observed that the resistance of a ferromagnetic wire depends on the direction of external magnetic field with respect to current direction. Even though the the first experiments on AMR produced only a few percent change in resistance, in 1991, IBM introduced read heads based on AMR. The biggest break through in spin electronics came in 1988, with the discovery of giant magnetoresistance (GMR) which was independently reported by A. Fert and P Gruňberg [24, 25] in ferromagnet-normal metal multilayers.

3.4.1 Giant magnetoresistance and Tunneling Mgnetoresistance

In the original experiments Gruňberg and Fert has observed large change in magnetoresistance and thus the term “giant” magnetoresistance. A typical GMR device is composed of two ferromagnetic layers (F1, F2) separated by a thin nonmagnetic layer. When a current is passed through these multilayers, the measured resistance depends on the relative orientation of the layers F1 and F2. The figure below shows the high and low resistance instances. These devices are also called spin valves since it acts like a “valve” where the electron flow through the device is allowed (in parallel configuration) or denied (antiparallel configuration) depending on the magnetisation direction of the ferromagnetic layers.

Whenever a current is injected from a ferromagnet to a normal material there is a redistribution of spins at the interface which give rise to a difference in spin up and spin down electrochemical potentials. This effect is picturised in Figure 3.4. This difference in chemical potential diffuses in material faster or slower depending on the spin relaxation length of the material.

The MR ratio in spin valve devices can be increased by replacing the non magnetic layer by an insulator. In this case electrons from one ferromagnet reaches to the next ferromagnet by quantum mechanical tunnelling and the corresponding magnetoresistance is called tunnelling magnetoresistance (TMR). The probability of tunnelling depends on the available spin up or spin down states in the second ferromagnet and this is illustrated in Figure 1.5.

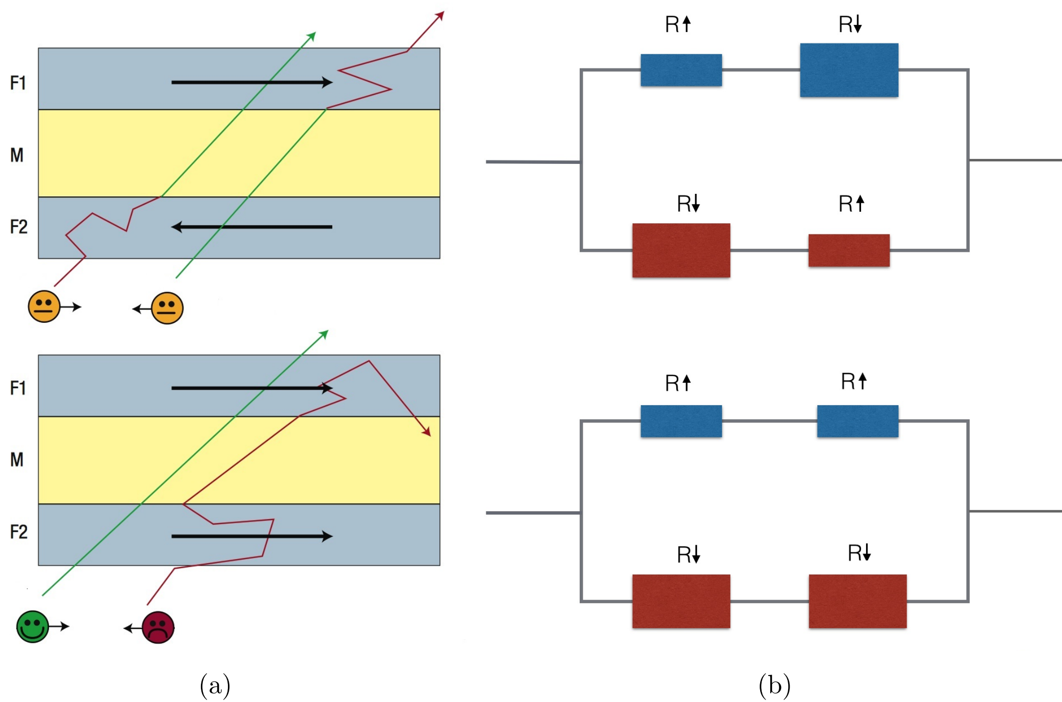

Figure 3.4: (left) A typical GMR device with two ferromagnetic layers (F1,F2) and nonmagnetic middle layer (M). When the ferromagnetic layers are aligned paralell, electrons with spin aligned along magnetsation direction of the F layers "feel" low resistance and electrons with their spin aligned opposite to that of F layers feel high resistance. Figure taken from [28]. (right) Representaion of GMR based on two current model first preposed by Mott [29]. In this model the total current is shown as two independant spin currents. Blue boxes show the resistance experienced by the spin up (down) current and red boxes show the resistance experienced by the spin down (up) current. The size of the boxes represent the magnitude of the resistance.

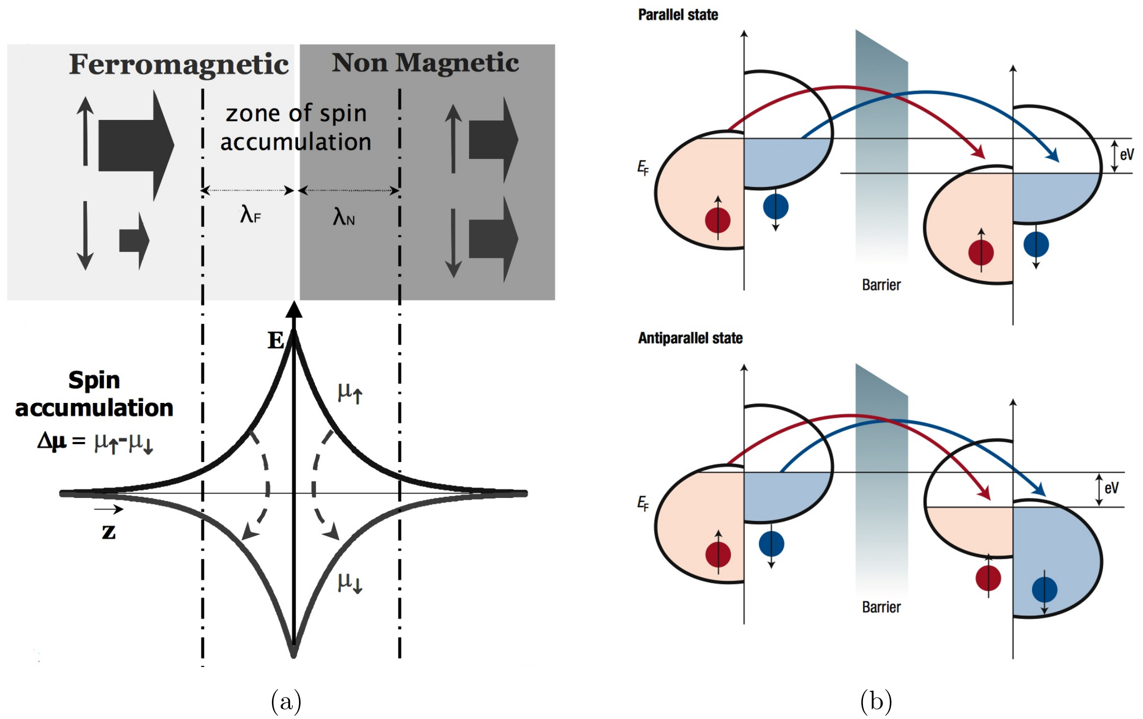

(a) (b)

Figure 3.5: (a) Spin accumulation at the interface of a ferromagnet and a non magnetic material. In the picture the majority carriers are spin up electrons which accumulates at the interface shifting the spin up chemical potential ($\mu_{\uparrow}$) up and spin down chemical potential ($\mu_{\downarrow}$) down. Rate of diffusion of the accumulated spin depends on the spin relaxation length (λ) of the material. The dotted arrows shows the possible spin flip scattering. (b) Tunnelling process between two ferromagnets through an insulating barrier. The probability of tunnelling for a spin up/down electron depnds on the available states for the same in the second ferromagnet. The difference in chemical poterntials between the source and the drain is what drives the tunnelling process.

3.5 Spin injection into semiconductors

Even though all-metallic spin valves mentioned earlier are successfully demonstrated and already found applications in electronics devices, they have one downside which is the short spin relaxation length in metals. So it makes sense to make similar spin valve devices based on semiconductors which have spin relaxation length up to hundreds of micrometers. But after so many attempts injection of spin current into semiconductors found to be extremely difficult. The successful attempts only yielded less than 1% change in magnetoresistance [30, 31] and even then spurious effects and hall effect can be sometimes misinterpreted as GMR [32]. The main reason for such low quality devices found to be the inability to create spin imbalance in semiconductors using transparent magnetic contacts. Later it was found that the problem lies in the difference in conductivities of the magnetic material used for spin injection and the semiconductor which is known as

"conductance mismatch" [4, 33].

3.5.1 Conductance mismatch

The low efficiency in spin injection to semiconductors using magnetic metals is due to the large difference in conductivities between them. To give an example, the number of free electrons in cobalt is in the order of $\sim 10^{28}/m^3$ whereas that of graphene at high gate voltage is $\sim 10^{16} - 10^{17}/m^2$. So when the semiconductor which has a small number of free electron states is contacted by a magnetic metal which has a huge number of free electrons, even the minority carriers in the metal can easily fill up all the minority carrier states in the semiconductor up to the Fermi energy. This makes it impossible to keep a difference in spin chemical potentials between minority and majority spin chemical potentials. The solution to this problem is to place a tunnel barrier between magnetic metal and semiconductor which will reduce the number of electrons injected to the semiconductor. This effect is illustrated in Figure 3.6 as water reservoir-collector system. The triangle-shaped "collector" represents the spin density of states of graphene in contact with the ferromagnet which is depicted as parabolic shaped "reservoir". In the absence of a tunnel barrier, due to the high conductivity of the ferromagnet, spin levels (water levels) in graphene gets saturated and so no difference in spin chemical potentials. On the other hand, If a tunnel barrier is introduced at the interface whose thickness is adjusted in a way that it reduces the conductivity at the interface to match to that of graphene, then as shown in the figure a spin imbalance can be achieved in graphene. This spin imbalance created at the interface then diffuses through graphene at a rate decided by the spin relaxation length (λ).

3.6 Spin injection to graphene

For investigating spin related phenomena in semiconductors, carbon based materials are very suitable because of carbon's low atomic number (Z). One of the main cause for the reduction of spin relaxation length (λ) in materials is the spin orbit coupling which is proportional to the fourth power of atomic number (6). But in addition to low spin orbit and hyperfine coupling, graphene also has other favourable properties like very high mobility at room temperature, low dimensionality, and the possibility of tuning carrier density by tuning the top or bottom gate. So it was not surprising that theoretical prediction of spin relaxation length in graphene reached up to hundreds of nanoseconds [34].

As discussed earlier, the main problem in injecting spins to a semiconductor is the conductance mismatch between the ferromagnet and the semiconductor. The solution to this problem is to deposit a thin insulator layer between the semiconductor and the ferromagnet. But in the case of graphene, growing a thin barrier is not straight forward since low surface energy and high surface diffusion of graphene lead to cluster formation

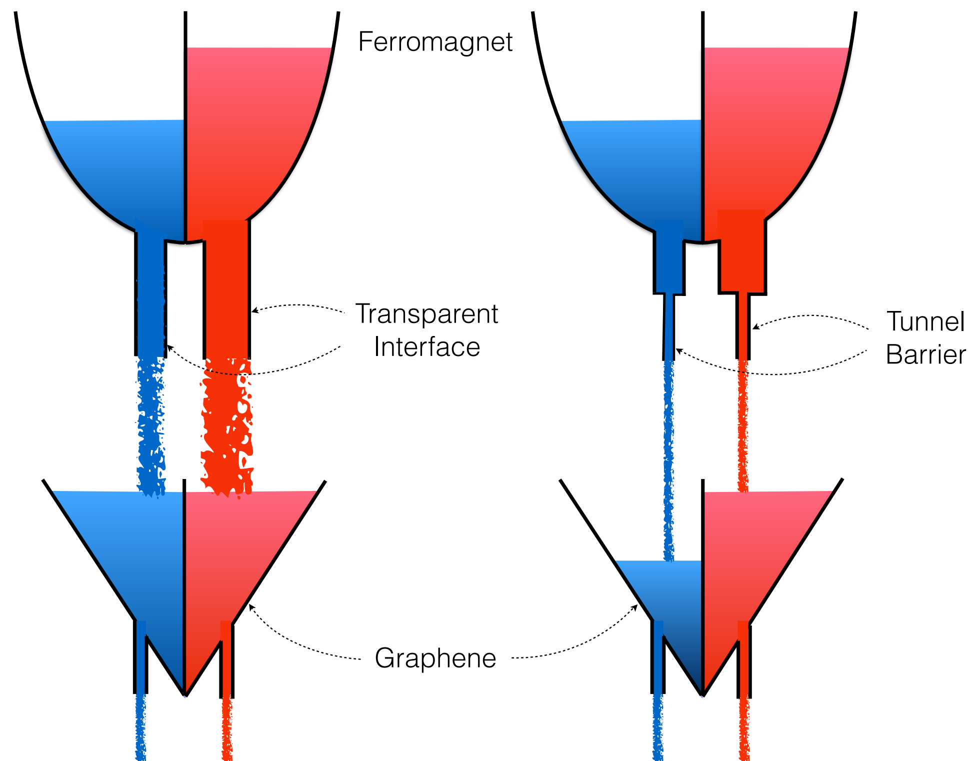

Figure 3.6: Illustration of the conductance mismatch problem as a water circulation system. The setup can be thought of as a reservor-collector system. The reservoir represents the ferromagnet and collector represents the graphene spin density of states. The two colours represents two spins and width of the pipes represents the spin depended conductivities. Figure on the left represents the graphene contacted by a ferromagnet without the tunnel barrier and figure on the right does the same with tunnel barrier.

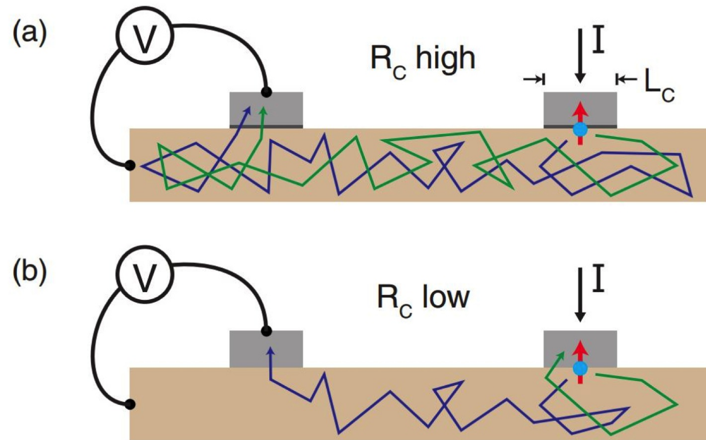

Figure 3.7: Schematic representation of injection and detection of polarised electrons in a diffusive semiconductor using nonlocal geometry. (a) Injection and detection of spin polarised electrons with tunnel contacts. Not only that tunnel barrier increses the spin injection efficiency, but high contact resistance (R_c) caused by the tunnel barrier also stops the injected spins from returning to injector. (b) In the absence of tunnel barriern (low R_c). Some of the spins are reabsorbed by the injector which reduces the injection efficiancy of the ferromagnetic contact. Figure taken from [35].

[35]. The first successful spin transport measurement in graphene was done by Tombros *et al.* [3], where they used thin Al_2O_3 layer as the tunnel barrier. Over the time different groups used variety of tunnel barriers for spin injection like M_gO grown on titanium seed layer [36], ALD (Atomic layer deposition) grown Al_2O_3 [5], T_iO_2 [37], boron nitride flakes [38, 39] and even graphene itself (fluorinated graphene) [40]. These tunnel barriers also solve another problem which is the reabsorption of injected spin polarised electrons by the low resistive ferromagnetic contacts which can heavily reduce the spin injection efficiency. By offering a very high resistive path for the electrons reflecting back to the injector, tunnel barrier contacts reduce the chance of electrons reflecting back to the source contact (Figure 3.7).

In the first successful demonstration of the spin transport in graphene, the deduced spin life times were between 100-200 ps [3], which is orders of magnitude less than the theoretically expected values. Out of the possible reasons for this suppressed spin life times, the obvious one is the pin holes in the tunnel barriers which the authors acknowledge in the same paper. T. Massen *et al.* [35] have done a detailed study of contact induced spin relaxation in graphene where they show that the magnitude of the contact resistance play very important role in spin transport. So the obvious thing to do to increase the spin life time is to grow a pin-hole free tunnel barrier which is exactly what W. Han *et al.* [36] have done. They have developed a method for fabricating pin-hole free Magnesium oxide (MgO) tunnel barriers with Titanium seed layer [41]. These contacts with low tunnel barrier surface roughness yield a spin relaxation length of 2.5-3 μm and spin life times of

400-500 ps which are higher than reported values for pin-hole contacts (λ =1.2-1.4 μm, τ =100-200 ps). Although these values are promising, it is still far away from the expected theoretical values. The reason for this discrepancy can be the S_iO_2 substrate which is known to mask the inherent electrical properties of graphene [42]. The roughness, trapped charges and surface phonons in the S_iO_2 substrate reduce the mobility of graphene. The same reasons can be said for the reduced spin relaxation length and time. So the study of spin transport in graphene without the S_iO_2 substrate might give a better understanding of the inherent spin transport properties of graphene. There are two established ways to produce high mobility graphene devices. One is by placing graphene on top of hexagonal boron nitride (h-BN) flake and the other is by suspending graphene. h-BN is atomically flat and free of trapped charges and hence the mobility of graphene on h-BN is shown to be two orders of magnitude higher than that on S_iO_2 [43]. P.J Zomer *et al.* [37] reported the first successful spin transport measurement on graphene placed on h-BN. With their fabrication process, they were able to achieve mobilities up to 40,000 $cm^2V^-1s^-1$ (at room temperature) and spin relaxation length up to 4.5 μm [37]. They were also able to measure spin signal over a distance of 20 μm. This increase in spin relaxation length comes from the increased spin diffusion constant $D_s = 0.052$ m^2/s which is much higher than that of the regular S_iO_2 devices ($D_s = 0.02 - 0.03$m^2/s). But the measured spin life times are still in the order of 200 ps which roughly the same as that of the S_iO_2 devices. Suspended graphene also shows similar spin transport characteristics [44]. As reported by Marcos H.D. *et al.*, [44] suspended graphene has mobilities up to 10^5 cm^2/Vs and spin life time and relaxation up to 150 ps and 4.74 μm respectively. This means that even though substrate plays an important role in defining the spin transport characteristics of graphene, it is not the only factor. The other reasons which might be reducing the spin life time can include adsorbates, charged impurities on the surface and inhomogeneity in the mobility between the suspended and supported parts of graphene. A more sophisticated way of fabricating spin sensitive devices based on graphene has been reported recently [45]. In this method the contacts for injection which is 40 nm Co/1 nm MgO (bottom to top) prepared separately on a S_iO_2 substrate upon which graphene previously prepared on h-BN is pressed with graphene side contacting MgO. This method has mainly two advantages. One is that the tunnel barrier MgO can be deposited much more uniformly on Co compared to graphene. Secondly, the graphene is never in contact with chemicals normally used for fabrication like PMMA, acetone, developer etc, which yields clean graphene with less contaminants. Because of these advantages they were able to achieve spin relaxation lengths and spin life times up to 10 μm and 3.7 ns respectively which are some of the highest values achieved on graphene.

3.7 Simple theory of spin transport in graphene

Consider a graphene device where the graphene is contacted by four tunnel contacts of different widths as shown in Figure 3.8. For simplicity, assume the contacts F2 and F3 as ferromagnetic and F1 and F4 as normal. A spin polarised current is injected from F2 and F1 is grounded so that the charge transport is only between F2 and F1. The injected spins from the ferromagnet split the spin chemical potentials ($\mu_\uparrow,\ \mu_\downarrow$) and create a spin accumulation ($\mu_\downarrow$) in graphene under the injecting contact ($\mu_s = \mu_\uparrow - \mu_\downarrow$). These spins diffuses exponentially in both directions over a length scale which is determined by the characteristic length scale λ (spin diffusion length). If the distance between F2 and F3 which is represented as L in the figure is comparable to λ ($L \leq \lambda$), then the elevated spin chemical potentials can be detected by F3. The diffusion of the spin accumulation can be represented by one dimensional Bloch equation as shown below.

$$D\nabla^2 - \frac{\mu_s}{\tau} + \omega \times \mu_s = 0 \tag{3.4}$$

Where D is the spin diffusion constant and τ the spin lifetime. ω represents the Larmer precession frequency which is given by $\omega = g\mu_B B$ where g is the gyromagnetic ratio (2), μ_B the Bohr magneton and B is the perpendicular external magnetic field.

If one were to consider a practical lateral spin valve device with all four contacts being magnetic, the change in spin chemical potentials over distance is relatively more complicated than shown in Figure 3.8. Variation of spin chemical potentials with respect to magnetisation direction of the contacts and lateral distance of such a system is shown in Figure 3.9. As mentioned earlier, all the four tunnel contacts have different widths which make it possible to control the magnetisation direction of the contacts separately since the coercive field of the contact is directly proportional to 1/width, provided the length of the contact is much larger than the width. As shown in the Figure 3.8, the widths of the contacts are in the order $W4 > W3 > W2 > W1$ which in an increasing in-plane external magnetic field will produce a contact switching order F4, F3, F2 and lastly F1. This gives rise to five possible magnetic configurations for the system starting from $\uparrow\uparrow\uparrow\uparrow$, $\uparrow\uparrow\uparrow\downarrow$, $\uparrow\uparrow\downarrow\downarrow$, $\uparrow\downarrow\downarrow\downarrow$ and lastly $\downarrow\downarrow\downarrow\downarrow$. The figure also shows an expected practical measurement data where the change in spin chemical potential in graphene due to the switching of the contacts can be clearly seen.

In practice the measurement is done as follows, at first, the magnetic contacts are magnetised by applying an in-plane magnetic field (B). An ac or dc current (I_{INJ}) is then injected from F2 to F1. At this point a positive non-local voltage can be measured between F3 and F4 since chemical potential diffuses exponentially over distance and F3 is closer to the injecting contacts than F4. Since non-local voltage is proportional to the amplitude of injected current, a non-local resistance (R_{NL}) can be defined as $R_{NL} = V_{NL}/I_{INJ}$ which makes it much more easier to compare multiple data sets. Upon increasing in-plane magnetic field in the opposite direction, the contacts start to switch and this exhibits as

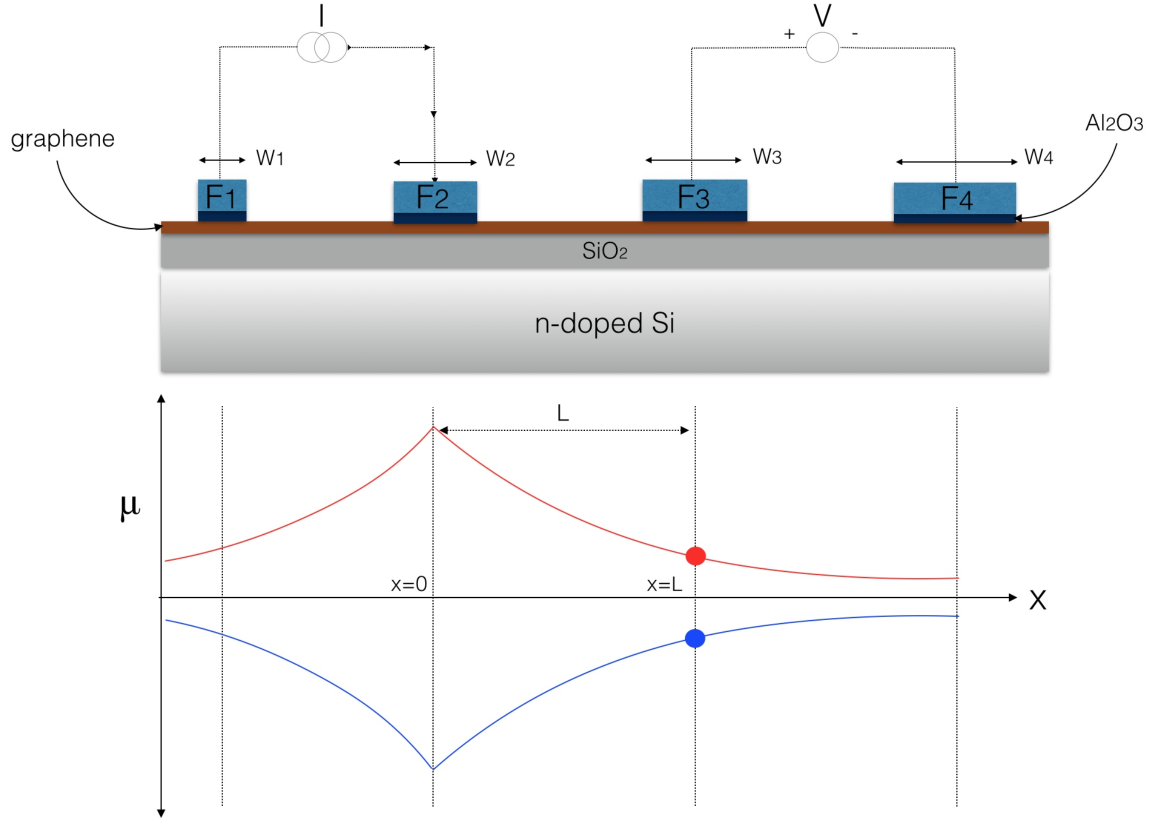

Figure 3.8: (top) Cross sectional view of a typical spin injection/detection setup. Graphene is placed on a SiO_2/Si substrate which can also act as bottom gate. Four tunnel contacts of different widths (W1, W2, W3 and W4) are placed on top of graphene out of which at least two have to be magnetic to perform spin injection and detection measurements. (bottom) Spin chemical potentials $\mu_\uparrow$ (red), $\mu_\downarrow$ (blue) in graphene as a function of distance assuming F2 and F3 are the only magnetic contacts. Under the contact F2, due to the injection of polarised elctrons the spin chemical potential splits and creates a spin accumulation $\mu_s = \mu_\uparrow - \mu_\downarrow$ which diffuses exponentialy to the left and right. Depending on the magnetization direction of the contact F3, it can measure $\mu_\uparrow$ (red dot) or $\mu_\downarrow$ (blue dot) at x=L.

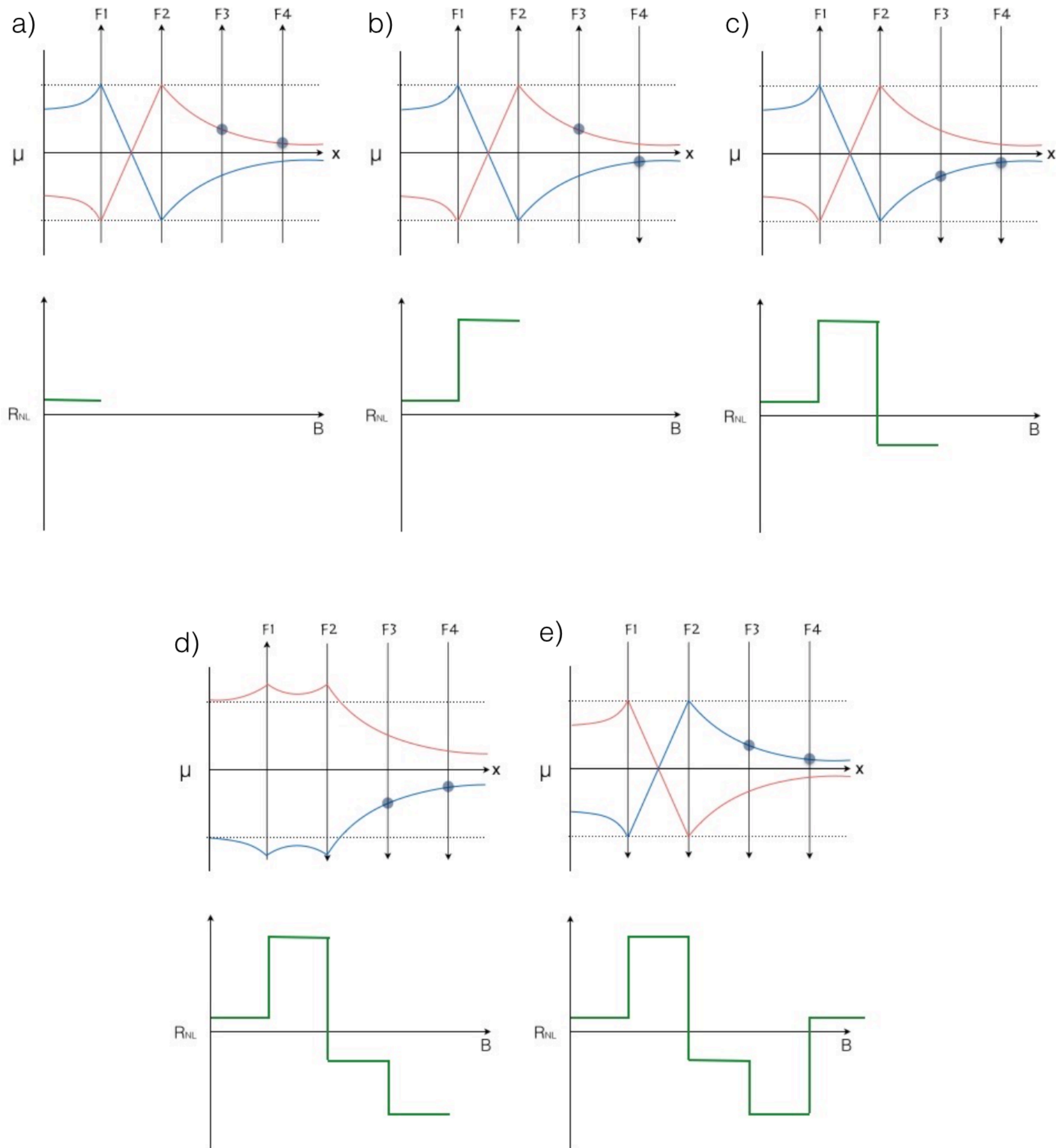

Figure 3.9: Possible chemical potential variations and carresponding experimental data arising from a four terminal nonlocal spin valve measurement with all contact being magnetic. The figure can be thought of as five sets with each set showing the change in chemical potential and expected measurement data (green curve) shown as R_{NL} vs B curves. The black dots shown

Figure 3.9: in the figure represent what the detecting contacts F3 and F4 measures. (a) All contacts are magnetised in the"up" direction. The red and blue line represent $\mu_\uparrow$ and $\mu_\downarrow$ in the graphene channel respectively. Under the contact F2 $\mu_\uparrow$ has a maxima since F2 is injecting spin up electrons to the channel. Under the contact F1 situation is different since F1 acts as drain and it accepts all the spin up electrons which explains the minima in $\mu_\downarrow$. The spin imbalance created diffuses and is detected as positive R_{NL} (V_{NL}/I_{INJ}) since both F3 and F4 are probing $\mu_\uparrow$. (b) The external magnetic field is increased further and causes F4 to "switch" and it is now probing $\mu_\downarrow$. The nonlocal voltage measured between F3 and F4 is higher than before and can be seen as a "step-like" feature in R_{NL} Vs B curve. After the switching, the curve stays flat until the next contact switches. (c) F2 switches after increasing the magnetic field further. Now both F3 and F4 are probing $\mu_\downarrow$ and R_{NL} switches to negative value. (d) F3 also switches and its now injecting spin down electrons to the graphene channel. Note that magnitude of the maxima and minima in $\mu_\uparrow$ and $\mu_\downarrow$ are higher than previous instances. F3 and F4 are still measuring $\mu_\downarrow$ but since a higher spin imbalance is created under F2 it measures a higher negative R_{NL}. The last contact also switches and system looks similar to that of (a) with $\mu_\uparrow$ and $\mu_\downarrow$ interchanged. R_{NL} is positive again even though both F3 and F4 are probing $\mu_\downarrow$.

step like features in the R_{NL} versus B graph which is also shown in the Figure 3.9. The magnitude of the change in R_{NL} (ΔR_{NL}) associated with the switching of the contact depends on many factors. Assuming the contacts are high resistive ideal tunnel contacts, $\Delta R_{NL}(R_{NL}\uparrow\uparrow - R_{NL}\uparrow\downarrow)$ can be expressed as follows

$$\Delta R_{NL} = \frac{1}{\sigma_G}\frac{P^2\lambda_G}{W}\ e^{(-L/\lambda_G)} \tag{3.5}$$

where P is the polarisation of the contact (injection-detection efficiency) and λ_G, W, σ_G are the spin diffusion length, width and conductivity of graphene respectively. In order to find the polarisation of the contact, one has to know the spin diffusion length and the spin life time before hand. In diffusive transport, λ_G is given by

$$\lambda_G = \sqrt{D\tau_s} \tag{3.6}$$

where D is the spin diffusion constant and τ_s is the spin lifetime. Both these quantities can be deduced from Hanle spin precession measurements.

3.7.1 Gate tunable spin transport

This section discusses the effect of change in carrier density on spin transport properties of graphene. As mentioned before, one of the major advantage of graphene is the ability to control carrier density by applying a gate voltage. This is usually done by applying a dc voltage to the highly doped Si substrate which is separated from graphene by in most

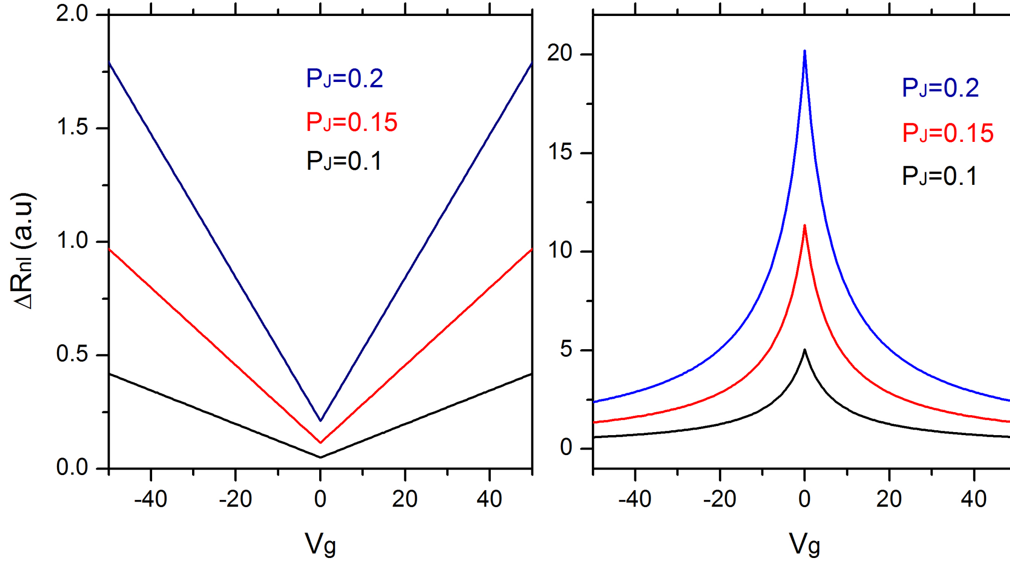

Figure 3.10: (left) Numerical plot based on equation 2.8 showing the change in ΔR_{NL} with respect to gate voltage (V_G) of a graphene nonlocal spin valve with transparent contacts for three different values of P_J. (right) Same plot for spin valve with tunnel contacts.

cases by a 300 nm S_iO_2 layer, which acts as dielectric. The following discussion on the effect of conductivity (σ_G) on R_{NL} is based on references [6] and [46].

Quantitatively, ΔR_{NL} can written in a general form as $\Delta R_{NL} =$

$$4R_G e^{(-L/\lambda_G)}\left(\frac{P_J\frac{R_J}{R_G}}{1-P_J{}^2}+\frac{P_F\frac{R_F}{R_G}}{1-P_F{}^2}\right)^2 \times \left(\left(1+\frac{2\frac{R_J}{R_G}}{1-P_J{}^2}+\frac{2\frac{R_F}{R_G}}{1-P_F{}^2}\right)^2 - e^{(-2L/\lambda_G)}\right)^{-1} \tag{3.7}$$

Where R_G and R_F are the spin resistances of graphene and ferromagnet respectively and are given by $R_G = \dfrac{\lambda_G}{\sigma_G W}$ and $R_F = \dfrac{\rho_F \lambda_F}{A_J}$. Here ρ_F, λ_F, A_J and W are resistivity of the ferromagnet, spin diffusion length of the ferromagnet, junction area and width of graphene flake respectively. The junction area (A_J) is given by the product of graphene width and the width of ferromagnetic contact. P_F is the polarisation of the ferromagnet, P_J is the polarisation of the interfacial current, R_J is the contact resistance between ferromagnet and graphene and L is the distance between the magnetic contacts. In order to understand the effect of σ_G on ΔR_{NL} we can define two regimes depending the ratio R_J/R_G. For transparent contacts, $R_J << R_G$ and the earlier general equation reduces to

$$\Delta R_{NL} = \frac{4}{R_G}\left(\frac{P_J R_J}{1-{P_J}^2} + \frac{P_F R_F}{1-{P_F}^2}\right)^2 \frac{e^{(-L/\lambda_G)}}{1-e^{(-2L/\lambda_G)}} \tag{3.8}$$

Assuming fixed values for parameters P_J, P_F, R_F and L one can see that $R_{NL} \propto \sigma_G$. For the tunnel contacts, $R_J >> R_G$ and the general equation reduces to

$$\Delta R_{NL} = \frac{1}{\sigma_G}\frac{{P_J}^2\lambda_G}{W}e^{(-L/\lambda_G)} \tag{3.9}$$

By fixing P_J, W, L, and λ_G, it can be seen that $\Delta R_{NL} \propto \dfrac{1}{\sigma_G}$ for tunnel contacts. Other than this main two regimes one can also define a third regime called the intermediate regime where $R_J \sim R_G$. Practically this represents tunnel contact with inhomogeneous insulating layer having pin-holes. For this regime equation reduces to

$$\Delta R_{NL} = R_G\left(\frac{\frac{P_J R_J}{R_G}}{1-{P_J}^2}\right) \times \left(\left(1+\frac{\frac{2R_J}{R_G}}{1-{P_J}^2}\right) - e^{(-2L/\lambda_G)}\right)^{-1} e^{(-L/\lambda_G)} \tag{3.10}$$

Figure 3.10 shows the variation of ΔR_{NL} with respect to applied gate voltage V_G based on the equations 3.8 and 3.9. For the numerical model, the values assumed for the parameters λ, μ and W are 2 μm, 2000 cm^2/Vs and 2 μm respectively. Conductivity of graphene depends on the gate voltage as $\sigma_G = \sigma_0 + \mu e\alpha|V_G|$ where σ_0 is the minimum conductivity (or conductivity at Dirac point. Assumed to be $4e^2/h$), μ the mobility and $\alpha = 7.8 \times 10^{14}$/Vm^2.

3.8 Experimental results

The results presented in this chapter are from single layer graphene spin valve devices. To fabricate the spin valve devices, first, graphene flakes are transferred from an HOPG graphite block to an S_iO_2/Si^{++} substrate by means of scotch-tape method and single graphene layers are identified and located using an optical microscope. Following the e-beam lithography, contacts of varying widths (200 nm-600 nm) and lengths (10 μm-12 μm) are defined on PMMA and later developed using isopropanol/water mixture. Over the time we have developed two slightly different methods for producing the thin insulator layer needed for spin injection. One is the ALD (Atomic layer deposition) grown Al_2O_3 without any seed layer and the other is with Ti seed layer. Al_2O_3 with Ti seed layer gives a more homogeneous tunnel barrier and a much better yield for successful spin

injection/detection contacts. After the growth of Al_2O_3 in the ALD machine, the sample is taken out to a metal deposition system where 50 nm Cobalt and 10 nm Gold are subsequently deposited. The thin gold layer is to help protect the Co layer from oxidising but the sides of the contacts are still exposed to the surroundings. Afterwards a second e-beam step is done to connect the contacts to big bonding pads and a third e-beam step is also done to etch away any unwanted graphene flakes if necessary (Details of the fabrication process are given in chapter 2). Later, the devices are bonded and are ready for the measurement. All devices are characterised using standard lock-in techniques with an ac current of amplitude 1-10 μA and of frequency 17 Hz. In the following pages measurement data from several devices are presented and each one is chosen to a show a certain characteristic behaviour.

As explained earlier, the biggest challenge in producing spin valve devices based on graphene is in fabricating thin, homogeneous tunnel barriers. One of the best way to produce ultra thin tunnel barrier is to grow oxide-based insulators using atomic layer deposition (ALD). Due to the self limiting manner in which oxides are grown using ALD, sub-nanometer thick homogeneous, pinhole free tunnel barriers can be grown with out difficulty. But in the case of graphene, due to it's chemically inert nature and because of the absence of dangling bonds, the growth of ALD based insulator directly on pristine graphene is non trivial [21]. The solution to this problem is straight forward which is functionalising graphene surface with chemicals or depositing seed layers upon which ALD based insulator can be grown. But surprisingly in our experiments, we found that even without any prior treatment Al_2O_3 can be grown using ALD with a reduced tunnel barrier quality. The grown layers always contain pin holes and the growth rates are inconsistent from sample to sample. Since in our fabrication recipe the growth of Al_2O_3 is done after defining the contacts using e-beam lithography, it is possible that we are accidentally functionalising the graphene surface during e-beam exposure or developing. This preposition is consistent with the fact that we do not see any growth on freshly prepared graphene flakes. Even though we have a decent yield of working devices ($\sim$20%), the inconsistencies in contact resistance from device to device forced us to make the functionalisation deliberate and controllable by adding a seed layer prior to the ALD growth.

3.8.1 Spin injection using ALD grown Al_2O_3 tunnel barrier

The thickness of the tunnel barrier grown by ALD is determined by the number of times the precursors react to the material surface in question. When both precursors complete the reaction, it is called one complete cycle. For our devices, we use trimethylaluminum (TMA) and water vapours as precursors. In order to improve the yield of working devices, many devices were made with varying cycles of ALD process ranging from 3 cycles up to 20 cycles. The best yield was found for devices with 10-12 cycles of ALD growth. But there were devices which showed measurable spin signals with just 3 cycles of tunnel

growth. Results of the measurement performed on such a low resistive device are shown in Figure 3.11. The figure also shows the scanning electron microscope (SEM) image of one our device. The contacts are made of ∼1 nm AL_2O_3/50 nm Co/10 nm Au from bottom to top. The Au layer serves as a protection layer for Co since it oxidises upon coming in contact with air. The width of the contacts range from 200 nm-600 nm. As seen from the picture, the contacts are connected by non magnetic leads (Ti/Au). This is very important since in the earlier devices, where the leads were also magnetic, (meaning contacts, leads and bonding pads are fabricated in one lithography step), it was possible to detect spin signal even when the in-plane external magnetic field was perpendicular to the length of the contacts (soft axis). This "not so rare" observations opened up the possibility that at least in some earlier devices, the magnetic leads which connect the contacts to the bonding pads might have contributed to the spin signal. In that case making the leads non-magnetic should solve the problem.

After the fabrication and successive bonding, the devices are taken to a room temperature measurement setup with the possibility of applying an in-plane magnetic field. The typical measurement done to prove spin injection and detection in our devices is the non-local four terminal spin valve measurement which is discussed in detail earlier. In practice, the measurement is done as follows. First an in-plane magnetic field is applied along the ferromagnetic contacts which is many times stronger than the coercive field of the contacts in order to make sure that the contacts are completely magnetised before the measurement. Later, an ac current of magnitude 1-10 μA is applied between two contacts and the resulting non local voltage is picked up by a lock-in amplifier. Then the in-plane magnetic field is slowly swept over a range which covers all the expected switching fields of the contacts. If all the contacts are spin sensitive, three step-like features and three horizontal resistance levels are observed in the non-local voltage. To observe any spin signal, at least one contact each in injecting pair and detecting pair has to be spin sensitive. Since in all devices there are at least 6 contacts, different configurations for spin valve measurement are possible. In this thesis injecting and detecting contacts are represented as "$I_{n,n}; V_{n,n}$" where "$I_{n,n}$" represent the injecting contact with source represented by the letter 'n' close to I and drain represented by the second 'n'. The non-local voltage contacts are represented as "$V_{n,n}$" with first 'n' representing the contact close to the injecting contact. For example, $I_{2,1}; V_{3,4}$ means current is injected from contact 2 to 1 and voltage is measured between contact 3 and 4 with contact 3 being next to contact 2.

3.8.2 Spin valve device 03.26_S

Device 03.26_S consists of 6 ferromagnetic contacts placed on top of a graphene flake of width 1.2 μm. This device was one of the earliest one and had only 3 cycles of ALD grown Al_2O_3 tunnel barrier. As expected the two contact resistances are very low (∼$1k\Omega$). Contact resistance is estimated by using the fact that at high gate voltages, graphene with unit length and width has a sheet resistance of ∼1k Ω. Figure 3.11 shows the SEM image

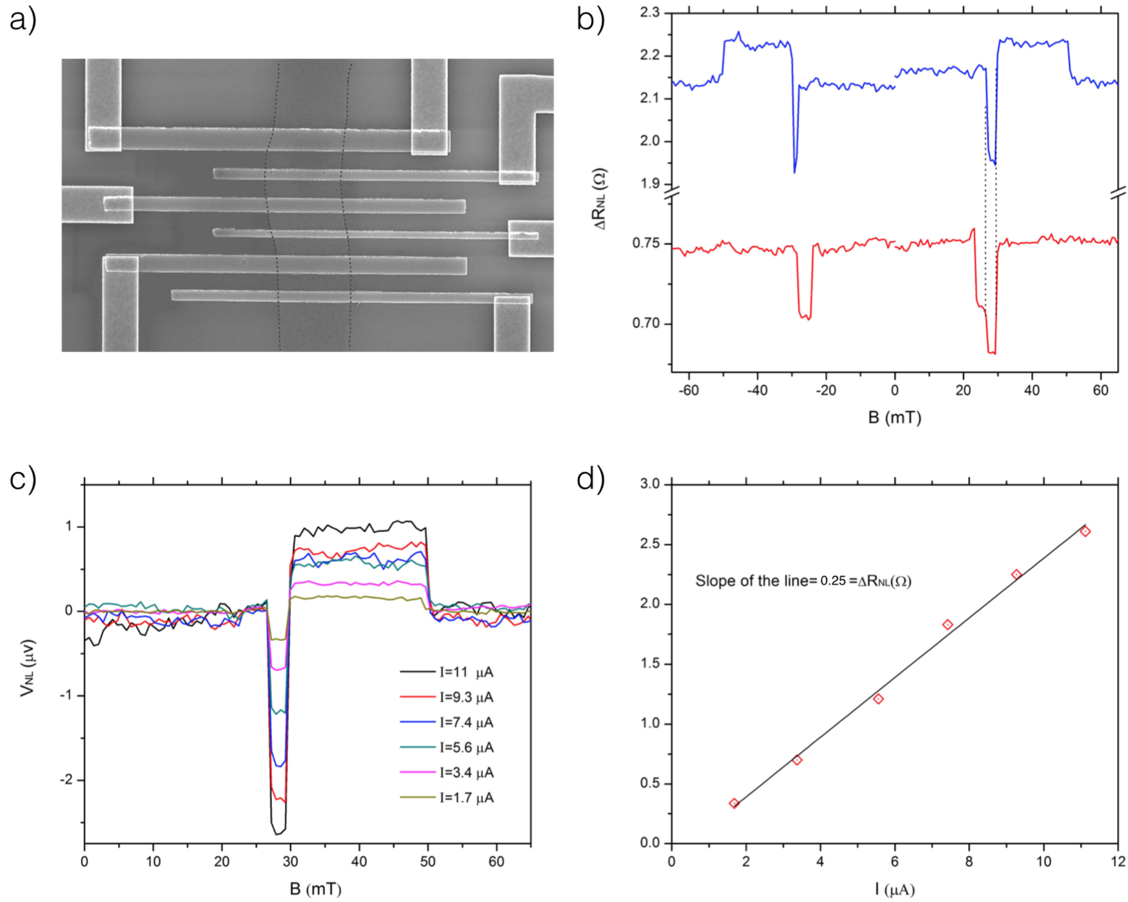

Figure 3.11: (a) SEM image of a typical spin transport device. The wdith of the contacts range from 200 nm-600 nm and the speration is 500 nm. Scale bar is 1 μm. (b) Non-local spin signal shown as R_{NL} Vs B graph at $V_G = 50$ V for two different configurations $\mathrm{I}_{3,4}; \mathrm{V}_{2,1}$ (red curve) and $\mathrm{I}_{5,6}; \mathrm{V}_{4,3}$ (blue curve). Both blue and red curves show two sets of data, one for the forward direction (from 0 to +65 mT) and the other for reverse direction (from 0 to -65mT). (c) Nonlocal voltage V_{NL} for different values of injected current. (d) Graph showing the calculated R_{NL} corresponding to injected current strength and the linear fit.

of a typical spin valve device. As seen in the image, one of the contact is connected by two leads in order to make sure that the leads are in good contact with the ferromagnetic contacts and their contribution to the actual contact resistance is negligible (only $\sim$100 Ω). The device has 6 contacts (F1, F2...F6) and widths of the contacts are as follows F1 (300 nm), F2 (600 nm), F3 (500 nm), F4 (400 nm), F5 (300 nm), and F6 (200 nm). Figure 3.11(b) shows the results of non-local spin valve measurements using with the contact configurations $\mathrm{I}_{5,6}; \mathrm{V}_{4,3}$ (blue curve) and $\mathrm{I}_{3,4}; \mathrm{V}_{2,1}$ (red curve). For the configuration $\mathrm{I}_{5,6}; \mathrm{V}_{4,3}$ two resistance levels are visible in both forward and backward sweeping directions

and a possible third resistance level in the negative field starting around 43mT. For the configuration $I_{3,4}; V_{2,1}$, two resistance levels are visible in the forward sweeping direction and only one resistance is visible in the reverse direction meaning one contact involved in the measurement is not spin sensitive at all. Comparing the red curve with the blue one, there are two abrupt "jumps" at 26 mT and 30 mT which are common to both and hence is caused by the switching of contacts F3 and F4 since they are common in both configurations. The first jump in the red curve around at $\sim$ 23 mT is from the contact F2 since it is wider than both F3 and F4 (switching field $\sim 1/W$). By the same logic, the last jump in the blue curve is due to the switching of the contact F6 and the possible switching at 43 mT is from F2. So the switching fields of the contacts with widths 200 nm (F6), 300 nm (F1), 400 nm (F4), 500 nm (F3), 600 nm (F2) are 50 mT, 43 mT, 30 mT, 26 mT and 23 mT respectively. Figure 3.11(c) shows the results of the measurement performed using the configuration $I_{5,6}; V_{4,3}$ for different values of injecting currents. A constant background voltage is subtracted from all the curves in this graph to make the comparison easy. Change in non-local voltage ΔV_{NL} for the first switching event is calculated for each current value and is shown in part (d) of the figure. The data points can be fitted with a straight line proving the fact that the parameter ΔR_{NL} is independent of Injected current and can be used to qualitatively compare the efficiency of the devices.

ΔR_{NL} measured in this devices is only 0.25 Ω and is similar to ΔR_{NL} reported in devices with transparent contacts [47]. This is not surprising since 3 cycles of ALD even on a best suited surface gives only $\sim$0.3 nm thick Al_2O_3 and on a graphene surface, it is expected to be even less. This thin tunnel barrier character is also visible in the contact resistances which is similar or slightly higher than what is expected from a device with transparent contacts and so it is not surprising that some contacts were not spin sensitive at all. The asymmetry between the forward and reverse sweep in the red curve from Figure 3.11 is not uncommon and can also be seen in major published articles [36], [44]. Even though its not possible to pinpoint the exact reason in our case, the possible causes can be the impurities in the ferromagnet, imperfect contact shape, oxidation of the contact from the sides etc.

3.8.3 Spin valve device 07.30_S2

Spin valve 07.30_S2 has 12 cycles of ALD grown Al_2O_3 tunnel barrier and as one would expect has a higher contact resistance compared to the previous device discussed. Similar to device 03.26_S, the device has 6 contacts namely from F1 to F6 with widths 200 nm, 500 nm, 600 nm, 400 nm, and 200 nm respectively. The two contact resistances are $R_{1-2} = 8$ kΩ, $R_{2-3} = 12$ kΩ, $R_{3-4} = 1$ kΩ, $R_{4-5} =$ "open", $R_{5-6} = 1$ kΩ which are calculated by assuming a graphene sheet resistance of 1 kΩ at high carrier density. Contact resistances also reveal that there is break in the graphene flake between F4 and F5 which is not uncommon in graphene devices and mostly happens during the fabrication process.

Figure 3.12 shows the results of the measurements done on this device. Prior to

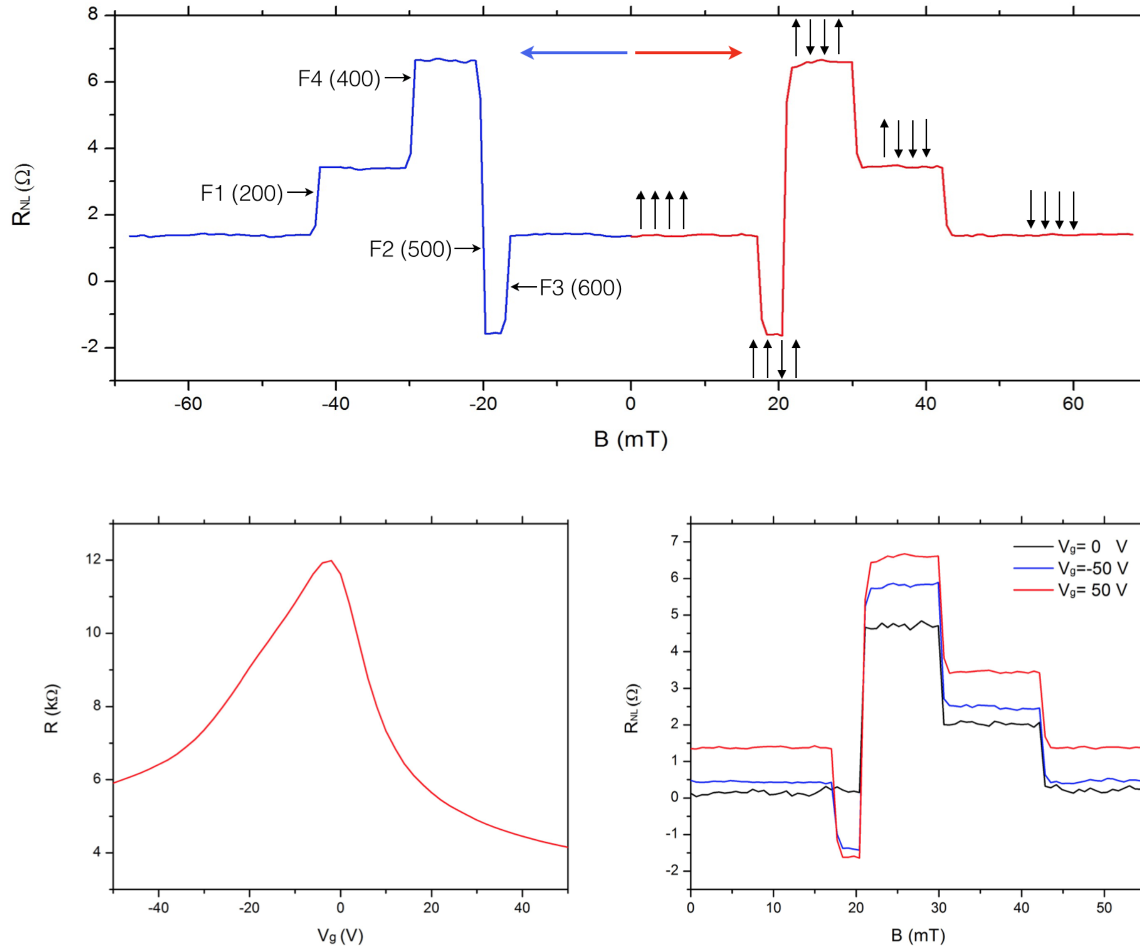

Figure 3.12: (top) Graph showing non-local resistance levels for forward (red) and backward (blue) magnetic field sweeps. Arrows and text on the blue curve shows the relevent contacts which switches it's magnetisation direction. Vertical arrows on the red curve shows the magnetization direction of the four contacts (F1, F2, F3, F4) at each non-local resistance level. (bottom-left) Graph showing two contact resistance of the section F1-F4 as a function of backgate voltage. The Dirac point can be seen at -2 V. (bottom right) R_{NL} as a function of B for three different gate voltages.

non-local measurements, the contacts are saturated at ±340 mT. The top graph shows the result of non-local spin valve measurement performed with contacts F1 (200 nm), F2 (500 nm), F3 (600 nm) and F4 (400 nm) with current injected from F2 to F1 and the resulting non-local voltage is measured between F3 and F4. The results shows three different resistance levels implying that all the four contacts are spin sensitive. Both curves also show a negative nonlocal resistance level when the contact F3 switches which is observed in only a few devices since most devices have much higher background non-local voltage. The device also shows great symmetry between switching fields for forward and backward sweeping. The bottom left of the Figure 3.12 shows two contact gate sweep

of the graphene between contact F1 and F4. The Dirac point is near -2 V and shows that graphene flake in this device is much cleaner than most of our devices whose Dirac points are usually between -20 and -40 gate voltages. It is possible that the absence of large background non-local voltage at room temperature is associated to the cleanliness of this device but further measurements on more devices have to be done to strengthen this possible connection. The last plot on the bottom right of the figure shows non-local resistance for different values of gate voltage. It is clear from the graph that near the Dirac point ΔR_{NL} is smaller compared to both electron and hole regimes. This behaviour is normally associated to transparent/pin-hole contacts and in this particular case, based on the contact resistances and ΔR_{NL} measured, the contacts are tunnel contacts with pin-holes.

In conclusion, the device 07.30_S2 shows the behaviour of tunnel contacts with pin-holes and has a maximum $\Delta R_{NL} \approx 6\ \Omega$ which is comparable to reported values [3] with similar contact characteristics. The contact resistances have increased with the increase in number of ALD cycles but tunnel barrier seems to have pin-holes. The gate sweep shows comparatively cleaner graphene with mobility reaching up to 3000 cm^2/Vs which is fairly good especially when 50% of the graphene surface is covered with contacts which are known to introduce dopants and scatterers [48].

3.8.4 Spin valve 04.16_S and 04.18_S

The fabrication recipe involving ALD process without any seed layer has many disadvantages. The devices 04.16_S and 04.18_S are chosen to demonstrate the inconsistency in the growth of Al_2O_3 on unintentionally functionalised graphene surface. This inconsistency can be clearly seen on the table given in Figure 3.13 as two contact resistance for the devices 04.16_S and 04.18_S both having the same design. The fabrication processes involved in the production of both devices were identical with the only difference between the devices being the widths of graphene flakes (1.5 μm and 2.2 μm). The table clearly shows the inconsistency in the contact resistances due to the undisciplined growth of Al_2O_3. Regardless of the resistance values, spin transport is observed in both devices.

	R_{1-2}	R_{2-3}	R_{3-4}	R_{4-5}	R_{5-6}
Two contact resistance 0416S (kΩ)	12	36	38	17	19
Two contact resistance 0418S (kΩ)	8.4	6.4	8.5	7.7	5.6

Figure 3.13: Table showing two-contact resistances for the devices 04.16_S and 04.18_S

Figure 3.14 shows some of the results of measurements done on these devices. The left graph in the figure shows the result of spin valve measurement performed on device 04.16_S for two different configurations $I_{4,3}; V_{5,6}$ and $I_{2,1}; V_{5,6}$. The widths of the contacts from contact F1 to F6 for both devices are 300 nm, 600 nm, 400 nm, 200 nm, 500 nm and 300 nm respectively. The distance between the injectors and detectors for the configuration $I_{4,3}; V_{5,6}$ is 500 nm and for the configuration $I_{2,1}; V_{5,6}$ is 2.1 μm. So this measurements is roughly a measure of the decay of spin chemical potential over distance. It is only a rough comparison because the contacts involved in two measurements are not the same and they may have different polarisations (injection/detection efficiencies). When the separation is only 500 nm the maximum observed spin signal is $\sim$8.5 Ω and it reduces to 1.5 Ω on increasing the distance to 2.1 μm. Note that this 2.1 μm long graphene channel also includes two contacts (F3 and F4) and depending on their transparency, they might induce extra spin relaxation [35]. In the blue curve which represents the configuration $I_{4,3}; V_{5,6}$, three non-local resistance levels are visible meaning all 4 contacts (F3, F4, F5, F6) are spin sensitive. But in the red curve representing the configuration $I_{2,1}; V_{5,6}$, only two resistance levels are visible since two of the contacts (F1 and F6) have the same width (300 nm). So It is impossible to say the last switching is due to F1 , F6 or simultaneous switching of both F1 and F6. Even though 500 nm wide contact has same switching field in both measurement configurations, switching events arising from 300 nm contacts are happening at two different fields (the difference is $\sim$5 mT). This can be simply due to the same inconsistency in switching fields which are common in non-local spin valves (assuming the last switching event in the red curve is caused by F6). It is also possible that the last switching on the red curve is caused by contact F1 alone and the difference in switching fields is due to the difference in edge roughness between F1 and F6 since it is known that edge roughness plays an important role in switching fields of magnetic contacts [49]. Even in the case that only one of the contacts between F1 and F6 is spin sensitive, the fact that three switching events are observed for the configuration $I_{2,1}; V_{5,6}$ means that spin transport is taking place over a distance of 3.2 μm.

The graph on the right in Figure 3.14 shows the results of measurements done on device 04.18_S. Black curves shows the two terminal gate sweeps for the parts F3-F4, F4-F5, F5-F6 and blue curve shows the change in ΔR_{NL} with respect to gate voltage for the configuration $I_{4,3}; V_{5,6}$. The difference in Dirac points for these three different sections can be due to the difference in dopant levels arising during the fabrication procedures. The minima in ΔR_{NL} around the Dirac point and the increase of ΔR_{NL} with respect to gate voltage shows transparent/pin-hole contact behaviour.

So in conclusion, it is possible to produce graphene based spin valve devices using ALD grown Al_2O_3 tunnel barrier without any functionalisation of the graphene surface. It is true that no ALD growth of Al_2O_3 happens on a freshly prepared graphene surface [21]. But in our case the un-intentional or accidental functionalisation of the graphene surface during the fabrication procedure in the form of defects induced by e-beam exposure, adsorbents, contaminants introduced from developing or residues of the PMMA make it

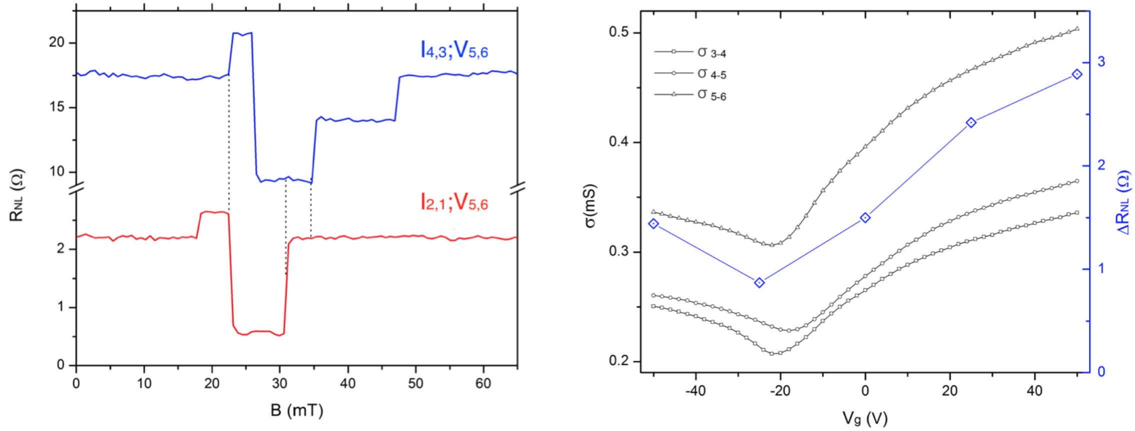

Figure 3.14: (left) Graphs showing results of non-local spin valve measurements for two different configurations. (right) Black curves shows the change in conductivity with respect to back gate voltage for different sections of the graphene flake (F3-F4, F4-F5, F5-F6). Blue data points show ΔR_{NL} for different gate voltages.

possible to grow the tunnel barrier using ALD. Since all this possible reasons are not in our control and can vary from sample to sample, it can result in reduced growth or in some cases surprisingly fast growth of Al_2O_3. This is evident in the contact resistances of the devices which varies from couple of kilo ohms to mega ohms even when the number of ALD cycles involved in the fabrication process were the same. Even though the yield of this process is high enough to produce spin valve devices, it is not good enough to produce more complicated devices like ferromagnetic-superconducting junctions. Another problem with this fabrication procedure is that even when the successful devices showed decent spin signal (ΔR_{NL}), most of them showed the behaviour of transparent/pinhole contacts and none of the devices showed the behaviour of a perfect tunnel barrier. The solution to both these problem is to add a seed layer on graphene before Al_2O_3 is grown using ALD. In fact this idea of putting a seed layer to epitaxially grow a homogeneous tunnel barrier has already been successfully demonstrated [41].

3.9 Spin injection using additional Ti seed layer

To make the growth of Al_2O_3 homogeneous and controllable, the best solution seemed to be adding a thin Ti layer before the ALD process. Ti is chosen since it is already in use for growing smooth MgO layer epitaxially for spin injection. In our devices, Ti seed layer is deposited in an e-beam evaporation system and oxidised in the same system using pure oxygen at 100 mbar for 10 minutes. The ALD system is not connected to the evaporation machine so the sample is exposed to air between the two processes. Several thicknesses of

Ti layer and different number of cycles of ALD process have been tried to find a suitable combination. In the end 0.2 nm thick Ti layer and 9 cycles of ALD process showed good yield for working devices.

3.9.1 Spin valve 01.24_S

The device 01.24_S was the first device to show spin signal with the new fabrication recipe and has 8 contacts placed on a graphene flake of width 2 μm. The widths of contacts from F1 to F8 are 500 nm, 300 nm, 400 nm, 200 nm, 600 nm, 300 nm, 400 nm and 200 nm. The distance between the contacts is 500 nm. Since there was a break in the graphene flake between F5 and F6, it was only possible to do spin valve measure from contact F1 to F5. The two contact resistances are R_{1-2}=7.5 kΩ, R_{1-2}=8 kΩ, R_{1-2}=10 kΩ and R_{1-2}=9 kΩ. Some of the results of the measurements done on the device are shown in Figure 3.16. Graph on the left of figure shows the two contact gate sweep between F1 and F5 and there are two peaks visible one around -5 V and the other around -28 V. This indicates that there is a section of graphene between F1 and F5 having Dirac point at -2 V and another section having Dirac point around -28 V. On the right of the figure shows the non-local resistance as a function of in-plane magnetic field for the configuration 3I2;4V5 and the three different resistance level shows that all four contacts are sensitive to spin current. This also means that contact F5 is able to detect the diffusing spins from contact F2, implying that spin transport is taking place over a distance of 2.1 μm.

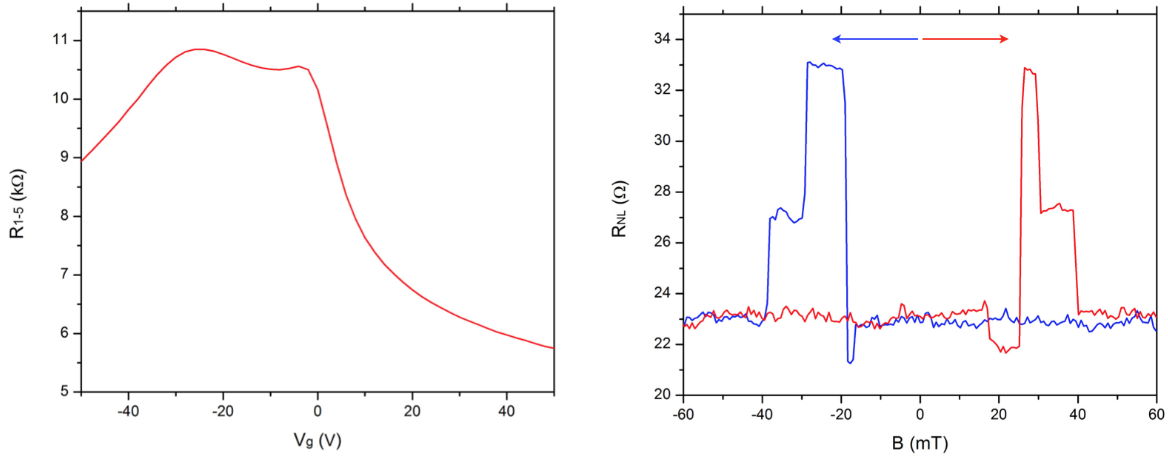

Figure 3.15: (left) Two termnial resistance of the graphene flake between contact F1 and F5 as a function of gate voltage. (right) Result of the non-local spin valve measurement with current injected from F3 to F2 and non-local voltage measured between F4 and F5. Red and blue arrow show the magnetic field sweeping direction.

3.9.2 Device 08.08_S1

The device 08.08_S1 is not a typical spin valve device as discussed before. The device consists of ferromagnetic and superconducting contacts placed on a graphene flake of average width 1.5 μm. A complete discussion and results of this device will be done at later part of this thesis and here, only ferromagnetic contacts and spin transport taking place between them alone are discussed. The device consists of four ferromagnetic contacts and four superconducting contacts placed in a fashion shown in Figure 3.16. There are specific reason for arranging contacts in this fashion but what is important in this section

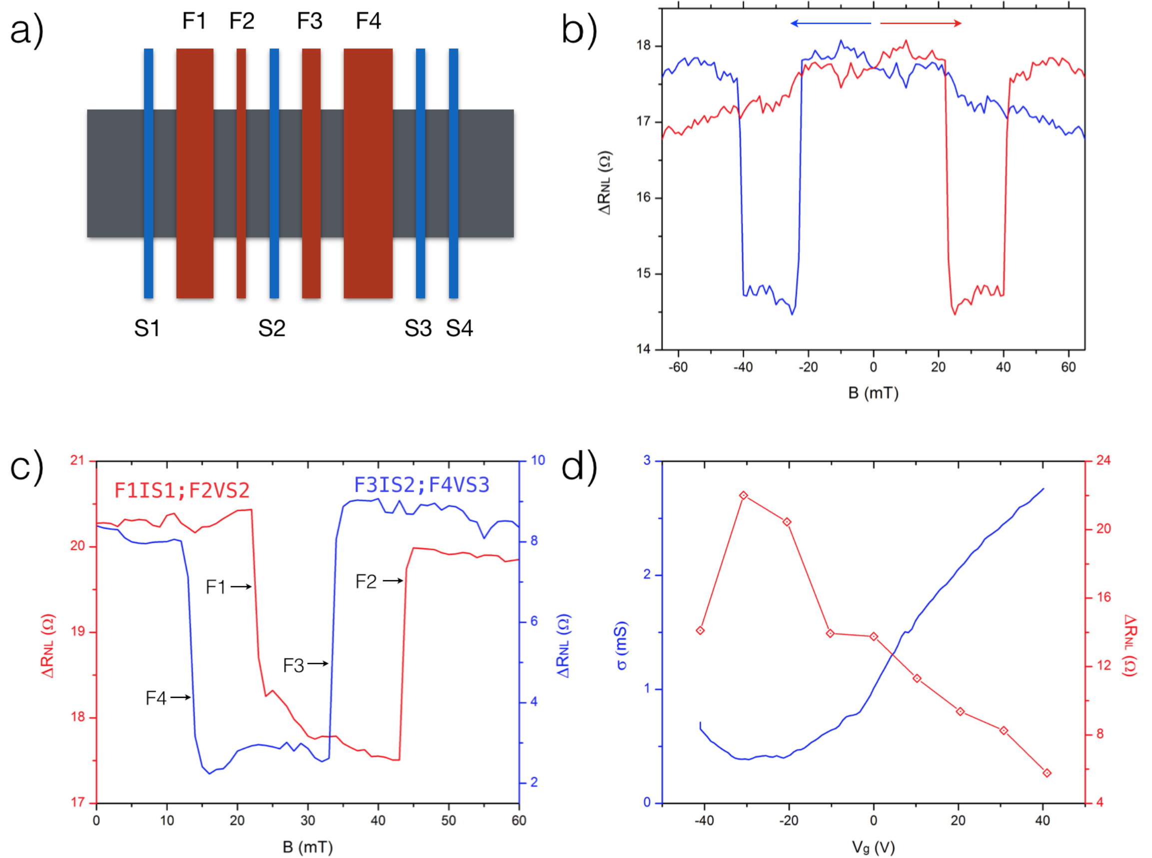

Figure 3.16: (a) Simplified design of the device 08.08_S1. Grey areas represent graphene flake. Red and blue stripes represent ferromagnetic and superconducting contacts respectively. (b) Graph showing the result of non-local spin valve measurements done at 4 K. Red and blue arrows represent magnetic field sweeping directions. (c) Graph showing the result of non-local measurements for the configuration $I_{F1,S1}; V_{F2,S2}$ (red) and $I_{F3,S2}; V_{F4,S3}$ (blue) respectively. Switching fields of the contacts are also shown. (d) Graph showing the conductivity of the graphene section between S1 and S2 as a function of gate voltage. Also shown in the change in ΔR_{NL} with back gate voltage.

is that the non-local spin valve measurements can be done for two configurations namely $I_{F1,S1}; V_{F2,S2}$ and $I_{F3,S2}; V_{F4,S3}$. The widths of the ferromagnetic contacts from F1 to F4 are 500 nm, 200 nm, 300 nm, and 600 nm. The separation between F-F and F-S is 250 nm and 100 nm. All superconducting contacts have a width of 200 nm. Measurements on this device are done in a helium cryostat with the capability of reaching the temperature ∼1.5 K by pumping the helium surface. Even though the superconducting contacts are involved in the measurements, care has been taken to apply a bias much higher than the superconducting gap (3 meV for bulk niobium) so that the transport is taking place above the gap. Also the minimum current used for the spin valve measurements is 1 μA which is well above the critical current of niobium. For these reasons they are considered as normal contacts in the discussion of spin transport in this section.

Figure 3.16(b) shows the results of the spin valve measurements for the configuration $I_{F1,S1}; V_{F2,S2}$ done at 4 K. Similar to all the other measurements, the contacts are saturated at high magnetic field (in this case 400 mT) prior to the measurement. Since only two magnetic contacts are involved in the configuration, only two switching events are observed. The two non-local resistance levels visible in both field sweeping directions represent parallel and antiparallel alignments of the contacts F1 and F2. Figure 3.16 (c) shows the result of similar measurement for both configurations at 1.5 K and and the switching fields for all four contacts can be easily seen. Lastly, Figure 3.16 (d) shows ΔR_{NL} as a function of gate voltage (red curve) for the configuration $I_{F1,S1}; V_{F2,S2}$. The graph also shows the conductivity of the section of graphene flake involved in the measurement (blue curve). ΔR_{NL} has a maxima around -30 V which is close to the Dirac point of the graphene and then ΔR_{NL} decreases with increase in conductivity. This behaviour is already discussed in section 3.7.1, and shows that the contacts F1 and F2 indeed are proper tunnel contacts. This deduction is also consistent with the fact that the device also shows a maximum ΔR_{NL} of ∼22 Ω which is the highest observed in all of our devices. The maximum calculated mobility for the device at 1.5 k is ∼ 4000 cm^2/Vs.

In conclusion the device 08.08_S1 shows good spin signal and magnetic contacts shows the behaviour of a perfect tunnel contacts. Assuming a spin relaxation length of 2.5 μm for tunnel contacts [36] gives a polarisation 10%-12% for the ferromagnetic contacts by using the equation 3.9. The fabrication of the spin valve devices with the use of Ti seed layer has increased the yield of working devices from 20% (with to Ti seed layer) to 50%. Also the the ambiguity in the contact resistance values also has gone down considerably since the ALD growth of tunnel barrier occurs in a much more controlled fashion.

3.10 Conclusion and Outlook

The primary intention of this part of the thesis is to produce a fabrication recipe to successfully contact graphene with ferromagnetic contacts with a high yield which will allow to accommodate superconducting contacts to the device to form ferromagnetic-

superconducting junctions. A high yield and a good understanding of the fabrication process is necessary to produce such devices since certain steps in the fabrication process can be incompatible. The maximum reported values of the yield of working contacts at the time of developing our recipe was around 30% [6]. It is illogical to start making complicated devices such as F/S junctions with such low yield for ferromagnetic devices knowing that each fabrication step will only reduce the total yield. Also all contacts in an F/S devices have to be working to do proper meaningful measurements. This is why it was decided to use ALD since in principle, ALD can produce ultra-thin homogeneous tunnel barriers. As explained before, in the case of graphene, this idea found to be difficult to implement [50]. But from our experience it was found that the un-intentional, unwanted functionalisation of graphene surface during the fabrication process can be a temporary solution. Many devices were successfully produced using this method and showed decent spin signal with an overall working contacts yield of 20%. Assuming reported spin relaxation lengths of 1.2 μm- 2 μm [3, 6, 51, 52] for transparent/pinhole contacts, the devices discussed in this chapter shows 3%-15% spin injection/detection efficiency with lowest value for the device 03.26_S. The unpredictability in contact resistance coming from the uncontrolled growth of Al_2O_3 which at times gave no growth at all forced us to introduce a very thin (0.2 nm) Ti seed layer with which the growth can be controlled. The new fabrication recipe has a yield above 50% and also reduces the divergence in the contact resistance from sample to sample. The device 01.24_S was the first device to show spin transport with the new fabrication recipe and has a spin injection/detection efficiency of $\sim$15%. On the other hand device 08.08_S1 shows an efficiency of 10% even though it shows proper tunnel contacts character. This is probably due to the very short distance between the ferromagnetic contacts (250 nm). In order to deduce quality parameters for spin transport it is best to have the distance between the injecting and detecting contacts to be much larger than the contact widths so that the transport is mainly taking place in section of graphene free of contacts.

It is important to mention the deviation in the switching fields of contacts from sample to sample and sometimes also in the same device for successive measurements. Even though not regularly, it is also observed that a single contact switches in two steps giving two step-like features in non-local measurements. The switching fields of these micro contacts mainly depends on parameters like size, thickness, and shape [53, 54]. But it also depends on subtle parameters like edge roughness [49, 55], surface roughness [56, 57] and partial oxidation [58]. So the deviation and asymmetry in coercivity of the contacts are expected since these parameters are difficult to control. All our devices are covered on top with a thin layer of Au but the sides are exposed and can easily get oxidised. In fact it is observed that contact resistance of our spin valve devices increases rapidly over time if they were exposed to air and the rate of increase goes down with the quality of vacuum in which it is kept. Also cobalt oxide is antiferromagnetic at lower temperatures. So one can expect higher inconsistency in coercivity of the contacts when measurements are done at cryogenic temperatures.

In most of our devices, the charge neutrality point is shifted to negative gate voltages which shows that graphene is electron doped. This is not surprising since contacts are known to shift the charge neutrality point [48, 59] and in our case due to the smaller distance between the contacts (500 nm in most cases), $\sim 50\%$ of graphene surface is covered by contacts in a typical spin valve device. Another important point to mention is the background non-local voltage visible in most of the spin-valve measurements. This background voltage can be huge at times and is caused by non-uniform current flow through the inhomogeneous tunnel barriers [60] and thermoelectric effects [61, 62]. This point takes the discussion back to the need for homogeneous tunnel barriers. A thicker oxide layer has a better chance of being pin-hole free but it may not be able to inject/detect spins. In our case the window of contact resistance for working devices is between 1 and 50 kΩ. But it is important to note that contact resistance alone does not represent the quality of the tunnel contacts. It is possible to have a high resistive contacts with inhomogeneous, rough tunnel barrier with lots of pinholes which severely affects the quality of the device.

In conclusion, A high yielding fabrication process is developed to contact graphene with ferromagnets for spin injection/detection. A high yield is the most important factor in our case since the ultimate aim is to produce ferromagnet-superconductor junctions on graphene and we have succeeded in doing so. The amplitude of the spin signal measured suggests that the efficiency of the contacts and spin relaxation lengths are similar to the reported values having similar design. But there is also room for improvement in terms of quality of the contacts with the most important being in producing homogeneous pin-hole free tunnel barriers. In the current fabrication recipe, the Ti seed layer of thickness 0.2 nm is deposited using an e-beam deposition system. A better way of doing this will be to sputter Ti which will give a more homogeneous distribution of Ti particles on graphene surface. Also at the moment, sample is exposed to air between Ti seed layer deposition and ALD growth which can reduce the yield and quality of the devices. So sputtering Ti and then moving the sample to ALD without breaking the vacuum is expected to increase the quality and yield of the devices further. Also our own recent experiments shows that increasing the Ti thickness decreases the surface roughness of Al_2O_3 dramatically but the contact resistances shoot up to mega ohms with out showing any spin signal. So by adjusting the Ti layer thickness and the number of ALD cycles, a smoother, closed Al_2O_3 tunnel barrier along with moderate contact resistance can probably be achieved.

Chapter 4

Ferromagnet-superconductor junctions on graphene

4.1 Introduction

On April 8th 1911, Heike Kamerlingh Onnes, a dutch physicist of Leiden university observed a complete lack of electrical resistance in mercury when it was cooled to 4.2 K [63]. This phenomenon of absence of resistance in certain materials under certain critical temperature (T_C) and magnetic field is called superconductivity and Kamerlingh Onnes received the nobel prize for physics in 1913 for it's discovery. The discovery of superconductivity opened the gates to a large,unexplored section of physics and also became the corner stone for many technological applications. Magnetic resonance imaging (MRI), nuclear magnetic resonance (NMR) and superconducting quantum interference devices (SQUIDs) are some of the most important ones to name.

4.2 Basics of superconductivity

In normal conductors electrical current is carried by free electrons. But in a superconductor, current is carried by a two electrons bound system called Cooper pairs. Cooper pairs are formed by the coupling of two electrons having properties $(k, E_k, \uparrow)$ and $(-k, E_k, \downarrow)$ where k, E_k represents the momentum vector, energy and the arrows represents the spin of electrons. When an electron passes through a crystal lattice, it can give or take energy and momentum to/from the lattice and change the vibrational state of the lattice. This change in vibrational state of lattice can said to be caused by emitting/accepting a phonon. In a superconductor the passage of an electron through a lattice area changes the position of ions in a way that the second electron passing through feels an attraction/acceleration towards the first electron. In another words, the first electron emits a phonon which is absorbed by the second electron. In this way two electrons are bound together as one entity called "Cooper pair" through lattice mediated phonon. Explan-

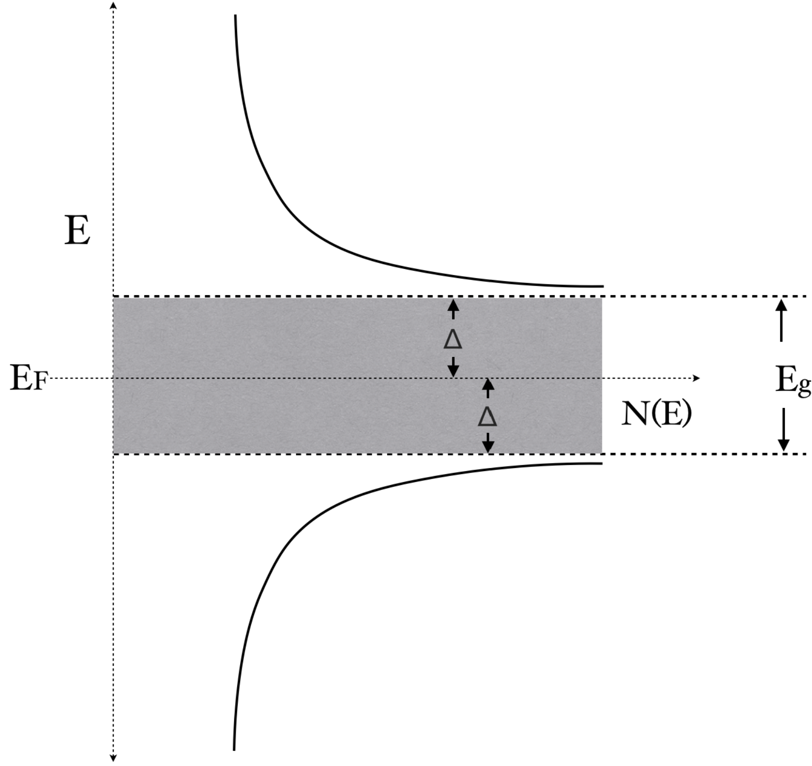

Figure 4.1: Density of states in a superconductor

ation and properties of superconductivity based on this idea was preposed by Bardeen, Schrieffer and Cooper in 1957 [64]. One of the main prediction of the theory was the formation of a band gap, inside which there are no single electron states. According to BCS theory, at T=0 the band gap is given by

$$E_g = 2\Delta = 3.528 K_b T_c \tag{4.1}$$

where K_b is the Boltzmann constant and T_c is the critical temperature of the superconductor. The superconductivity is destroyed by heating the superconductor above T_c or by applying an external magnetic field. Upon increasing the temperature the width of the gap barely changes near T=0 but near the vicinity of T_c the width of gap reduces dramatically and reaches zero at T=T_c . The temperature dependance of the gap in the vicinity of T_c is given by the following equation

$$\frac{\Delta(T)}{\Delta(0)} = 1.74 \left(1 - \frac{T}{T_C}\right)^{1/2} \tag{4.2}$$

Superconductors also show perfect diamagnetism which was observed by Meissner and Ochsenfeld in 1933 and hence known as Meissner effect. This means that any magnetic

field is excluded from the interior of a bulk superconductor. Not only that, if there was any field present inside the superconductor when it was in it's normal state, upon cooling through T_c, this field will be expelled from the interior. The extend to which the external magnetic field can penetrate the superconductor is decided by the London penetration length (λ). The field in the exterior of a superconductor is given by

$$B(x) = B(0)e^{-x/\lambda} \tag{4.3}$$

Where x is the distance measured from the surface of the superconductor. But if a large enough external magnetic field is applied, smiler to the effect of increase in temperature, the superconductivity vanishes. This minimum magnetic field required to destroy the superconductivity is known as critical magnetic field (Hc). Another important length scale related to superconductivity is the coherence length (ξ) introduced by A. B. Pippard. If any spatial change is made in superconductor properties such as the number density of electrons in superconducting ground state, it may only be visible up to the coherence length of the superconductor. In another words, coherence length defines the length up to which one can observe the intrinsic nonlocal properties of the superconductor. The coherence length is given by the formula,

$$\xi = a\frac{\hbar V_F}{K_B T_C} \tag{4.4}$$

Where V_F is the Fermi velocity and a is the numerical constant and has an approximate value of 0.18 (according to BCS theory).

4.3 Andreev reflection

Consider an electron approaching a normal conductor/superconductor interface from the normal conductor side. Let's assume that T=0, so that all single electron states up to Fermi energy (E_F) are filled on the normal conductor side and on the superconductor side, an energy gap is formed with $Eg = 2\Delta$. The only way the incident electron can enter to the superconductor is by forming a Cooper pair with another electron having equal but opposite momentum and spin. Assuming the incident electron has an energy ϵ (above the Fermi energy) and a momentum vector ke_1, it picks up another electron from the interface with energy $-\epsilon$ and momentum $ke_2 = -ke_1$ (also opposite spin). This process creates a hole in normal conductor with energy $-\epsilon$ and momentum $k_h = -ke_2$ meaning it's momentum vector is in the same direction as of the incident electron. Since the hole has negative effective mass, it's velocity will be opposite to that of the incident electron. So in effect, it will retrace the path of the incident electron. Note that the energy of the reflected hole ($E_F - \epsilon$)) is decided by the energy of the incident electron ($E_F + \epsilon$). Also during this process every incident electron drags a secondary electron from the normal

conductor to form Cooper pair and there by increasing the conductivity by two folds. This peculiar reflection process was first preposed by the Russian physicist Alexander F. Andreev in 1964. Like in any other scattering process, energy, momentum and charge have to be conserved during the process. Applying those conditions, one can see that the change in momentum between the incident electron and the reflected hole Δk, which is picked up by the Cooper pair, is decided by the difference in energy between the two. This difference in energy $\Delta E = 2\epsilon$ is maximum when $\epsilon = \Delta$. Using this information one can derive the length scale over which the incident electron and the reflected hole is "in phase". The two are in out of phase when their relative phase difference becomes $\Delta\phi = \pi$. This happens when the hole travels a distance $L = \pi/\Delta k$. Following in this path one can derive the relation for the superconducting phase coherence length (L_ϕ) in normal conductor for the ballistic transport regime.

$$L_\phi = \frac{hV_F}{\pi\Delta} \tag{4.5}$$

Where h is the Planck's constant and V_F is the Fermi velocity. For diffusive transport the relation modifies to,

$$L_\phi(D) = \sqrt{L_\phi \, l_e} \tag{4.6}$$

Where l_e is the elastic mean free path of the normal region.

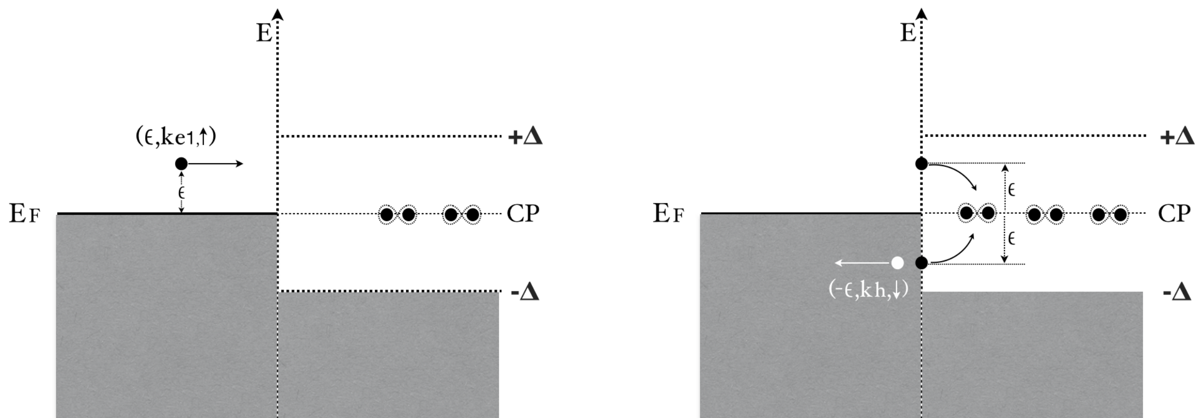

Figure 4.2: Andreev reflection process. Electrons are represented by black dots and holes by white dots. The vertical doted line represent the interface of normal conductor and super conductor.

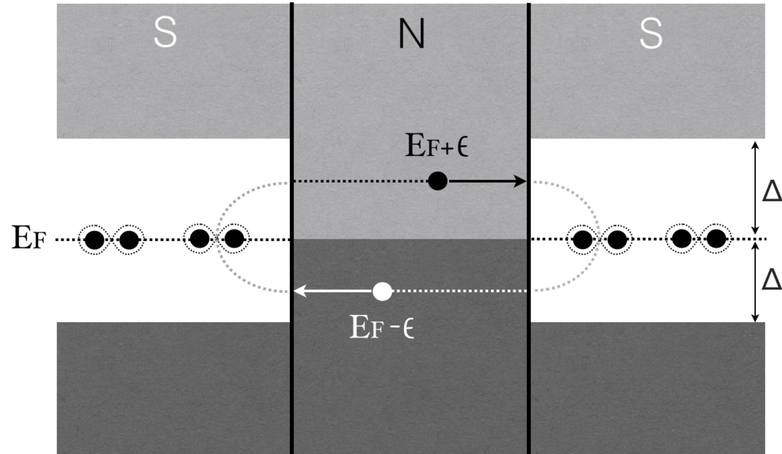

Figure 4.3: Formation of Andreev bound states. Electrons are represented with black dots and holes by white dotes. The darker region represents the filled states and the ligter areas represents unfilled states.

4.3.1 Multiple Andreev reflection and Andreev bound states

Figure shows a superconductor/normal conductor/superconductor junction (S/N/S) where a normal conductor is sandwiched between two superconductors with the thickness of the normal conductor comparable or less than the superconducting phase coherence length of the normal conductor L_ϕ. As explained earlier, an electron with an energy $E_F + \epsilon$ approaching the superconductor from the normal conductor is retro-reflected as a hole. But in the case of S/N/S junction, the hole having energy $E_F - \epsilon$ travels towards the superconductor on the left and upon reaching the S/N interface breaks a Cooper pair to free up an electron with energy $E_F + \epsilon$. This electron travels towards the superconductor like the previous electron and the whole process repeats. This perpetual reflections in effect transports Cooper pairs from one superconductor to another through a normal conductor is called Andreev bound states. Andreev bound states facilitate the flow of dissipation less supercurrent (I_S) which is dependent on the phase difference (ϕ) between the superconducting electrodes through the relation $I_S = I_c \sin\Delta\phi$. If the current is more than the critical current I_C, a dissipative current flows between the superconductors with a measurable voltage drop across the junction.

Assume an initial voltage difference between the S electrodes higher than $2\Delta/e$ which is then slowly decreased. When $V > 2\Delta/e$ there are two possible reflection processes. One is the normal quasiparticle transport represented in the Figure 4.4 as n=0 and the other is the single Andreev reflection represented as n=1. When the voltage difference is further decreased and is in the region $\Delta < eV < 2\Delta$, normal quasiparticle transport cannot occur but a second order Andreev reflection (n=2) is possible as shown in the figure. Andreev

reflection continues to happen whenever V equal $2\Delta/n$ where n=1,2,3.... These multiple Andreev reflection can be seen as sub gap conductance peaks in differential conductance measurements [65, 66].

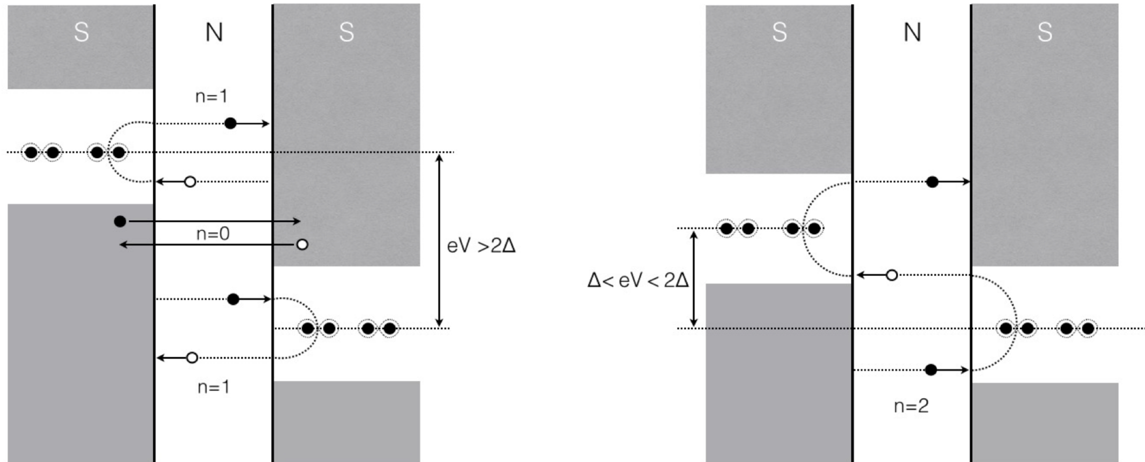

Figure 4.4: Multiple Andreev reflection processes. (left) When the voltage difference is slightly higher than 2Δ, quasiparticle transport takes place between the normal regions of the superconductor (n=0). Also possible is the first order Andreev reflection (n=1). (right) when V is higher than Δ but smaller than 2Δ, normal transport is firbidden but a second ordrer Andreev reflection is possible. An electron incident on the second superconductor is reflected as a hole with an energy enough to enter to the gap of the first superconductor. The hole then breaks up a Cooper pair and frees an electron which then travel towards the second superconductor.

4.4 Specular and retro reflections

As discussed above, Andreev reflection in general is retroreflective. But in the case of graphene both retroreflection and specular reflection can take place depending on the position of Fermi level. Consider an electron with energy $E_F + \epsilon$ approaching a superconductor from a single layer graphene sheet. In order for Andreev reflection to happen, this electron with wave vector $+k$ needs to couple with second electron with momentum vector $-k$ and energy $E_F - \epsilon$. If $\epsilon < E_F$, both the electron and the reflected hole are from the conduction band. So the reflected hole has velocity components opposite to that of the incident electron, meaning the hole is retracing the path of the electron. So when $\epsilon < E_F$ retroreflection will take place with electrons with opposite momentum vector coming from two different valleys K and K'. So retroreflection in graphene is an intraband process.

But when $E_F < \epsilon$, the second electron or the reflected hole comes from the valance band as shown in the Figure 4.5. For Andreev reflection to happen momentum along the interface has to be conserved. Since the velocity of valance electrons are parallel to the wave vector, the y component of the electron and hole stays the same. In order to conserve the momentum in the x direction the x component of the velocity of the hole changes sign as shown in the figure. Specular Andreev reflection in graphene is an interband process. It is also important to mention that for any Andreev reflection to occur, both E_F and ϵ have to be smaller than Δ.

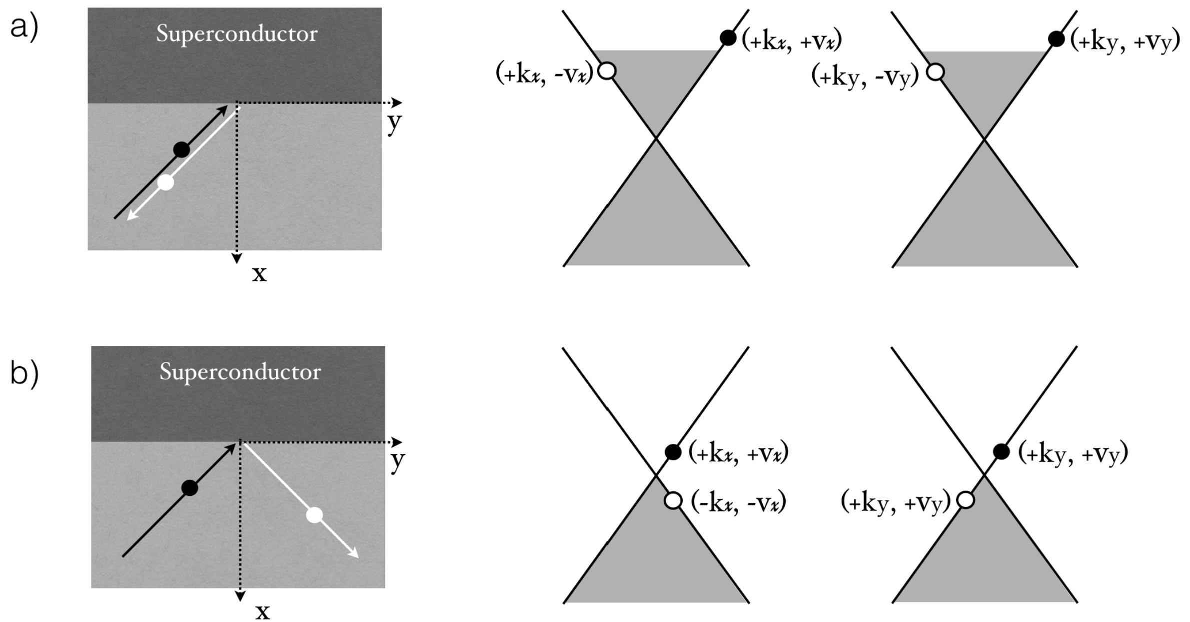

Figure 4.5: Andreev retroreflection (a) and specular reflection (b). In the band diagrams, shaded area represents the filled states.

4.5 Ferromagnet-superconductor junction

Interplay between a superconductor and ferromagnet can give rise to rich physics. One of the recent findings is the long spin relaxation lengths measured in superconductors [68,69]. Many comparatively new physical phenomenas can be studied by injecting spin polarised current in to a superconductor. Some of those effects are suppression of Andreev reflection [67,70], crossed Andreev reflection [71,72], elastic cotunneling and spin imbalance [68,73]. One of the first pioneering work in combining ferromagnet and superconductor was done by P.M Tedrow and R. Meservey [67] in ferromagnet/insulator/superconductor junctions (F/I/S). When a superconductor is placed in an external magnetic field, the spin magnetic

moments of quasiparticles near the edge of the superconducting gap will interact with the magnetic field. This results in shifting of density of states in the superconductor. If H is the external magnetic field and μ is the magnetic moment of electron, then the states shifts by $\pm\mu H$ depending on the spin quantum number of the states as shown in the Figure 4.6. Prior to the application of the magnetic field the superconducting gap was from $E_F - \Delta$ to $E_F + \Delta$ ($Eg = 2\Delta$). But in the presence of field, edges of the gap for spin up states are now at $(E_F - \Delta) + \mu H$ and $(E_F + \Delta) + \mu H$. Similarly gap edges of the spin down states are at $(E_F - \Delta) - \mu H$ and $(E_F + \Delta) - \mu H$. This asymmetry in the density of states in superconductor can be seen in the differential conductance measurement also shown in Figure 4.6. At zero magnetic field the conductance curve is symmetric with respect to zero as seen in figure. The conductivity goes to zero inside the gap since there are no single electron states. The increased conductivity before and after the gap is due to the increased density of states near the superconducting gap (Figure 4.1). In an external field, whenever the bias voltage is in line with the top or bottom of the spin up/down density of states, an increased conductance can be seen in the conductance spectra as expected. The asymmetry in the curve which can be better seen between position 'a' and position 'b' in the curve is due to the asymmetry in the ferromagnet density of states. In a ferromagnet there are more spin up electron states than spin down electron states (or vice versa) near the Fermi level giving rise to a net polarisation. By measuring this asymmetry in the conductance curve, the spin polarisation of the ferromagnet can be estimates as described in the report [67].

Even though this report gives a good technique to measure the spin polarisation of ferromagnets, there is one major drawback. The ferromagnet whose polarisation needs

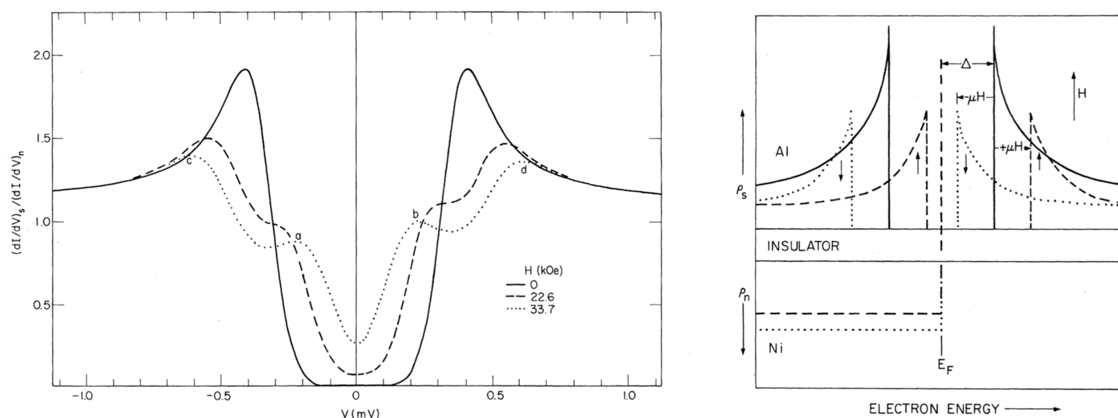

Figure 4.6: (left) Normalised conductance spectra of the F/I/S junction as a function of bias voltage. (right) Spin density of states in an external magnetic field of the superconductor. Dashed lines represent spin up states and dotted lines represent spin down states. Figure taken from [67].

to be measured has to be made in the form of F/I/S junctions and producing a thin homogeneous tunnel barriers is not an easy task. Also certain materials may not be suitable to be made in this format. R.J Soulen Jr *et al.* [70] has reported an alternative to this method to measure the spin polarisation known as “Andreev spectroscopy”. The underlying principle of this method is the fact that in an F/S junction the probability of Andreev reflection depends on the amount of polarisation of the ferromagnet. As explained earlier, in order for Andreev reflection to happen the incoming electron needs to find second electron with opposite spin to enter to the superconductor as Cooper pairs. As shown in the left of Figure 4.7, if the metal is completely polarised the probability of Andreev reflection is obviously zero and probability goes higher with decrease in polarisation. Soulen Jr *et al.* [70] realised this idea by making point contact between ferromagnet and superconductor. These point contacts allow coherent two particle transmission at the interface unlike the tunnel junction mentioned before. The effect of polarisation of the ferromagnet on Andreev reflection probability can be seen experimentally in a conductance measurement. The right of the Figure 4.7 shows the normalised conductance of different materials (point) contacted by superconductor. Cu for example has P=0 and the conductance reaches two times the normal conductance due to the occurrence of Andreev reflection. The amplitude of the sub gap conductance then goes down with materials with increasing polarisation. In the point contact method, the polarisation is defined as follows

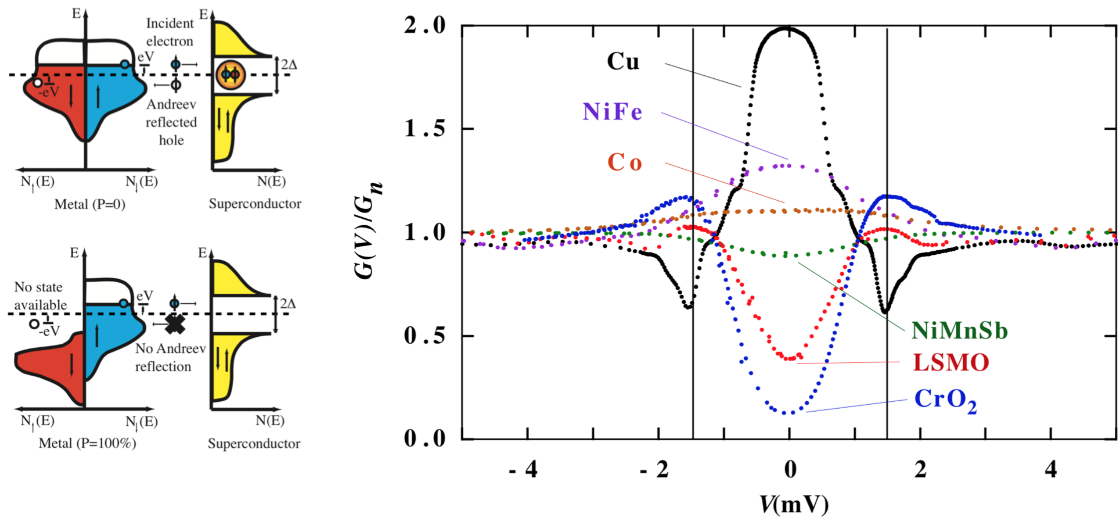

Figure 4.7: (left) Figure shows how the probability of Andreev reflection in an F/S junction depends on the polarisation of the ferromagnet. (right) Graph showing normalised conductance of the junction as a function of bias voltage for different materials. Figures are taken from [70].

$$P_C = \frac{I\uparrow - I\downarrow}{I\uparrow + I\downarrow} \tag{4.7}$$

Where $I\uparrow$ and $I\downarrow$ are the spin up and spin down currents between the materials. If there is no interfacial scattering and the temperature is close to zero, the polarisation is related to conductance at zero bias as

$$\frac{1}{G_n}\frac{dI}{dV} = 2(1 - P) \tag{4.8}$$

Where G_n is the normal state conductance.

Other than these effects there are other nonlocal effects which can be detected in F/S/F or N/S/N double junctions. Crossed Andreev reflection, elastic co tunnelling and spin/charge imbalance in the superconducting quasiparticle density of states are some of the important ones.

4.5.1 Crossed Andreev reflection

Crossed Andreev reflection (CAR) is quite similar to normal Andreev reflection except for the fact that the reflected hole is from a second contact. So in a ferromagnet/superconductor/ferromagnet junction (F/S/F) or normal conductor/superconductor-/normal conductor junction (N/S/N), the incident electron from the first ferromagnet or normal conductor couples with a second electron with opposite spin from the second ferromagnet or normal conductor to form Cooper pair in the superconductor. In an N/S/N junction with electrons injected from a normal contact to the superconductor, if successful CAR is taking place, meaning the electrons from the second normal conductor are coupling with the injected electrons to enter the superconductor, a negative non local voltage can be measured between the superconductor and the second normal conductor [71]. But what is also possible is the tunnelling of electron from the first normal contact to the second one without producing a hole in the second normal contact which is known as elastic cotunneling (EC). Since the EC produces nonlocal voltage with positive sign on the second junction, the sign of the nonlocal voltage measured in an experiment will depend on the probability of CAR and EC and if both have equal probability, the nonlocal voltage might disappear. CAR has been reported in both N/S/N tunnel junctions [71] and F/S/F point contacts [72]. It is important to mention that in order for CAR to happen the distance between the superconductor and normal/ferromagnetic contacts has to be comparable to the superconducting phase coherence length.

mFigure 4.8 shows the appearance of both CAR and EC in a nonlocal measurement reported by S. Russo *et al.* on Nb/Al double tunnel junctions. The experiment is carried out by passing a current from the first normal contact to the superconductor and measuring corresponding nonlocal voltage. In their main result which is shown in Figure 4.8, the nonlocal voltage is zero above 700 μV probably because EC and CAR cancel each other (note that the measured Δ was 900 μV). At bias voltages between 700 μV and 270 μV the nonlocal voltage is negative due to the occurrence of CAR and afterwards nonlocal voltage changes sign and increases until it reaches zero bias voltage which shows the

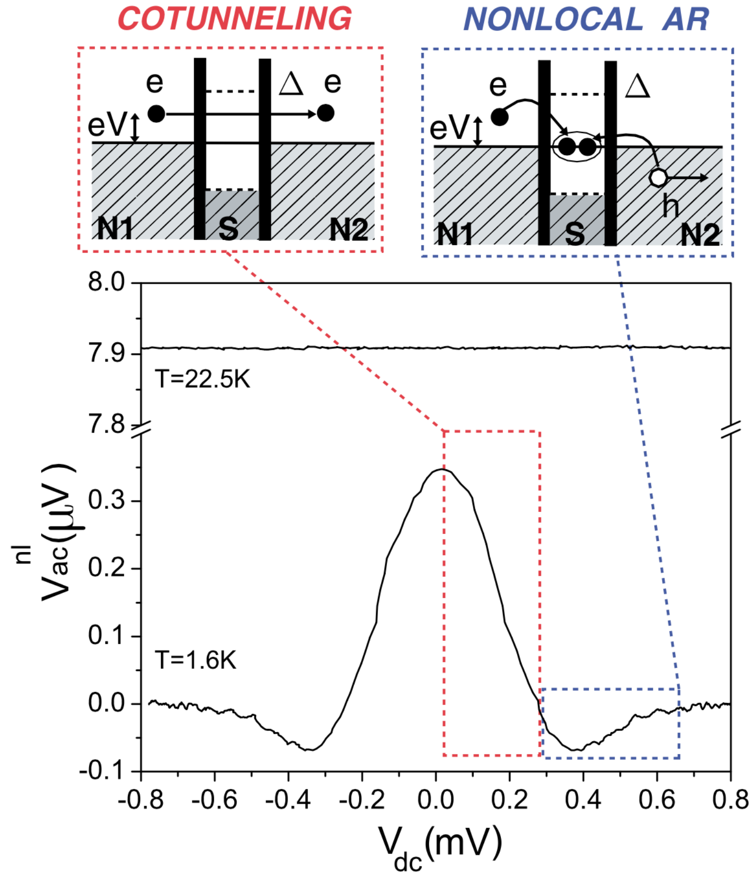

Figure 4.8: Figure taken from [71] shows ac nonlocal voltage as a function of dc bias voltage. Measurement is carried out by adding a small ac voltage on top of the dc bias voltage. Carresponding nonlocal ac voltage is then measured while the dc bias voltage is swept slowly. Also shown in the figure is the processes EC and CAR.

dominance of EC. If instead of normal contact ferromagnets are used one can presumably control EC or CAR by aligning ferromagnets parallel or antiparallel.

CAR is also verified independently by Beckmann *et al.* [72] in a device consists of a superconducting aluminium bar contacted by multiple iron wires of different widths. This allows them to control the magnetisation direction of the iron wires independently. In this measurement, a small current of amplitude 50 nA is injected from one ferromagnet to superconductor and the corresponding nonlocal voltage is measured between the second ferromagnet and superconductor. For each magnetization configuration, the sample is cooled through the transition temperature. The main finding of the report is the two resistance levels detectable for parallel and antiparallel configuration below the superconducting transition temperature.

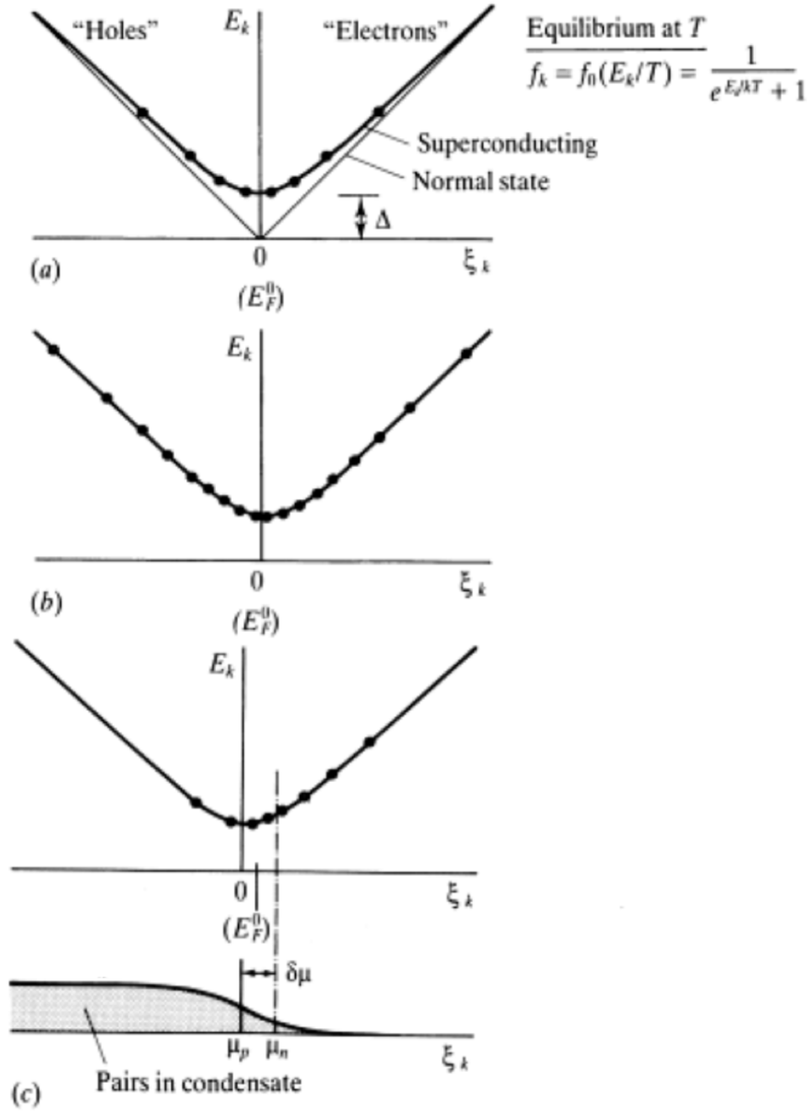

Figure 4.9: (a) Quasiparticle energy spectrum at normal and superconducting state with dots representing ccupation of quasiparticles. (b) Evenly excited population due to nuetral excitations. (c) Oddly excited population spectrum due to charged perturbations giving rise to charge imbalance. μ_p (chemical potential of the condensate) and μ_n (quasiparticle chemical potential) shifts relative to the equilibrium value E_F^0 since total number of particles are conserved. Figure taken from [74].

4.5.2 Spin imbalance

According to BCS theory, in a superconductor Cooper pairs are formed by electrons having equal and opposite momentum and spin. The ground state of this superconductor at T=0 is a condensate of Cooper pairs. The energy of the single particle excitation is given by $E_k = \sqrt{\Delta^2 + \xi_k^2}$ where ξ_k is the quasiparticle energy in the normal state. With

respect to the Fermi energy, ξ_k can be written as $\hbar^2 k^2/2m$. In thermal equilibrium, the quasiparticle state above the gap is occupied according to Fermi-Dirac distribution $f(E) = 1/(e^{K_B T}+1)$ where K_B is the Boltzmann's constant. But in general, and especially in the case of non-equilibrium processes, actual occupation number $f_k \neq f_0(E_k/K_b T)$ where f_0 represents the Fermi distribution at thermal equilibrium. In the case of neutral disturbance to the system like phonons or photons, the result is similar to that of a change in temperature, which is to produce equal number of electron-like and hole-like quasiparticle in the superconductor as shown in the Figure 4.9. Also this equal production of quasiparticles affect the energy gap (Δ) in the same way as a change in temperature does (equation 4.6). On the other side, if the distortion in equilibrium is caused by charged perturbations like electron injection, then electron-like or hole-like quasiparticle can dominate and the result is a net charge in the quasiparticle density spectrum as shown in Figure 4.9. This so called "charge imbalance", if not kept in a dynamical equilibrium will relax. The charge imbalance also causes the chemical potential of the quasiparticles μ_{QP} to shift as shown in Figure 4.9. Since overall electrical neutrality needs to be maintained, μ_{QP} and μ_p (superconducting pair chemical potential) move in opposite directions [74]. Charge imbalance was first observed by Michael Tinkham and John Clarke four decades ago [75, 76].

In the discussion above, it was assumed that the quasiparticles are spin randomised and

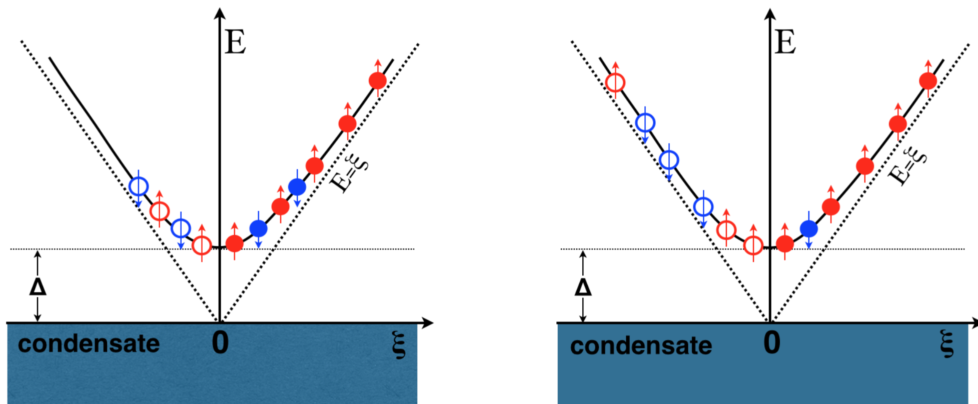

Figure 4.10: (left) Figure portraying spin imbalance along with charge imbalance in superconducting quasiparticle density of states. Dots represent electrons and circles represent holes. The total number of spin up (red) quasiparticles is more than the number of spin down (blue) quasiparticles. Also there are more electron-like quasiparticles than hole-like which create charge imbalance. (right) Spin imbalance with no charge imbalance. Eventhough there are equal number of electron-like and hole-like quasiparticles, there are more spin up quasiparticles compared to spin down quasiparticles, producing a net spin imbalance.

hence the chemical potential of spin up and spin down quasiparticles are the same. But one can imagine a situation as shown in the left part of Figure 4.10, where there are more electron-like spin up quasiparticles and thermally populated spin down quasiparticles. Now the chemical potentials of spin up and spin down quasiparticles $\mu_{QP\uparrow}$ and $\mu_{QP\downarrow}$ are not the same and there is a net spin imbalance $\mu_S = (\mu_{QP\uparrow} - \mu_{QP\downarrow})$. Also, note that there is a charge imbalance since there are more electron like quasiparticles than hole-like.

There can also be a different situation where there is spin imbalance without charge imbalance. This situation is shown on right side in Figure 4.10. Here the spin up and spin down quasiparticles occupy the states asymmetrically to create a spin imbalance but at the same time there are equal number of electron-like and hole-like quasiparticles. It is important to note that in the case of spin imbalance with charge imbalance, $\mu_P \neq \mu_{QP}$ and $\mu_{QP\uparrow} \neq \mu_{QP\downarrow}$. And in the case of spin imbalance alone $\mu_P = \mu_{QP}$ and $\mu_{QP\uparrow} \neq \mu_{QP\downarrow}$. According to Ref. [73], spin imbalance can be created either by Zeeman splitting or by injecting spin polarised current in to a superconductor. They have fabricated F/I/S/I/F lateral spin valves to measure spin imbalance with Co being the ferromagnet, Al_2O_3 the insulator and Al as the superconductor. The main result of their report is shown in Figure 4.11.

The actual experiment is conducted as follows. A spin polarised current is injected from a ferromagnet to the superconductor and the resulting nonlocal resistance is probed using a second ferromagnet. The two sharp peaks visible in the figure represents $\mu_{QP\uparrow}$ and $\mu_{QP\downarrow}$. The hight of the peaks depends on the external magnetic field since the splitting of the density of states depends linearly on the applied magnetic field. They have also shown

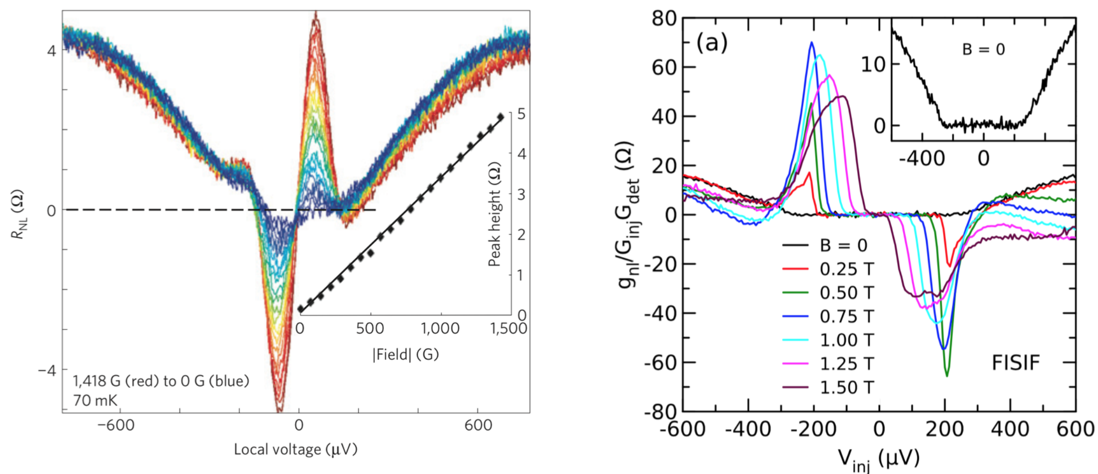

Figure 4.11: (left) Graph showing nonlocal resistance as a function of injector bias voltage. The field independant symmetric background is due to charge imbalance. Figure taken from [73]. (right) Normalized nolocal conductance as a function of bias voltage for a F/I/S/I/F device. The symmetric black curve in the incet shows charge imbalance at B=0. Taken from [68].

the reversal of the nonlocal asymmetric resistance curve upon reversal of the magnetization of the detector ferromagnet (not shown here). Another article reporting spin imbalance in superconductor is by F. Hübler *et al.* [68]. They have used ferromagnet to inject current in to superconductor having Zeeman splitting. Similarly the resulting nonlocal signal is measured by a second ferromagnet. Results of their measurement are similar to that of C.H.L Quay *et al.* The asymmetric nonlocal conductance peaks are observed and their amplitude depend on the external magnetic field (Figure4.11). Both reports show an increased spin relaxation length in superconductor compared to it's normal state. This is due to the fact that in the superconducting state, spin relaxation caused by elastic spin flips cannot occur since in the presence of external magnetic field, quasiparticle spin density of states in the superconductor have different energies [68].

Chapter 5

Characterisation of ferromagnet/superconductor junctions on graphene

5.1 Introduction

This chapter discusses the measurements performed on ferromagnet/superconductor junctions (F/S) based on graphene and the inferences that can be made by analysing the results of those measurements. All the F/S devices are characterised in a He^4 cryostat with the capability of reaching temperature down to $\sim$1.5 K by pumping on the helium surface. The devices are inserted in the cryostat in a way that the external magnetic field is parallel to the length of the contacts. All F/S devices measured have the basic design shown in Figure 5.1. But the widths of the contacts and the separation between them have changed over the time for better measurement results. The succession of the measurements done on F/S devices are as follows. After cooling to 1.5 K, differential resistance/conductance measurements are done on the Josephson junction which is at the edge of the device, formed by two superconductors and the graphene between them (as the weak link). By analysing the differential conductance spectra and the I-V curves, the transparency of the superconducting contacts, the band gap (2Δ), phase coherence length (L_ϕ) etc. can be estimated. Afterwards, nonlocal spin valve measurements are done to confirm that the ferromagnetic contacts are spin sensitive. Even though the exact polarisation of the contacts cannot be determined by this measurement, a qualitative assessment can be deduced by assuming the reported spin relaxation length (λ) values on graphene. The last set of measurements are the ones which involve both ferromagnetic and superconducting contacts.

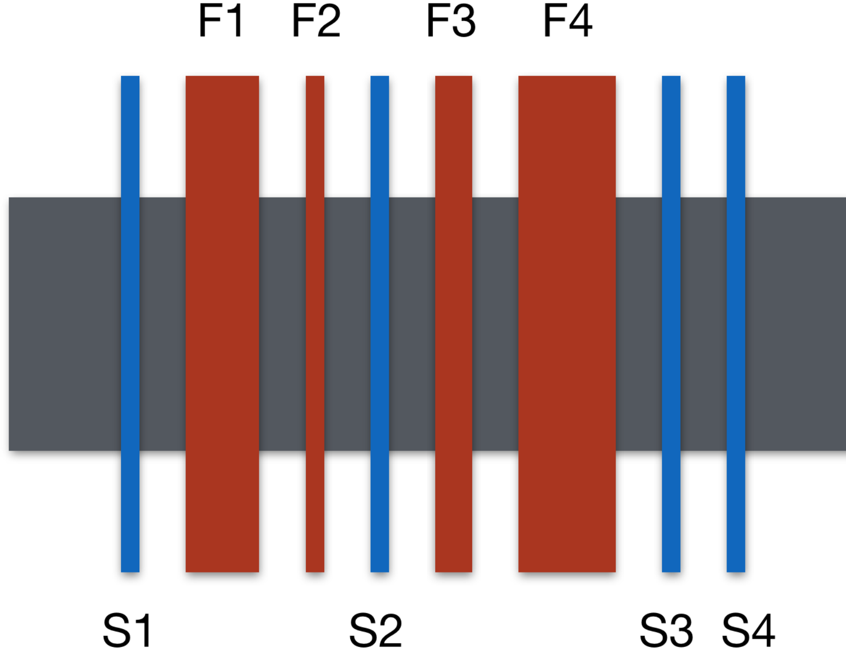

Figure 5.1: Basic design of the F/S device. The grey area represents graphene. The superconducting contacts S3 and S4 form a Josephson junction. Contacts F1, F2 and F3 F4, having widths 500 nm, 200 nm, 300 nm, 600 nm respectively form lateral spin valves and their magnetisation direction can be independantly controlled.

5.2 Josephson junction

Josephson effect is a phenomenon where a supercurrent can pass between two superconducting reservoirs which are connected by a weak link. The weak link can be a conductor or insulator and the junction formed is called Josephson junction. The supercurrent I_s that can flow between the superconductors can be written as $I_s = I_c \sin \delta\phi$, where I_c is the maximum supercurrent through the junction and $\delta\phi$ is the difference in phase of the superconducting reservoirs. The theory of transport phenomenas that happens between two superconducting contacts when connected by a normal contact is explained in chapter 4. As shown in the design of F/S device (Figure 5.1), the last two superconducting contacts (S3 and S4) form a Josephson junction with the graphene between them as the weak link. The first report on graphene based Josephson junction is by Hubert *et al.* [65] where they used Al as the superconductor and Ti as the intermediate layer which helps to increase the transparency. Later on there has been a series of articles reporting contacting graphene with Ti/Nb [77], Pt/Ta [78], PbIn [79] and W [80]. Also there is a recent report on Josephson junction where the weak link is suspended graphene [81].

As discussed in the fabrication chapter (chapter 2), the superconducting contacts

consist of from bottom to top, 5 nm Ti, 65 nm Nb, 10 nm Al and 10 nm Ru. The Ti layer helps to have a transparent interface between Nb and graphene. The thickness of the Ti layer is crucial since from our experiments, the quality of the superconducting contacts depends heavily on it. Also a recent article reports the effect of thickness of Ti layer on the interface resistance in graphene based Josephson junction [77]. In the best performed devices, Ti layer is produced by sputtering at 100 W for 65 seconds giving a thickness of ~5 nm. But several devices were made with different sputtering times to find a optimum thickness.

The selection of Nb as the superconductor is due to it's high critical field (H_C) and critical temperature (Tc). To characterise the F/S devices, an in-plane magnetic field is necessary to change the magnetic orientation of the ferromagnetic contacts. The switching fields of the contacts are usually between 10 mT - 50 mT. The low critical field of Al (10 mT) is one main reason for not choosing Al as the superconductor in the F/S devices, despite it's high coherence length. Even though many of the measurements are done at zero magnetic field, in a normal cryostat, the remnant field of the magnet itself can reach several mT which might effect the results of the measurement. The coherence length of the superconductor in the dirty limit scales with $1/\sqrt{\Delta}$. So Al which has a bulk band gap of Δ= 160 μeV, has a higher coherence length compared to Nb which has a higher band gap (Δ=1.6 meV). Even though in this regard Nb is not the best choice, the higher critical temperature (~9 K), permit Nb based devices to be characterised in normal He^4 based cryostats which is a great advantage. From our experiments, the narrowest Nb contact found to be superconducting were ~150 nm wide, and to be on the safe side, all the superconducting contacts in the F/S devices have a width of 200 nm.

Figure 5.2 shows a simplified diagram of the measurement setup. All F/S devices are measured in a normal He^4 cryostat with the possibility of applying an in-plane magnetic field. All superconducting contacts have two leads connecting them so that there are separate contacts for injecting current and detecting voltage drop. Note that even though this allows us to avoid the lead resistance from the measurement, it still includes the contact resistance between the superconductor and graphene. To do the differential resistance measurement, an ac voltage of amplitude 10 μV- 50 μV is superimposed on a dc bias voltage which is applied across the Josephson junction and the reference resistor (R_{ref}) connected in series. The reference resistor is chosen in a way that it's resistance is much higher than the junction resistance so that the measurement can be conducted in current bias mode. By measuring the voltage drop on R_{ref}, the current through the junction can be calculated since R_{ref} is known and constant. The ac voltage drop on the device and R_{ref} are measured by lock-ins and dc voltage drop is measured by 1:1 voltage amplifier. The output of both are given to the nano voltmeter which then passes the signal to the computer.

Figure 5.3 shows data from 3 different Josephson junctions having lengths 150 nm, 200 nm and 250 nm. Both 150 nm and 200 nm long junctions have the same thickness for the Ti layer (sputtered at 100 W for 65 s) while the 250 nm long junction has slightly thicker

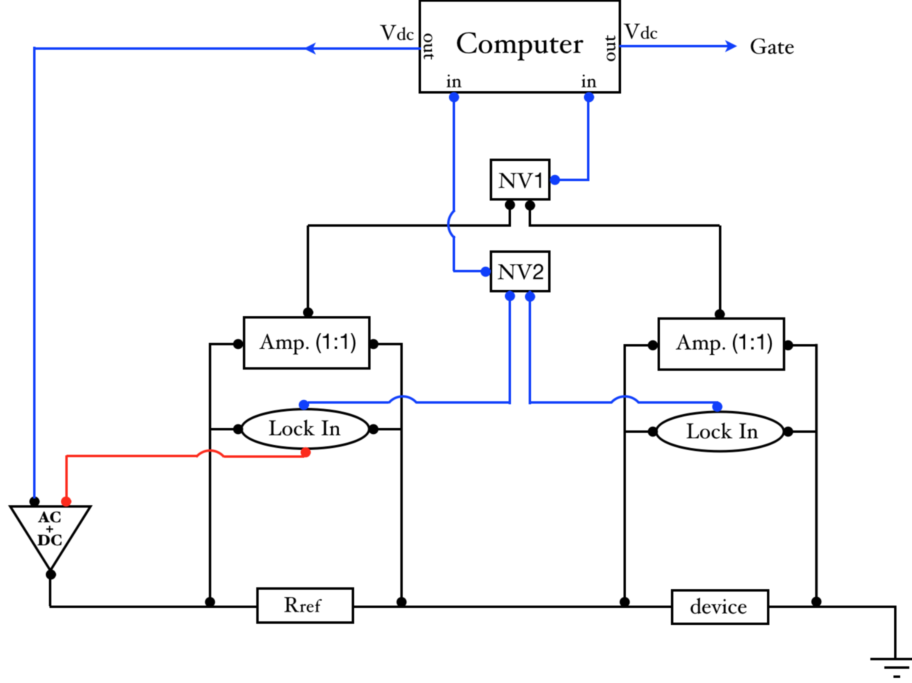

Figure 5.2: Simplified diagram of the differential resistance measurement setup. The ac+dc adapter superimposes the small ac signal from the lock in to the dc bias voltage from the computer to bias the device (Jospehson junction). The lock-in amplifiers measure the ac voltage drop on the reference resistor (R_{ref}) and the device while 1:1 voltage amplifiers measure the dc voltage drop. The output of both are then fed to the nano voltmeter which then sends it to the computer. The blue lines represents dc-only lines and red line represents ac-only lines.

Ti layer (100 W, 75 seconds). The graphs in Figure 5.3 show the gate-sweep, differential conductance and the I-V characteristics of the junctions.

5.2.1 150 nm long junction

The results of the measurements performed on this junction is shown as brown curves in Figure 5.3. Figure 5.3 (a) shows the gate sweep of the junction and the Dirac point can be seen at ∼-10 V, meaning the graphene is electron doped. The slight 'n' doping of the graphene can be due to the residues or contaminants from the fabrication processes. Also what can be seen is the asymmetry between the hole and electron regime. Figure 5.3 (b) shows the differential conductance of the junction at high gate voltage (∼42 V). As explained in chapter 5, multiple Andreev reflections (MAR) happen whenever the dc bias voltage equals $2\Delta/n$ and the conductance peak for n=1 happens when applied voltage equals 2Δ, provided the junction has good transparency. Three conductance peaks can be seen in Figure 5.3 (b) at 2Δ, Δ and at $\Delta/2$ which gives a superconducting gap $2\Delta \approx 800$

eV. The measured Δ of the Nb contacts are four times less than the gap (Δ) of the bulk Nb superconductor. Strongly reduced gap of Ti/Nb superconductor is also reported on carbon nanotubes [82,83]. E Sheer *et al.* [84] also shows a reduced superconducting gap in Al/Au/Al point contacts where the superconductivity is proximity induced compared to a pure Al device having the same device design. One reason for reduced gap in our devices can be that the transport happens between the proximity induced superconducting density of states in Ti layer or in graphene under the superconducting contacts rather than the Nb contacts and thus have different characteristics (like bandgap). Another reason could be the contaminants in the Nb contacts during the sputtering process. In the dirty limit, the superconducting coherence length is given by $L_\phi = \sqrt{(\hbar D/\Delta)}$. The diffusion constant D in graphene is given by $D = \sigma/e^2\rho(E)$, where $\rho(E)$ is the density of states in graphene, e the electron charge and σ is the conductivity given by $L/(WR_N)$. Here L, W and R_N represent length, width and normal state resistance of the junction respectively. For the 150 nm junction, the width of the graphene flake is 2.8 μm and the diffusion constant is calculated to be 0.015 m^2/s. This gives a superconducting coherence length of 135 nm. It is important to mention that this value is the lower limit of the coherence length since contact resistance is not avoided in the calculation of diffusion constant. Also it is not clear what is the effective length of the junction. For the calculation presented here the length of the junction is taken as the distance between the edges of Nb contact (150 nm) rather than the center to center of the contact (350 nm).

Figure 5.3 (c) shows the I-V characteristics of the junction (brown curve) and how the excess current (I_{ex}) is calculated from the I-V curve. This excess current is caused by the Andreev reflection process happening between the superconducting contacts. According to BTK formalism [85], the ratio of $I_{ex}R_N$ to Δ/e is called the interface barrier strength Z. The transparency of the junction is given by $T = 1/(1+Z^2)$. The normal state resistance (R_N) for the junction is 70 Ω (at V_G ~42 V) which also includes interface resistance between graphene and superconductor. From the figure $I_{ex} \approx 4$ μA and the corresponding T≈67%. But this calculations assume ballistic transport between the superconducting junction but in our case it is diffusive. The elastic mean free path (l_e) of graphene is given by $2D/V_F$ where V_F is the Fermi velocity. Substituting the value of D and $V_F \sim 10^6$ m/s, gives $l_e \approx 30$ nm which is much smaller than the junction length. So even though the value of T can be used to compare different junctions, the value itself cannot be taken as absolute. Figure 5.3 (d) shows the close up of the I-V curve showing a supercurrent through the junction. The voltage drop on the junction near zero bias is not zero but a few microvolts and the switching from normal to superconducting state is rather smooth. These observations have been reported already in graphene based Josephson junctions [81, 86]. The reason for the gradual switching and the small offset voltage is the phase diffusion in underdamped junctions in the presence of strong thermal fluctuations [86, 87]. Such an I-V curve can be analysed by resistively and capacitively shunted junction (RCSJ) model where the weak link is considered as a parallel circuit of the actual junction, a resistor and a capacitor [74].

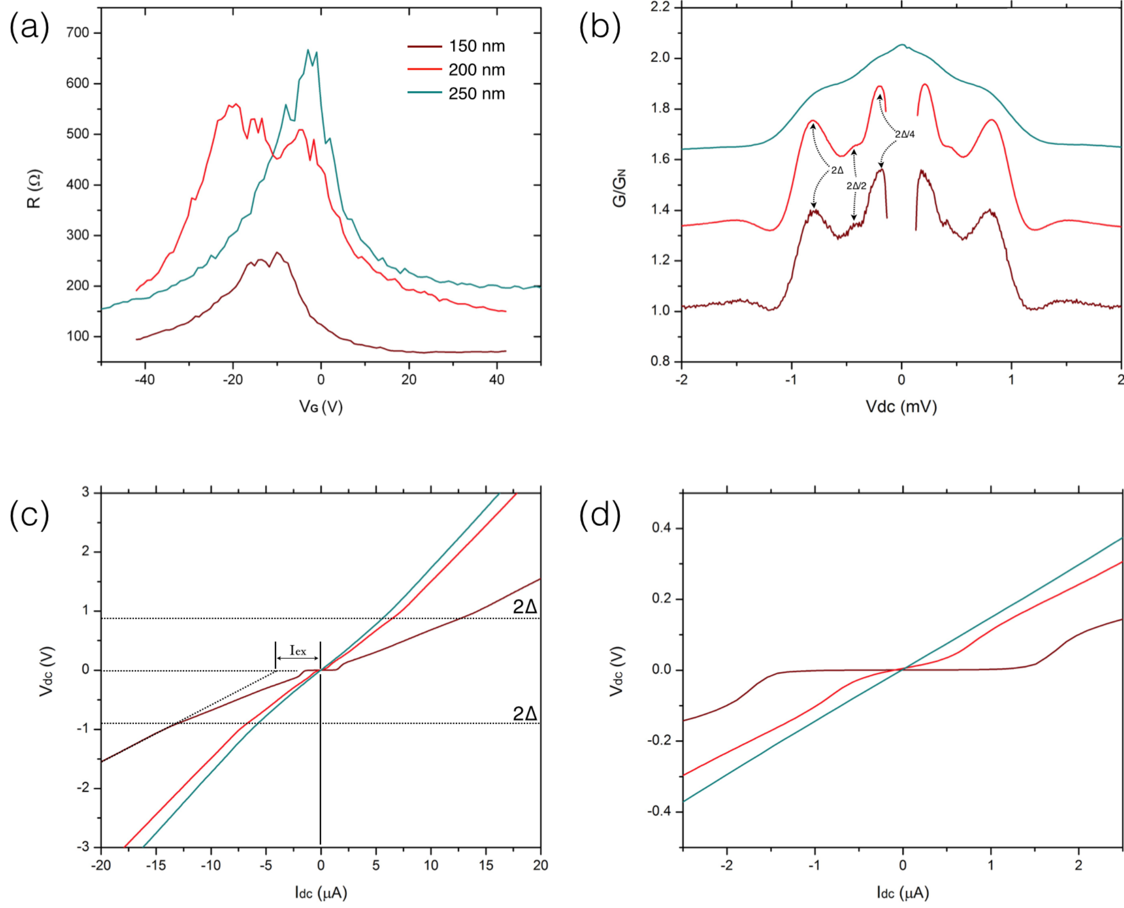

Figure 5.3: Data showing the gate-sweep, conductance spectra and I-V characteristics of the Josephson junctions with lengths 150 nm (brown), 200 nm (red) and 250 nm (blue). (a) Resistance of the junction as a function of back gate voltage (V_G). (b) Differential conductance of the junction as a function of dc bias voltage. The conductance near zero bias for 150 nm and 200 nm junctions shoots up so that the data points near zero are erased. (c) The dc voltage drop on the junction as a function of dc current. I_{ex} for the 150 nm junction (brown curve) is determined by extrapolating the current outside the gap and finding the point where it crosses $V_{dc} = 0$ V line. (d) Closer view of the I-V curve showing supercurrent for the 150 nm long junction.

5.2.2 200 nm junction

Figure 5.3 (a) shows the gate-sweep of the junction and the resistance peak (Dirac point) can be seen at ∼20 V, showing that there is less doping compared to the last junction. The red curve in Figure 5.3 (b) shows the differential conductance of the junction from which the Δ can be deduced to be 410 μV which is quite similar to the 150 nm junction. Also similar to the previous junction is the sub-gap conductance peaks visible at 2Δ, $2\Delta/2$ and $2\Delta/4$. The graphene flake between the contacts are 1.2 μm wide and the diffusion

constant D is calculated to be 0.023 m^2/s, implying that the junction is "cleaner" than the 150 nm junction. The superconducting coherence length for the corresponding diffusion constant is 190 nm. Again this is the lower limit of the value due to the same reasons stated above. The excess current for the junction is ≈3.1 μA which gives a transparency of 43%. The elastic mean free path for the junction is 45 nm which is 50% higher than the 150 nm junction. So it can be said that the increased coherence length is not due to an increased transparency of the junction but due to a much cleaner graphene channel. The junction is part of the F/S device "08.08_S1" and details of the measurement data on this device are given later.

5.2.3 250 nm junction

The 250 nm junction has one main difference from the other two junctions. The Ti layer in this junction is slightly thicker than the other junction. The Ti layer in 250 nm junction is expected to be 15% thicker since the sputtering of Ti was done for 75 seconds (at 100 W) compared to 65 seconds in other junctions. The graphene flake is 1.5 μm wide and the Dirac point is at ∼-5 V. The peaks in the conductance spectra shown in Figure 5.3 is vague and is probably due to a comparatively inferior interface quality. Taking the first maxima in the conductance as 2Δ yields a gap $\Delta \approx 315$ μV which is smaller than other junctions. The diffusion constant is calculate to be 0.01 m^2/s and the coherence length is approximately 140 nm. I_{ex} calculated from the I-V curve is ∼3.4 μA and the transparency is only 17%.

All junctions reported here have superconducting coherence length $L_\phi \gtrsim 140$ nm, which is an important information when analysing data from F/S or F/S/F junction. But at the same time it is also important to mention that the calculation of the L_ϕ ($L_\phi = \sqrt{\hbar D/\Delta}$) does not take in to consideration the quality of the interface. Both 200 nm and 150 nm long junctions show MAR even though the junctions are measured at 1.5 K in a normal He^4 cryostat which shows the quality of the junction. The visible MAR reflections are also consistent with the fact that both junction have a higher transparency (43% and 67%) compared to the 250 nm junction (17%). As said before the values of transparency are only good for comparison since the calculation assumes ballistic transport in the junction and the calculation of elastic mean free paths show this is not the case in our devices. Also, it is interesting to see supercurrent at 1.5 K in 150 nm long junction even though no modelling (RCSJ) has been done to deduce the critical current.

5.3 Device 08.08_S1

The device 08.08_S1 has the basic design shown in Figure 5.2. The distance between S-S, F-F and F-S contacts are 200 nm, 250 nm and 100 nm respectively. The Josephson junction formed at the end of the device is discussed in section 5.2.2. The normal state resistance of the Josephson junction at high gate voltage is only ∼150 Ω which shows a

low contact resistance and high transparency. The conductance spectra of the Josephson junction for different gate voltages is shown in Figure 5.4. Also shown is the conductance curves for different temperatures. As seen in the figure the conductance peaks which are the evidence for MAR is more or less the same at all gate voltages. The position of the peaks gives a gap $\Delta \approx$410 μeV. The width of the gap reduces with the increase in temperature and disappears completely at $\sim$7.3 K. It is important to mention that the temperatures mentioned in the graphs are not exact but an approximation since the temperature sensor used in the measurement was not fully calibrated. From the graph it is clear that the width of the gap seems to saturate at 1.5 K so further increase in gap is not expected at lower temperature which is consistent with the equation 4.6. In fact similar junctions measured in our group at the base temperature of a dilution refrigerator also shows almost same gap width. The coherence length calculated from the diffusion constant and the measured Δ is 190 nm assuming the length of the junction is 200 nm (edge to edge of the contact). If the length is taken as center to center of the superconducting contacts the coherence length increases to 265 nm. But the calculation does not take in to consider interface scattering and it is valid for diffusive junctions where the length of the junction $L > l_e$ but not necessarily when $L > L_\phi$. Recently J.C. Cuevas *et al.* [88] have reported their work where they model the I-V characteristics of diffusive S/N/S junction on the basis of L/L_ϕ ratio. Comparing the value of $eI_{ex}/G_N\Delta$ for the device 08.08_S1 to their calculation gives $L_\phi \approx$ 110 nm if edge to edge distance is taken (200 nm) and 220 nm if center to center (of the contact) distance is taken (400 nm). The calculated L_ϕ values are in accordance with the device design where the distance between the ferromagnetic and superconducting contacts is 100 nm.

As explained earlier, it is also important to show independently that the ferromagnetic contacts are capable of injecting/detecting spin polarised current. The four ferromagnetic contacts F1, F2, F3 and F4 have contact resistances $\sim$7 kΩ, $\sim$2.5 kΩ, $\sim$10 kΩ and $\sim$13 kΩ respectively at 1.5 K. Figure 5.5 (left) shows the results of non-local measurements which shows all the ferromagnetic contacts are spin sensitive. The graph on the left shows the results of two nonlocal measurements involving contact pairs F1, F2 and F3, F4 at 1.5 K. The switching of the contacts can be seen at 14 mT, 22 mT, 33 mT and 44 mT which is in accordance with their width 600 nm, 500 nm, 300 nm and 200 nm. The contacts F2 and F3 which have comparatively smaller widths (200nm and 300 nm) are deliberately placed adjacent to S2 so that they have a shorter center to center (of contact) distance between them which might be important when nonlocal measurements involving F2, S2 and F3 are performed. But even though the difference in their width is only 100 nm, since the switching field is proportional to $1/W$, there is enough difference in their switching fields ($\sim$10 mT) to independently control their magnetic orientation. The graph on the right of Figure 5.5 shows the change in ΔR_{NL} from the contacts F1 and F2 with respect to the gate voltage. According to Figure 3.10 and equation 3.9, the graph shows a perfect tunnel barrier behaviour for the contact pair F1 and F2. Assuming the previously reported values of spin relaxation times in graphene for the device, the polarisation of

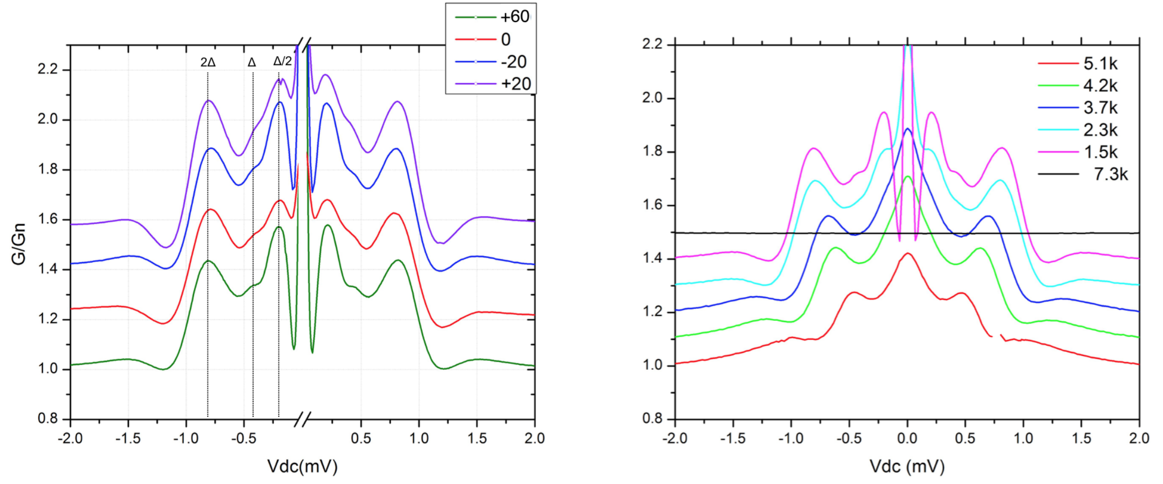

Figure 5.4: (left) Conductance spectra of the junction S3/G/S4 for different gate voltages $V_G - V_D$ where V_D represents the position of the Dirac point. A break is introduced in the x axis since the conductance shoots up near zero bias. (right) Conductance curves at different temperatures. The sub-gap conductance peaks becomes unclear with the increase in temperature. Note that the gap closes just above 7.3 K.

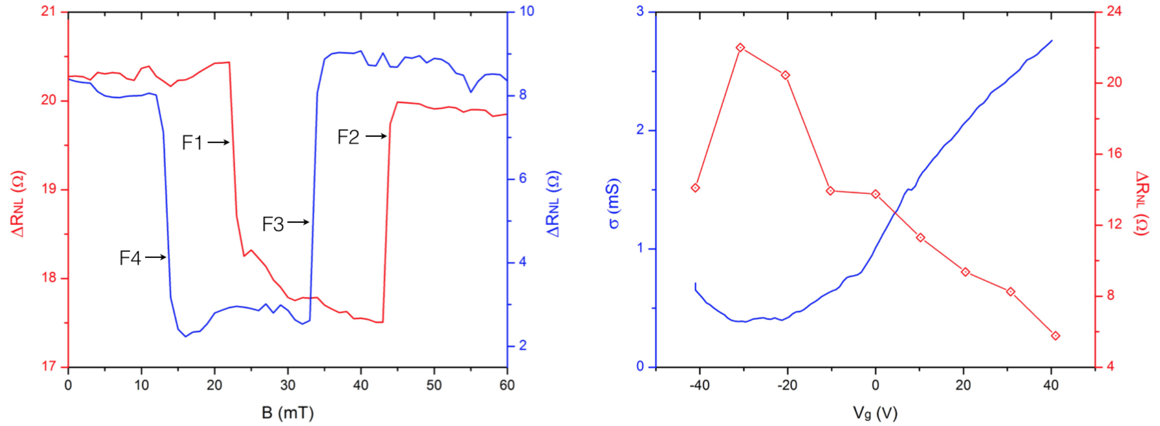

Figure 5.5: (left) Results of nonlocal measurements conducted on ferromagnetic contacts F1, F2 and F3, F4. For the red curve, current is injected from F1 to S1 and the corresponding nonlocal voltage is measured between F2 and S2. In the same way, for the blue curve, current is injected from F3 to S2 and the nonlocal voltage is measured between F3 and S3. (right) Graph shows the change in ΔR_{NL} (red) as a function of gate voltage (V_G). Also shown is the conductivity (blue curve) of graphene flake as function of V_G. Note that the maxima in ΔR_{NL} happens around the minima of conductivity of graphene.

the contacts is 10%-12%. This value is a a lower limit since to deduce the spin relaxation length from a nonlocal spin valve device, the length of the channel (graphene) between the contacts need to be much higher then the contact widths, ideally. But in the case of device 08.08_S1, the distance between the ferromagnetic contacts are only 250 nm which is lower than the widths of 3 out of four ferromagnetic contacts.

After independently proving the quality of ferromagnetic and superconducting contacts, the obvious measurement to do is to perform a differential resistance measurement on a ferromagnet/graphene/superconductor (F/G/S) junction. Figure 5.4 shows the differential resistance (R) versus applied dc bias (V_{dc}) between contact F2 and S2. The measurement is carried out by applying a small ac voltage of amplitude 30 μV-50 μV which is superimposed on the dc bias which is then slowly swept. Prior to the measurement, the ferromagnetic contact is saturated at ±400 mT and then the field is swept back to zero. The aim of the measurement is to find out what happens when spin polarised electrons are injected to a superconductor. But it is important to know that in this measurement, spin polarised electrons from the ferromagnet are not directly injected to the superconductor. Instead, they are injected to the graphene under the ferromagnet from where they are directed towards the superconductor by the applied potential. The differential resistance curves (Figure5.4) have many peaks and dips and are asymmetric with respect to x axis. Both curves for spin up and spin down injected current overlap for the most of the part with slight differences near zero bias voltage. This is consistent with the fact that in the absence of any reference direction superconductor does not see any difference between spin up and spin down electrons. To make any analysis of the data it is important to know where the superconducting gap starts to open and which are the sub-gap transport structures. But the fact that most of the voltage is dropped at the interface of the ferromagnet and graphene, makes it difficult to predict at what bias voltage the sub-gap transport starts to take place. Due to the presence of tunnel barrier between graphene and ferromagnet, a linear estimation of the voltage drop between graphene and superconductor is not possible since the voltage drop across the ferromagnet/graphene interface itself is a function of bias voltage. The oscillations and the asymmetry seen on these curves are also seen on the junction formed by contact F3 and S2. Since contact F3 has a higher contact resistance, differential resistance of both F2/G/S2 and S2/G/F3 junctions were plotted as a function of bias current to see any similarities between the curves but no resemblances were found between the curves. Similar behaviour is also seen in other devices where the resistance curves changed the shape over time and the strength of saturating magnetic field. To understand the origin of the oscillations, differential resistance of the junction F2/G/F3 is measured as a function of bias voltage and the result can be seen in Figure 5.6 (right). In principle the junction should show the behaviour of a tunnel barrier contact with the resistance consistently increasing with the decrease in bias voltage. But instead the graph shows oscillations similar to F/G/S junction with many oscillations in the resistance curve. This suggests that the curves in Figure 5.6 (left) shows mostly the behaviour of the ferromagnet and not the interplay between ferromag-

net and superconductor. It is also possible that any contribution of superconductor is buried under the large resistance of ferromagnet/graphene interface. But the oscillations in the differential resistance curves of F/G/F is also quite unusual. To understand where the oscillations are coming from, a device with ferromagnetic contacts alone needs to be fabricated and the same measurements has to be repeated to see if the resistance curves are reproducible in the absence of neighbouring superconductors.

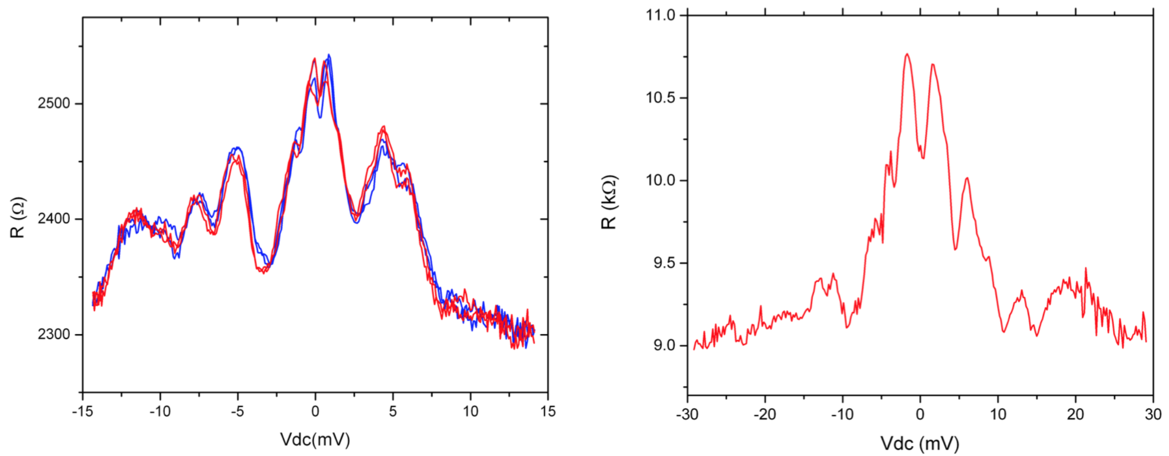

Figure 5.6: (left) Graph showing the ac differential resistance of F2/G/S2 junction as a function of dc bias voltage. Blue curve shows the data when F2 is magnetised in the "up" direction and red for the opposite direction. (right) Differential resistance for the junction F2/G/F3.

Another important measurement which can shed some light in to the behaviour of the F/S junction is the pseudo nonlocal measurement where an ac+dc spin current is injected in to the superconductor using the ferromagnet and the resulting ac nonlocal voltage is measured using a second ferromagnet. The device is designed to perform this measurement and at the center of the device there is an F/G/S/G/F junction using which a spin polarised current can be injected from the left ferromagnet to the superconductor and the corresponding nonlocal voltage can be measured using the ferromagnet on the right. This basic design of the measurement in principle can detect crossed Andreev reflection [71,72], elastic cotunneling and also spin imbalance [68,73]. In our measurement the current is injected from contact F2 (200 nm) to S2 (200 nm) and the nonlocal voltage is measured between S2 and F3 (300 nm). An ac current of amplitude 0.1-1.2 μA is superimposed on to a dc signal and the dc voltage is swept and the change in nonlocal voltage is measured. The resistance of the reference resistor used for the measurement is much higher than the device resistance so that the changes in device resistance does not effect the bias current. All measurements are done in zero magnetic field but prior to the measurement, the magnetic orientation of the ferromagnetic contacts are adjusted in the desired direction by the help of magnetic field.

Figure 5.7 (left) shows the nonlocal voltage measured as a function of dc bias voltage for different values of current. Prior to the measurements, magnetic field is swept to +400 mT and then back to zero so that that both ferromagnetic contacts are magnetised in the "up" direction. All curves in the figure have two basic characters. One is that they all have a maxima and minima occurring at same dc bias voltage having opposite polarities. And the other is observation of zero ac nonlocal voltage at zero dc bias voltage. This characteristic behaviour is similar to the results of Hubler *et al.* [68] and Quay *et al.* [73] where they report these characteristic curves as one of the main evidence for spin imbalance in quasiparticle density of states in superconductor. The concept of spin imbalance in a superconductor is explained in section 4.5.2. In their measurement a current is injected from a ferromagnet/normal contact to the superconductor and the spin imbalance is created by Zeeman splitting. The spin diffusion in the superconductor is then detected by a different ferromagnet which is also in contact with the superconductor. So there are two basic difference between the data shown here and the reported by the same. One is that they are measuring the spin diffusion happening in the superconductor and in our case, if we assume it is the same phenomenon we are observing, then the spin imbalance created in the quasiparticle density of states of the superconductor is diffusing to the graphene which is what measured by the ferromagnet placed closer to the superconductor. Secondly, even though Ref. [73] states that the spin imbalance can be created either by injecting spin current to the superconductor or by Zeeman splitting, both reports mentioned before uses an external magnetic field to create the spin imbalance even though in principle, injecting spin current alone should be able to create the phenomenon. In our case, similar data is measured in the absence of any external field, which suggest that it is the spin polarised electrons injected to the superconductor which creates the imbalance in the quasiparticle density of states.

Data in the Figure 5.7 show that upon increasing the ac current amplitude, the curve is affected in two different ways. One is that the maxima/minima shifts away from zero and the other is that the amplitude of the peaks increases. The increase in amplitude can be direct consequence of a higher number of spin polarised electrons injected to the superconductor and hence a higher number of diffusing spins in graphene. This is quite similar to the effect of an increased current in a nonlocal spin valve device. In such devices both the background voltage and ΔV_{NL} scales with the amplitude of the bias current. But the shift in the position of the peaks can happen only if the spin chemical potentials also shift. This can happen due to an increased polarisation of the injecting ferromagnet which creates a higher asymmetry in the quasiparticle spin density of states or in the presence of an external magnetic field which shifts the density of states by $\pm\mu H$. But both these reasons do not apply in our case. The reason for the shift in the features can be the change in the ac bias signal itself. In principle in an ac+dc measurement the amplitude of the ac bias voltage needs to be much smaller compared to the dc bias voltages so that the ac signal itself does not effect the results. But in this case the lowest ac current of amplitude 0.12 μA corresponds an ac rms voltage of 300 mV and the highest current of

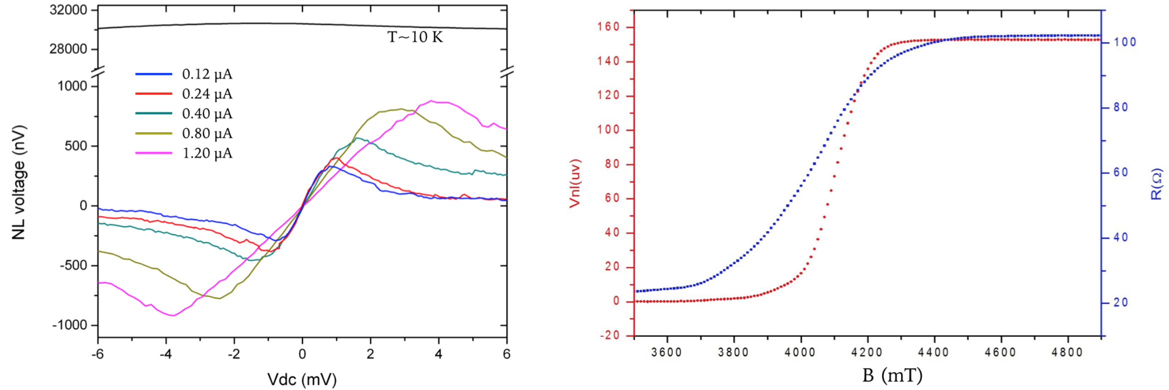

Figure 5.7: (left) Ac nonlocal voltage as a function of dc bias voltage for different ac bias excitations. (right) Graph showng the critical field of the superconducting contacts along with the change in ac nonlocal voltage at zero bias for the same.

1.2 μA is equivalent to 3 mV. So the ac voltage is comparable to the dc bias voltage which might be the reason for the shift in maxima/minima. Also it can be seen that the features shift more for higher ac currents than for lower ac currents which also points to the higher ac bias voltage as the reason for the shifts. To make sure the data are superconductor related the measurement is also carried out at ∼10 K where the superconductor is in normal state. As shown in the graph, the maxima and minima, which represent the spin up and spin down quasiparticle chemical potentials in the superconductor, vanish at this temperature and also there is a big offset voltage of amplitude ∼30 μV near zero bias.

As mentioned earlier the second important feature is the precise zero ac nonlocal voltage measured at zero bias. To check if this is superconductor related, a measurement is carried out as follows. First the two terminal resistance of the superconducting contact (stripe) is measured as function of in-plane magnetic field to find out the critical field at which the superconductor becomes normal. The results of this measurements are shown in Figure 5.7 (right) where the change in resistance of the superconductor from 26 Ω to ∼100 Ω can be seen around 4 T. Next the nonlocal ac voltage is measured at zero bias as a function of external in-plane magnetic field. The data shows a change in nonlocal voltage from zero to ∼150 μV at around the same field values of the critical field of the superconductor. So this measurement also proves that the phenomenon is superconductor related and the similarity of the features with already reported data suggests that phenomenon being observed is spin imbalance in the quasiparticle density of the superconductor. Also carried out is a nonlocal spin valve measurement, where spin polarised current is injected from F2 to F1 and the nonlocal voltage is measured between F3 and F4. Upon sweeping the magnetic field after saturating the contacts, no clear switching events where observed even though the distance between the injecting and detecting pairs where only 400 nm.

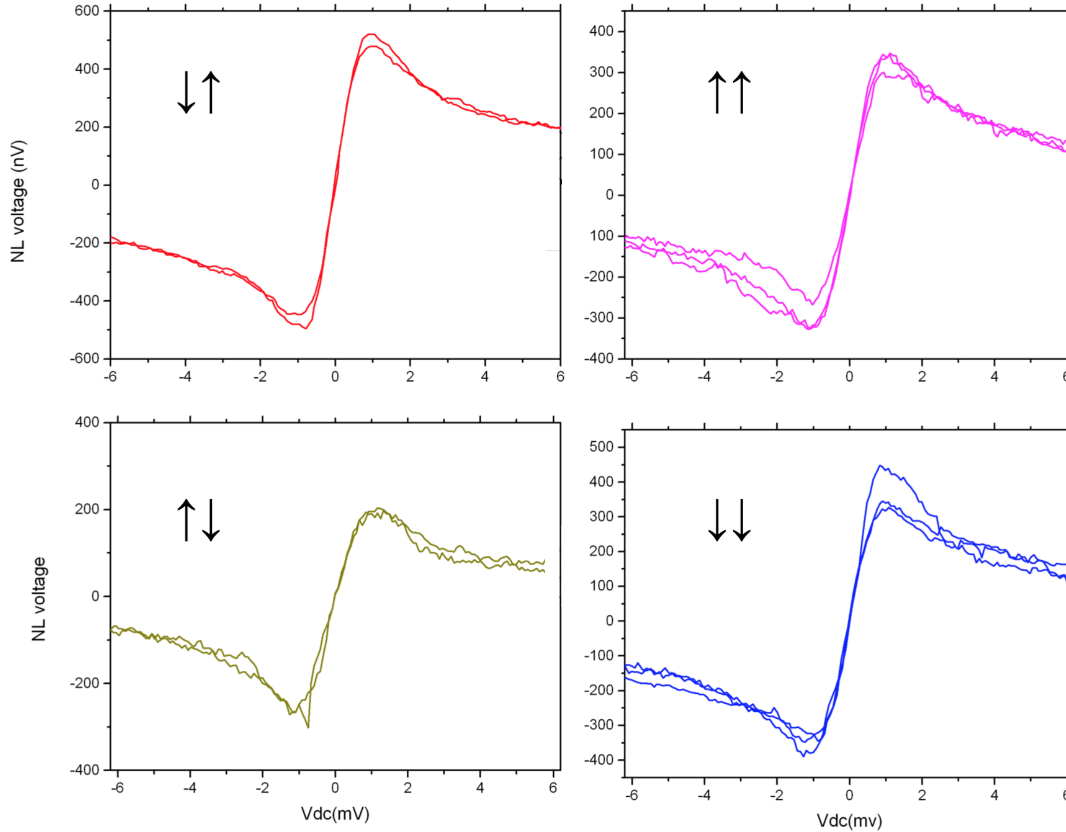

Figure 5.8: Graph showing nonlocal ac voltage as a function of dc bias voltage for different magnetic orientation of the contacts. Measurements are repeated atleast two times and are shown in same colours.

The measurement is carried out for both normal and superconducting state of the contact S2 and the results were similar (not shown). This proves that the spin imbalance created under the contact F2 does not reach contact F3 due to the spin relaxation created by the transparent contact S2 and transparent contacts are known to induce heavy spin relaxation [35]. So again the nonlocal voltage detected by F3 is not originating from F2 and suggests that the most possible cause is the diffusing spins from the superconductor.

Since the detecting contact is measuring spin chemical potential, reversing the magnetisation direction of either the injecting ferromagnet F2 or detecting ferromagnet F3, should switch the position of maxima and minima observed in the measurement. Also the features and their positions should be the same if both F2 and F3 are magnetised in the same direction. But strangely, as shown in Figure 5.8 no reversal of the positions of the features were observed for the anti-parallel configuration of the ferromagnetic contacts even though the data is consistent with the expected behaviour for parallel configurations. The magnetisation orientation of the ferromagnetic contacts are done either by saturating

the contacts at a high magnetic field or by sweeping the magnetic field up to their coercive fields, observing the switching, and then slowly ramping down the field to zero.

5.4 Conclusion and outlook

In conclusion, by developing a fabrication recipe, both ferromagnetic and superconducting contacts are incorporated in graphene to form F/G/S and F/G/S/G/F junctions. Independent measurements show that both ferromagnetic and superconducting contacts are behaving in their expected characteristic manner. Even though the measurements are done in a normal He^4 cryostat with no additional filters, Josephson supercurrent is observed in one of the device. The device 08.08_S1 shows MAR corresponding to n=1,2 and 4 which shows the good interface transparency of the superconducting contacts. Nonlocal spin valve measurements show that all ferromagnetic contacts are spin sensitive and contacts F1 and F2 shows perfect tunnel barrier behaviour in the ΔR_{NL} versus V_G graph. But the conductance spectra of both F/G/S and F/G/F junctions contain unusual oscillations which need to be investigated further to make predictions from the measured data. The three terminal nonlocal measurements performed on the junction F2/G/S2/G/F3 indicate the existence of spin imbalance in the superconducting quasiparticle density of states. The two peak structure observed in our device has been reported in F/I/S/I/F metal junctions with the help of Zeeman splitting even though theoretically external magnetic field is not necessary to observe the phenomenon. In our device the spin imbalance is probably created by the injection of spin polarised electrons into the superconductor. The amplitude of the signal also seems to increase upon increasing the ac bias current. But reversing the magnetisation direction of one of the ferromagnetic contact had no significant effect on the observed curve which is not what is expected theoretically. So more similar devices have to be made and characterised preferably in a dilution refrigerator to conclusively prove the phenomenon. An important measurement to do in such a situation would be to probe the spin imbalance signal using both the ferromagnet (that is inject the current using F2 and detect the voltage drop using both F3 and F4). Such a measurement would allow to deduce the spin relaxation length of the diffusing quasiparticles by assuming that the spin chemical potentials in graphene diffuse exponentially.

Chapter 6

Conclusion and Outlook

This thesis reports a successful fabrication and characterisation of ferromagnetic/superconductor junction (F/S) on graphene. The first challenge in fabricating F/S devices was to develop a fabrication recipe to contact graphene with ferromagnetic contacts. Chapter 2 discusses the two fabrication recipes used to contact graphene with ferromagnetic contacts. The main challenge in using ferromagnets for spin injection to graphene is in growing thin, homogeneous tunnel barrier. The first fabrication recipe consisted of ALD grown Al_2O_3 with out any seed layer to grow thin tunnel barrier. Even though no insulating layer can be grown on pristine graphene surface, the resist residues and other contaminants from the prior fabrication process works as a seed layer to grow the insulating layer. Although many successful devices were made using this recipe, the oxide layers grown without any seed layer were inconsistent and non-uniform which resulted in low yield for successful devices. The second fabrication recipe which uses ALD grown Al_2O_3 with the help of Ti seed layer is more consistent in terms of device performance and has a better yield over the old recipe ($\sim$50 %). Results of measurements done on many devices are shown in chapter 2 and one of the devices made using the new fabrication recipe shows perfect tunnel barrier behaviour (device 08.08_S1). Even then there is room for further improving the fabrication recipe. One suggestion this thesis put forward is to use sputtering over e-beam evaporation for depositing thin Ti seed layer and transferring the samples to ALD system without breaking the vacuum. Also the roughness of the grown layers depends on the thickness of Ti layer. Hence, a combination of thicker Ti seed layer with a suitable ALD cycles in principle should give a more homogeneous insulating layer.

After developing the recipe to contact graphene with ferromagnet, the recipe is further developed to incorporate superconducting contacts to the device to produce ferromagnet/superconductor junctions. The devices are fashioned in a way that both ferromagnetic and superconducting contacts can be independently characterised so that there is a better understanding when analysing the results of the measurements involving both ferromagnetic and superconducting contacts. The data presented from the device 08.08_S1 show expected characteristic behaviour of ferromagnetic and superconducting contacts

with ferromagnetic contacts showing 10-12 % efficiency in injecting/detecting spin polarised electrons. The deduced superconducting coherence length (L_{ϕ}) is higher than the distance between the ferromagnetic and superconducting contacts (100 nm), which is an important condition to observe the interplay of both contacts. Measurements done on F/G/S/G/F suggests that by injecting spin polarised current into the superconductor, a spin imbalance is created in the quasiparticle density of states of the superconductor which then diffuses through the graphene channel. The observed characteristic curves are similar to the ones which are already reported on metallic ferromagnet/superconductor junctions where the spin imbalance is created using Zeeman splitting. Further measurements also show that the curves loose their characteristic shapes when the temperature is increased above the critical temperature (Tc) or when the external magnetic field is higher then the critical field (Hc) of the superconducting contact. But to prove conclusively and doubtlessly the existence of spin imbalance in ferromagnet/superconductor junctions on graphene, more devices have to be made and characterised preferably in a dilution refrigerator.

Appendix A

Fabrication processes

A.1 Preparation of substrates

- Cut the SiO_2/Si wafer to 1cm × 1cm pieces without scratching the SiO_2 surface
- Spin coat ARU-4060S1 at 6000 rpm and bake the substrates at 100 °C for 2 minutes
- Expose the design of the coordinate system using mask aligner (exposure time: 3 s)
- Develop using AR 300-26:H_2O (1:8) for 35 s and gently rinse in clean water
- Deposite 2 nm Ti and 20 nm Au
- Lift-off in preheated Acetone at 50 °C with the help of ultrasonic agitation
- Clean the substrates using plasma and ultrasonic agitation and place them on 180 °C hot plate prior to graphene deposition

A.2 Contacting graphene with ferromagnet

- Find single layer graphene using optical microscope and map them using coordinate marks
- Immediately after, spin coat with PMMA (ARP 672.03, 950K, 3% anisol). 3000 rpm, baking: 180 °C for 2 minutes
- E-beam exposure of the contact design on to PMMA
- Develop using pre-cooled (8°) C_3H_8O : H_2O (3:1) mixture
- Deposite 2 $A°$ Ti in e-beam deposition system at a rate of 0.2 A°/S
- Oxidise in the same setup at 10 mbar for 10 minutes

- Run a "blank" process in ALD to get rid of any chemicals present from previous run
- Run ALD process with sample in at 80 °C, 9 cycles.
  Pulselength: 0.05 s, cover-time: 10 s, purge-time: 100s
- Deposite 50 nm Co in e-beam deposition system at a rate of 0.3-0.4 nm/s and 10 nm Au
- Lift-off in warm acetone (50°C) for 15 minutes
- Cleaning in NEP for 1 hour at 80 °C
- Spin coat same resist with same parameters twice
- E-beam exposure of the leads and bonding pads design on to PMMA
- Develop using pre-cooled (8°) C_3H_8O : H_2O (3:1)
- Deposite 3 nm Ti and 120 nm Au
- Lift-off in warm acetone (50°C)
- Spin coat PMMA (ARP 672.04, 950K, 4.5 % anisol) at 3000 rpm to etch away unwanted graphene/graphite layers
- E-beam exposure and development
- Etching in RIE using process name "Graphene" (process no. 3) for 3-12 seconds depending on the thickness of graphene layers
- Cut the substrate after spin coating PMMA (ARP 672.04, 950K, 4.5 % anisol) and clean them in NEP for 1 hour at 80 °C
- Cut the substrate and glue it in chip carrier using silver glue and place it on hot plate at 180 ° C for 2 minutes
- Bond the device using ultrasonic bonding technique and keep the devices in vacuum until measuring setup is ready

A.3 Fabrication of ferromagnet-superconducting junctions

- Contact graphene with ferromagnet as explained

- After lift-off process in warm acetone (non-preheated), spin coat PMMA (ARP 672.03, 950K, 3% anisol)
- E-beam exposure of the superconducting contact design and successive development
- Deposite Ti, Nb, Al and Ru in the dc sputtering system
  Ti: 100 W, 65 s
  Nb: 400 W, 5×30 s with 10 minute gap between
  Al: 50 W, 119 s
  Ru 100 W, 100 s
- Lift-off process in warm acetone (non-preheated)
- Spin coat PMMA twice (ARP 672.03, 950K, 3% anisol)
- E-beam exposure and development for bonding pads and leads
- Etching of undeveloped resist in RIE. Process name "mini clean" (process no. 70)
- Deposite 3 nm Ti and 120 nm Au in e-beam deposition system
- Perform lift-off and then spin coat PMMA (ARP 672.04, 950K, 4.5 % anisol) for etching away unwanted graphene layers
- After etching, spin coat PMMA (ARP 672.04, 950K, 4.5 % anisol) and cut the substrates appropriately and clean them in NEP (80 °C) for 1 hour.
- Glue the devices in chip carrier and keep them in vacuum until ready for measurements.

Appendix B

Picture gallery

B.1 Ferromagnet-superconductor junctions on graphene

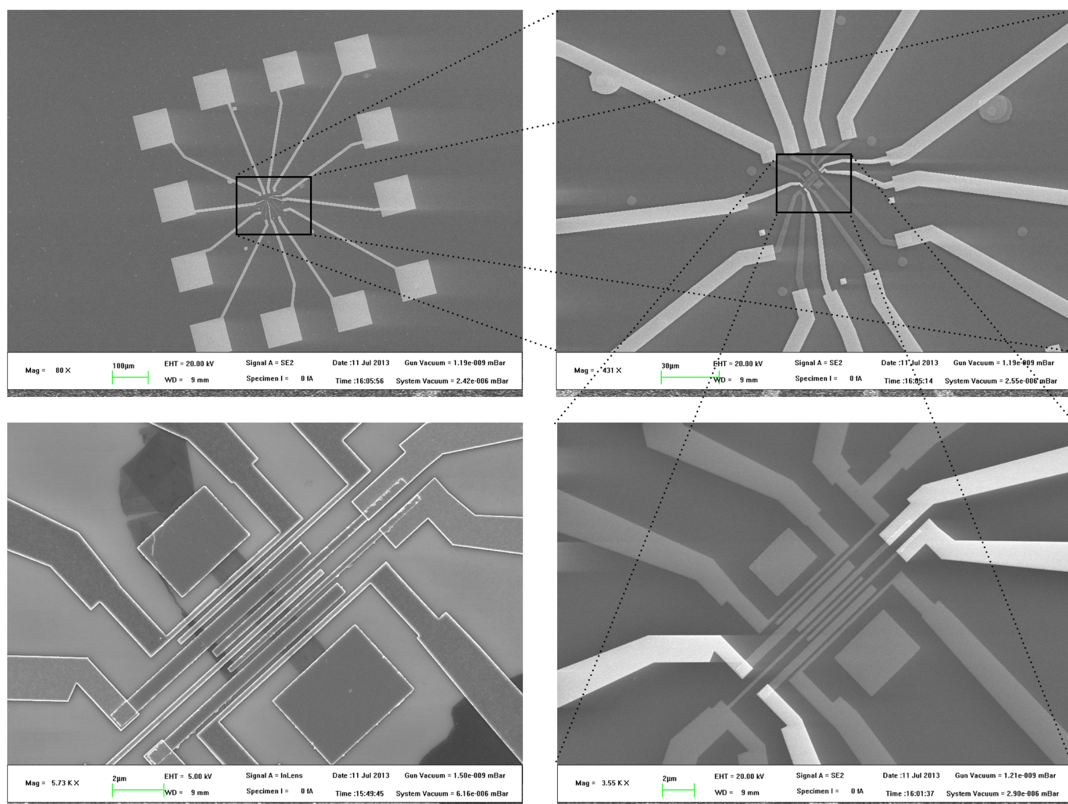

Figure B.1: SEM images of a F/S device with different magnifications.

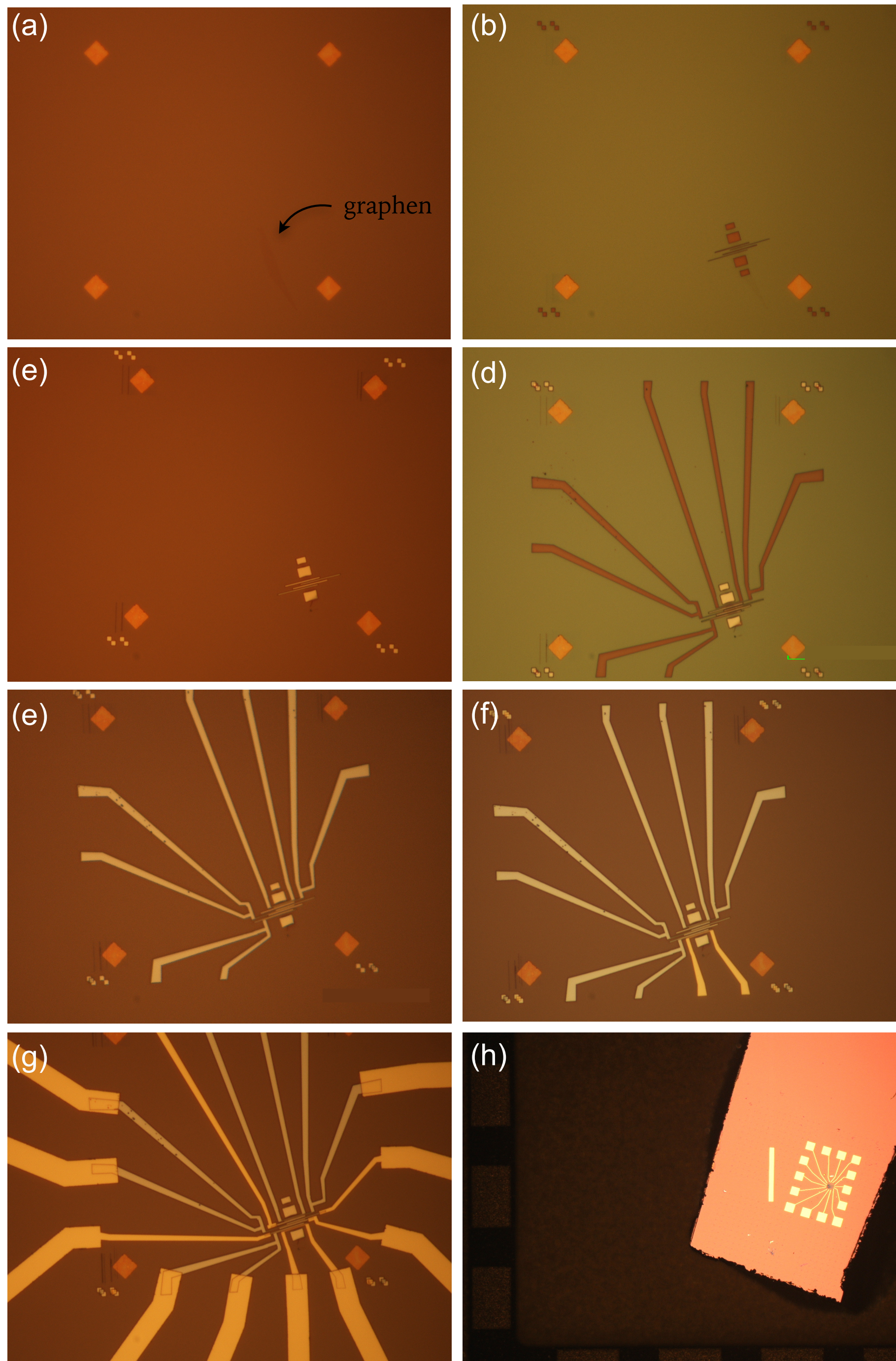

Figure B.2: Opical microscope images of F/S device during different fabrication steps. (a) Graphene deposition. (b) After the development of ferromagnetic contact design. (c) After the deposition of Co and Au. (d) After the e-beam exposure and development of superconducting contacts. (e) After the deposition of Ti, Nb, Al and Ru. (f) After placing nomral (Ti/Au) contacts. (g) After connecting contacts with Ti/Au leads. (h) After glueing the device in chip carier.

B.2 Other devices

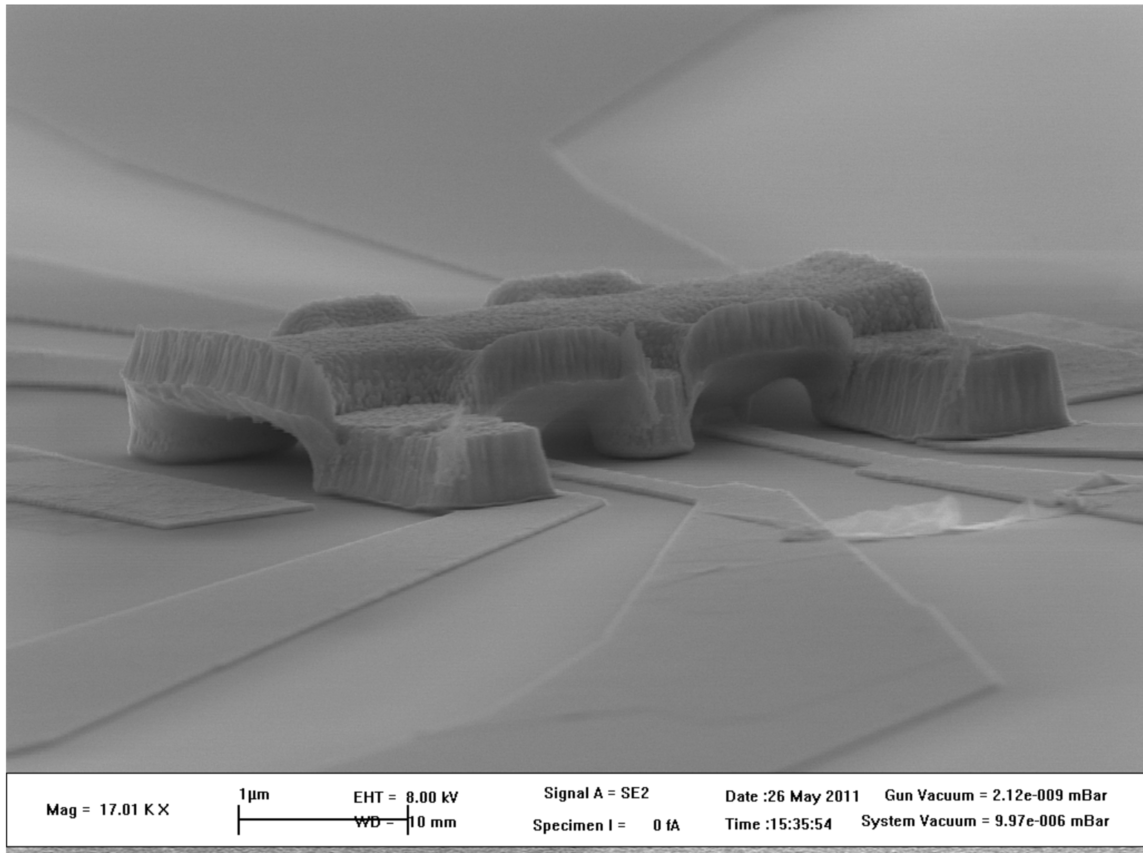

Figure B.3: A graphene hall bar device with air bridge as topgate.

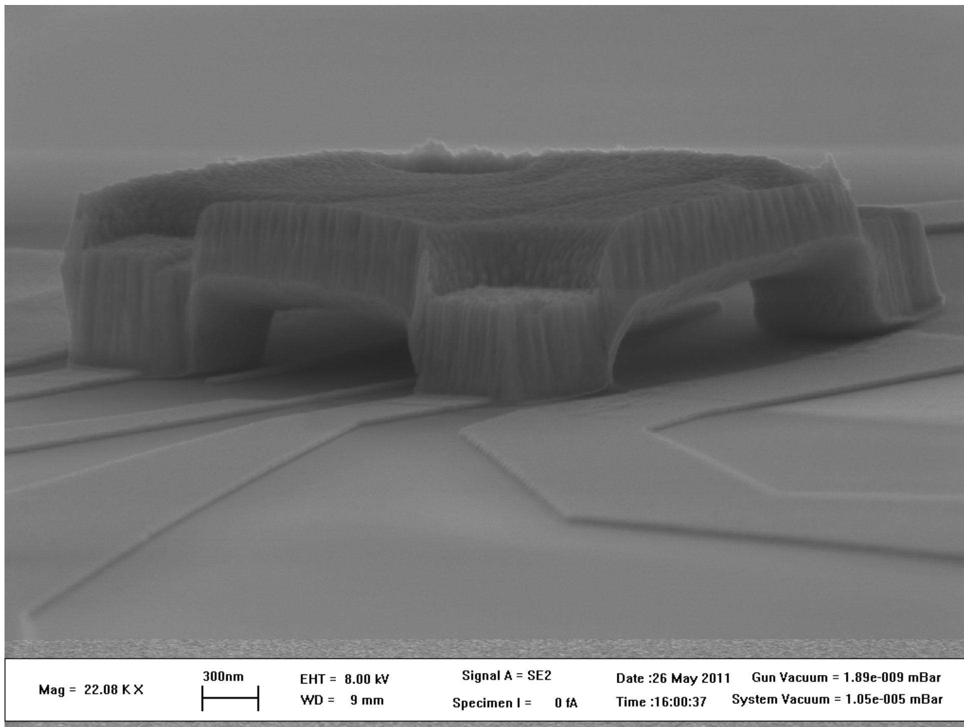

Figure B.4: Graphene device with a different topgate.

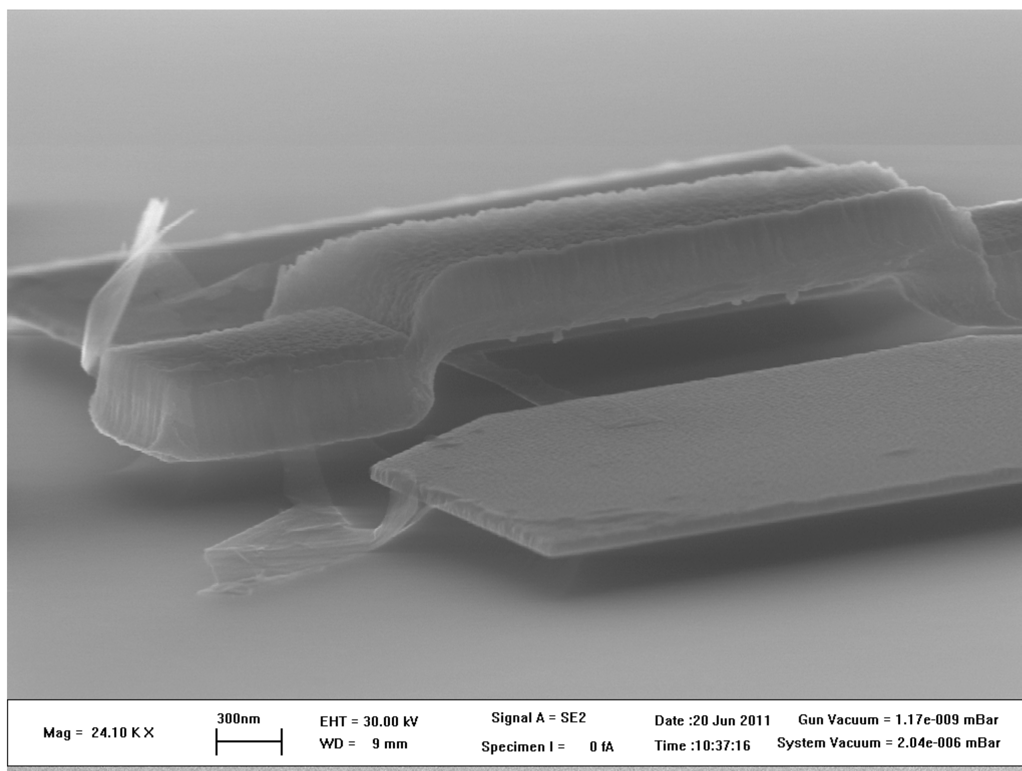

Figure B.5: Suspended graphene ribbon with airbridge as top gate. One of the two graphene ribbons was washed away during the etching. The second one can be seen in the figure.

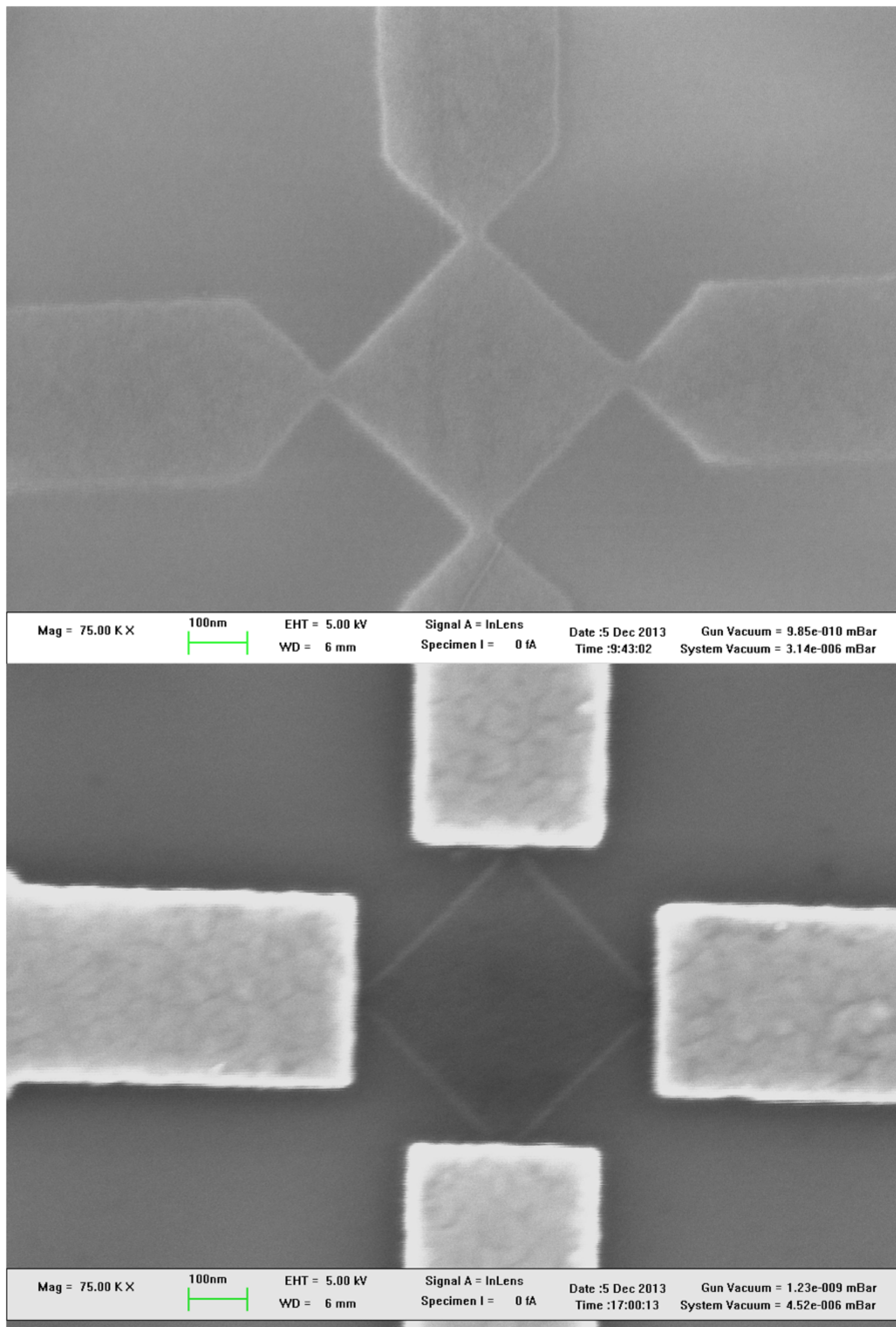

Figure B.6: (top) A diamond shaped graphene device before placing cotacts. The constrictions have widths between 30-50 nm. (bottom) The device after the placement of the Ti/Au contacts. Note that the edges of the contacts are in allignment with the constriction.

Bibliography

[1] A. Aspect, P. Grangier, and G. Roger, “Experimental Realization of Einstein-Podolsky-Rosen-Bohm Gedankenexperiment: A New Violation of Bell’s Inequalities,” *Phys. Rev. Lett.*, vol. 49, pp. 91–94, July 1982.

[2] K. S. Novoselov, A. K. Geim, S. V. Morozov, D. Jiang, Y. Zhang, S. V. Dubonos, I. V. Grigorieva, and A. A. Firsov, “Electric Field Effect in Atomically Thin Carbon Films,” *Science*, vol. 306, pp. 666–669, Oct. 2004.

[3] N. Tombros, C. Jozsa, M. Popinciuc, H. T. Jonkman, and B. J. van Wees, “Electronic spin transport and spin precession in single graphene layers at room temperature,” *Nature*, vol. 448, no. 7153, pp. 571–574, 2007.

[4] G. Schmidt, D. Ferrand, L. Molenkamp, A. Filip, and B. van Wees, “Fundamental obstacle for electrical spin injection from a ferromagnetic metal into a diffusive semiconductor,” *Physical Review B*, vol. 62, pp. R4790–R4793, Aug. 2000.

[5] T. Yamaguchi, S. Masubuchi, K. Iguchi, R. Moriya, and T. Machida, “Tunnel spin injection into graphene using Al2O3 barrier grown by atomic layer deposition on functionalized graphene surface,” *Journal of Magnetism and Magnetic Materials*, vol. 324, pp. 849–852, Mar. 2012.

[6] W. Han, K. M. McCreary, K. Pi, W. H. Wang, Y. Li, H. Wen, J. R. Chen, and R. K. Kawakami, “Spin transport and relaxation in graphene,” *Journal of Magnetism and Magnetic Materials*, vol. 324, pp. 369–381, Feb. 2012.

[7] G. Brassard and a. A. Méthot, “Can quantum-mechanical description of physical reality be considered correct?,” *Foundations of Physics*, vol. 40, no. 4, pp. 463–468, 2010.

[8] J. S. Bell, “On the Einstein-Podolsky-Rosen paradox,” *Physics*, vol. 1, pp. 195–200, 1964.

[9] L. Wang, I. Meric, P. Y. Huang, Q. Gao, Y. Gao, H. Tran, T. Taniguchi, K. Watanabe, L. M. Campos, D. A. Muller, J. Guo, P. Kim, J. Hone, K. L. Shepard, and C. R. Dean, “One-Dimensional Electrical Contact to a Two-Dimensional Material,” *Science*, vol. 342, pp. 614–617, Nov. 2013.

[10] A. A. Balandin, “Thermal properties of graphene and nanostructured carbon materials,” *Nat Mater*, vol. 10, pp. 569–581, Aug. 2011.

[11] C. Lee, X. Wei, J. W. Kysar, and J. Hone, "Measurement of the Elastic Properties and Intrinsic Strength of Monolayer Graphene," *Science*, vol. 321, pp. 385–388, July 2008.

[12] J. S. Bunch, S. S. Verbridge, J. S. Alden, A. M. van der Zande, J. M. Parpia, H. G. Craighead, and P. L. McEuen, "Impermeable Atomic Membranes from Graphene Sheets," *Nano Letters*, vol. 8, pp. 2458–2462, Aug. 2008.

[13] G. A. K. and N. K. S., "The rise of graphene.," *Nat. Mater.*, pp. 183–191, 2007.

[14] a. H. Castro Neto, N. M. R. Peres, K. S. Novoselov, and a. K. Geim, "The electronic properties of graphene," *Reviews of Modern Physics*, vol. 81, pp. 109–162, Jan. 2009.

[15] M. Wilson, "Electrons in atomically thin carbon sheets behave like massless particles," *Physics Today*, vol. 59, no. 1, pp. 21–23, 2006.

[16] S. Bae, H. Kim, Y. Lee, X. Xu, J.-S. Park, Y. Zheng, J. Balakrishnan, T. Lei, H. Ri Kim, Y. I. Song, Y.-J. Kim, K. S. Kim, B. Ozyilmaz, J.-H. Ahn, B. H. Hong, and S. Iijima, "Roll-to-roll production of 30-inch graphene films for transparent electrodes," *Nat Nano*, vol. 5, pp. 574–578, Aug. 2010.

[17] W. Gannett, W. Regan, K. Watanabe, T. Taniguchi, M. F. Crommie, and a. Zettl, "Boron nitride substrates for high mobility chemical vapor deposited graphene," *Applied Physics Letters*, vol. 98, no. 24, pp. 1–4, 2011.

[18] S. B. Lee, J. S. Lee, S. H. Chang, H. K. Yoo, B. S. Kang, B. Kahng, C. J. Kim, and T. W. Noh, "One-Dimensional Electrical Contact to a Two-Dimensional Material," *Science*, no. November, pp. 1–12, 2013.

[19] F. Bonaccorso, Z. Sun, T. Hasan, and a. C. Ferrari, "Graphene Photonics and Optoelectronics," vol. 4, no. August, pp. 611–622, 2010.

[20] P. Blake, E. W. Hill, a. H. Castro Neto, K. S. Novoselov, D. Jiang, R. Yang, T. J. Booth, and a. K. Geim, "Making graphene visible," *Applied Physics Letters*, vol. 91, no. 6, pp. 1–4, 2007.

[21] X. Wang, S. M. Tabakman, and H. Dai, "Atomic Layer Deposition of Metal Oxides on Pristine and Functionalized Graphene," *Journal of the American Chemical Society*, vol. 130, no. 26, pp. 8152–8153, 2008.

[22] S. M. George, "Atomic layer deposition: An overview," *Chemical Reviews*, pp. 111–131, 2010.

[23] J. J. Thomson, "Cathode Rays," *Philosophical Magazine Series 5*, vol. 44, no. 269, pp. 293–316, 1897.

[24] M. N. Baibich, J. M. Broto, A. Fert, F. N. Van Dau, F. Petroff, P. Etienne, G. Creuzet, A. Friederich, and J. Chazelas, "Giant Magnetoresistance of (001)Fe/(001)Cr Magnetic Superlattices," *Phys. Rev. Lett.*, vol. 61, pp. 2472–2475, Nov. 1988.

[25] G. Binasch, P. Grünberg, F. Saurenbach, and W. Zinn, "Enhanced magnetoresistance in layered magnetic structures with antiferromagnetic interlayer exchange," *Phys. Rev. B*, vol. 39, pp. 4828–4830, Mar. 1989.

[26] N. A. Spaldin, *Magnetic materials: fundamentals and applications.* Cambridge University Press, 2010.

[27] W. Thomson, "The Bakerian Lecture: – On the Electro-Dynamic Properties of Metals," *Proceedings of the Royal Society of London*, vol. 8, pp. 50–55, 1856.

[28] C. Chappert, A. Fert, and F. N. Van Dau, "The emergence of spin electronics in data storage," *Nat Mater*, vol. 6, no. 11, pp. 813–823, 2007.

[29] N. F. Mott, "Electrons in transition metals," *Advances in Physics*, vol. 13, no. 51, pp. 325–422, 1964.

[30] W. Y. Lee, S. Gardelis, B.-C. Choi, Y. B. Xu, C. G. Smith, C. H. W. Barnes, D. A. Ritchie, E. H. Linfield, and J. A. C. Bland, "Magnetization reversal and magnetoresistance in a lateral spin-injection device," *Journal of Applied Physics*, vol. 85, no. 9, 1999.

[31] P. R. Hammar, B. R. Bennett, M. J. Yang, and M. Johnson, "Observation of Spin Injection at a Ferromagnet-Semiconductor Interface," *Physical Review Letters*, vol. 83, pp. 203–206, July 1999.

[32] F. G. Monzon, M. Johnson, and M. L. Roukes, "Strong Hall voltage modulation in hybrid ferromagnet/semiconductor microstructures," *Applied Physics Letters*, vol. 71, no. 21, pp. 3087–3089, 1997.

[33] A. Fert and H. Jaffrès, "Conditions for efficient spin injection from a ferromagnetic metal into a semiconductor," *Phys. Rev. B*, vol. 64, p. 184420, Oct. 2001.

[34] D. Huertas-Hernando, F. Guinea, and A. Brataas, "Spin-Orbit-Mediated Spin Relaxation in Graphene," *Phys. Rev. Lett.*, vol. 103, p. 146801, Sept. 2009.

[35] T. Maassen, I. J. Vera-Marun, M. H. D. Guimarães, and B. J. van Wees, "Contact-induced spin relaxation in Hanle spin precession measurements," *Phys. Rev. B*, vol. 86, p. 235408, Dec. 2012.

[36] W. Han, K. Pi, K. M. McCreary, Y. Li, J. J. I. Wong, A. G. Swartz, and R. K. Kawakami, "Tunneling Spin Injection into Single Layer Graphene," *Phys. Rev. Lett.*, vol. 105, p. 167202, Oct. 2010.

[37] P. J. Zomer, M. H. D. Guimarães, N. Tombros, and B. J. van Wees, "Long-distance spin transport in high-mobility graphene on hexagonal boron nitride," *Phys. Rev. B*, vol. 86, p. 161416, Oct. 2012.

[38] T. Yamaguchi, Y. Inoue, S. Masubuchi, S. Morikawa, M. Onuki, K. Watanabe, T. Taniguchi, R. Moriya, and T. Machida, "Electrical Spin Injection into Graphene through Monolayer Hexagonal Boron Nitride," *Applied Physics Express*, vol. 6, no. 7, p. 73001, 2013.

[39] W. Fu, P. Makk, R. Maurand, M. Bräuninger, and C. Schönenberger, "Large-scale fabrication of BN tunnel barriers for graphene spintronics," *Journal of Applied Physics*, vol. 116, p. 074306, Aug. 2014.

[40] A. L. Friedman, O. M. J. van 't Erve, C. H. Li, J. T. Robinson, and B. T. Jonker, "Homoepitaxial tunnel barriers with functionalized graphene-on-graphene for charge and spin transport.," *Nature communications*, vol. 5, p. 3161, Jan. 2014.

[41] W. H. Wang, W. Han, K. Pi, K. M. McCreary, F. Miao, W. Bao, C. N. Lau, and R. K. Kawakami, "Growth of atomically smooth MgO films on graphene by molecular beam epitaxy," *Applied Physics Letters*, vol. 93, pp. 2006–2009, 2008.

[42] J. Martin, N. Akerman, G. Ulbricht, T. Lohmann, J. H. Smet, K. von Klitzing, and A. Yacoby, "Observation of electron-hole puddles in graphene using a scanning single-electron transistor," *Nat Phys*, vol. 4, pp. 144–148, Feb. 2008.

[43] D. R., Y. F., MericI., LeeC., WangL., SorgenfreiS., WatanabeK., TaniguchiT., KimP., S. L., and HoneJ., "Boron nitride substrates for high-quality graphene electronics," *Nat Nano*, vol. 5, pp. 722–726, Oct. 2010.

[44] M. H. D. Guimarães, A. Veligura, P. J. Zomer, T. Maassen, I. J. Vera-Marun, N. Tombros, and B. J. van Wees, "Spin transport in high-quality suspended graphene devices.," *Nano letters*, vol. 12, pp. 3512–7, July 2012.

[45] F. Volmer, M. Wolter, K. Watanabe, T. Taniguchi, C. Stampfer, and B. Beschoten, "Nanosecond Spin Lifetimes in Single- and Few-Layer Graphene hBN Heterostructures at Room Temperature," *Nano Letters*, vol. 14, no. 11, pp. 1–6, 2014.

[46] S. Takahashi and S. Maekawa, "Spin injection and detection in magnetic nanostructures," *Phys. Rev. B*, vol. 67, p. 52409, Feb. 2003.

[47] W. Han, K. Pi, W. Bao, K. M. McCreary, Y. Li, W. H. Wang, C. N. Lau, and R. K. Kawakami, "Electrical detection of spin precession in single layer graphene spin valves with transparent contacts," *Applied Physics Letters*, vol. 94, no. 22, p. 222109, 2009.

[48] R. Nouchi, T. Saito, and K. Tanigaki, "Determination of Carrier Type Doped from Metal Contacts to Graphene by Channel-Length-Dependent Shift of Charge Neutrality Points," *Applied Physics Express*, vol. 4, no. 3, p. 35101, 2011.

[49] M. T. Bryan, D. Atkinson, and R. P. Cowburn, "Experimental study of the influence of edge roughness on magnetization switching in Permalloy nanostructures," *Applied Physics Letters*, vol. 85, no. 16, pp. 3510–3512, 2004.

[50] H. Alles, J. Aarik, J. Kozlova, A. Niilisk, R. Rammula, and V. Sammelselg, "Atomic layer deposition of high-k oxides on graphene," *ArXiv e-prints*, Sept. 2011.

[51] N. Tombros, S. Tanabe, A. Veligura, C. Jozsa, M. Popinciuc, H. T. Jonkman, and B. J. van Wees, "Anisotropic Spin Relaxation in Graphene," *Phys. Rev. Lett.*, vol. 101, p. 46601, July 2008.

[52] M. Popinciuc, C. Józsa, P. J. Zomer, N. Tombros, A. Veligura, H. T. Jonkman, and B. J. van Wees, "Electronic spin transport in graphene field-effect transistors," *Phys. Rev. B*, vol. 80, p. 214427, Dec. 2009.

[53] R. Hubert and A. Schäfer, *Mgnetic Domains*. Springer Berlin Heidelberg, 1998.

[54] V. Cambel, P. Eliáš, D. Gregušová, J. Martaus, J. Fedor, G. Karapetrov, and V. Novosad, "Magnetic elements for switching magnetization magnetic force microscopy tips," *Journal of Magnetism and Magnetic Materials*, vol. 322, no. 18, pp. 2715–2721, 2010.

[55] M. T. Bryan, D. Atkinson, and R. P. Cowburn, "Edge roughness and coercivity in magnetic nanostructures," *Journal of Physics: Conference Series*, vol. 17, pp. 40–44, 2005.

[56] M. Li, Y.-P. Zhao, G.-C. Wang, and H.-G. Min, "Effect of surface roughness on magnetization reversal of Co films on plasma-etched Si(100) substrates," *Journal of Applied Physics*, vol. 83, no. 100, p. 6287, 1998.

[57] Y. P. Zhao, R. M. Gamache, G. C. Wang, T. M. Lu, G. Palasantzas, and J. T. M. De Hosson, "Effect of surface roughness on magnetic domain wall thickness, domain size, and coercivity," *Journal of Applied Physics*, vol. 89, no. 2001, pp. 1325–1330, 2001.

[58] M. Zhu and R. D. McMichael, "Modification of edge mode dynamics by oxidation in Ni80 Fe 20 thin film edges," *Journal of Applied Physics*, vol. 107, no. 2010, 2010.

[59] A. Varykhalov, M. R. Scholz, T. K. Kim, and O. Rader, "Effect of noble-metal contacts on doping and band gap of graphene," *Phys. Rev. B*, vol. 82, p. 121101, Sept. 2010.

[60] F. Volmer, M. D. ogeler, T. Pohlmann, G. G. ntherodt, C.Stampfer, and B. Beschoten, "spin transport measurements in Co / MgO / graphene devices," *ArXiv e-prints*.

[61] F. L. Bakker, A. Slachter, J. P. Adam, and B. J. Van Wees, "Interplay of peltier and seebeck effects in nanoscale nonlocal spin valves," *Physical Review Letters*, vol. 105, pp. 1–4.

[62] T. Naydenova, P. Dürrenfeld, K. Tavakoli, N. Pégard, L. Ebel, K. Pappert, K. Brunner, C. Gould, and L. W. Molenkamp, "Diffusion thermopower of (Ga,Mn)As/GaAs tunnel junctions," *Physical Review Letters*, vol. 107, no. November, pp. 1–5, 2011.

[63] H. K. Onnes, "The resistance of pure mercury at helium temperatures," *Commun. Phys. Lab. Univ. Leiden*, vol. 12, no. 120, p. 1, 1911.

[64] J. Bardeen, L. N. Cooper, and J. R. Schrieffer, "Theory of Superconductivity," *Phys. Rev.*, vol. 108, pp. 1175–1204, Dec. 1957.

[65] H. B. Heersche, P. J. Herrero, J. B. Oostinga, L. M. K. Vandersypen, and A. F. Morpurgo, "Bipolar supercurrent in graphene," *Nature*, vol. 446, pp. 56–59, Mar. 2007.

[66] X. Du, I. Skachko, and E. Y. Andrei, "Josephson current and multiple Andreev reflections in graphene SNS junctions," *Phys. Rev. B*, vol. 77, p. 184507, May 2008.

[67] P. M. Tedrow and R. Meservey, "Spin-dependent tunneling into ferromagnetic nickel," *Physical Review Letters*, vol. 26, no. 4, pp. 192–195, 1971.

[68] F. Hübler, M. J. Wolf, D. Beckmann, and H. v. Löhneysen, "Long-Range Spin-Polarized Quasiparticle Transport in Mesoscopic Al Superconductors with a Zeeman Splitting," *Physical Review Letters*, vol. 109, p. 207001, Nov. 2012.

[69] H. Yang, S.-H. Yang, S. Takahashi, S. Maekawa, and S. S. P. Parkin, "Extremely long quasiparticle spin lifetimes in superconducting aluminium using MgO tunnel spin injectors.," *Nature materials*, vol. 9, pp. 586–93, July 2010.

[70] R. J. Soulen, J. M. Byers, M. S. Osofsky, B. Nadgorny, T. Ambrose, S. F. Cheng, P. R. Broussard, C. T. Tanaka, J. Nowak, J. S. Moodera, A. Barry, and J. M. D. Coey, "Measuring the Spin Polarization of a Metal with a Superconducting Point Contact," *Science*, vol. 282, pp. 85–88, Oct. 1998.

[71] S. Russo, M. Kroug, T. M. Klapwijk, and a. F. Morpurgo, "Experimental observation of bias-dependent nonlocal Andreev reflection," *Physical Review Letters*, vol. 95, no. July, pp. 1–4, 2005.

[72] D. Beckmann, E. B. Weber, and H. V. Löhneysen, "Evidence for crossed andreev reflection in superconductor-ferromagnet hybrid structures," *Physical Review Letters*, vol. 93, no. November, pp. 1–4, 2004.

[73] C. H. L. Quay, D. Chevallier, C. Bena, and M. Aprili, "Spin imbalance and spin-charge separation in a mesoscopic superconductor," *Nature Physics*, vol. 9, pp. 84–88, Jan. 2013.

[74] Tinkham, *Introduction to Superconductivity*. Dover, 2004.

[75] M. Tinkham and J. Clarke, "Theory of Pair-Quasiparticle Potential Difference in Nonequilibrium Superconductors," *Phys. Rev. Lett.*, vol. 28, pp. 1366–1369, May 1972.

[76] J. Clarke, "Experimental Observation of Pair-Quasiparticle Potential Difference in Nonequilibrium Superconductors," *Phys. Rev. Lett.*, vol. 28, pp. 1363–1366, May 1972.

[77] P. Rickhaus, M. Weiss, L. Marot, and C. Schönenberger, "Quantum Hall Effect in Graphene with Superconducting Electrodes," *Nano Letters*, vol. 12, no. 4, pp. 1942–1945, 2012.

[78] C. Ojeda-Aristizabal, M. Ferrier, S. Guéron, and H. Bouchiat, "Tuning the proximity effect in a superconductor-graphene-superconductor junction," *Phys. Rev. B*, vol. 79, p. 165436, Apr. 2009.

[79] D. Jeong, J. H. Choi, G. H. Lee, S. Jo, Y. J. Doh, and H. J. Lee, "Observation of supercurrent in PbIn-graphene-PbIn Josephson junction," *Physical Review B - Condensed Matter and Materials Physics*, vol. 83, pp. 1–5, 2011.

[80] A. Shailos, W. Nativel, A. Kasumov, C. Collet, M. Ferrier, S. Guéron, R. Deblock, and H. Bouchiat, "Proximity effect and multiple Andreev reflections in few-layer graphene," *EPL (Europhysics Letters)*, vol. 79, no. 5, p. 57008, 2007.

[81] N. Mizuno, B. Nielsen, and X. Du, "Ballistic-like supercurrent in suspended graphene Josephson weak links.," *Nature communications*, vol. 4, p. 2716, 2013.

[82] K. Grove-Rasmussen, H. I. Jø rgensen, B. M. Andersen, J. Paaske, T. S. Jespersen, J. Nygå rd, K. Flensberg, and P. E. Lindelof, "Superconductivity-enhanced bias spectroscopy in carbon nanotube quantum dots," *Phys. Rev. B*, vol. 79, p. 134518, Apr. 2009.

[83] H. I. Jø rgensen, K. Grove-Rasmussen, T. Novotný, K. Flensberg, and P. E. Lindelof, "Electron Transport in Single-Wall Carbon Nanotube Weak Links in the Fabry-Perot Regime," *Phys. Rev. Lett.*, vol. 96, p. 207003, May 2006.

[84] E. Scheer, W. Belzig, Y. Naveh, M. Devoret, D. Esteve, and C. Urbina, "Proximity Effect and Multiple Andreev Reflections in Gold Atomic Contacts," *Physical Review Letters*, vol. 86, pp. 284–287, Jan. 2001.

[85] G. E. Blonder, M. Tinkham, and T. M. Klapwijk, "Transition from metallic to tunneling regimes in superconducting microconstrictions: Excess current, charge imbalance, and supercurrent conversion," *Phys. Rev. B*, vol. 25, pp. 4515–4532, Apr. 1982.

[86] I. V. Borzenets, U. C. Coskun, S. J. Jones, and G. Finkelstein, "Phase Diffusion in Graphene-Based Josephson Junctions," *Phys. Rev. Lett.*, vol. 107, p. 137005, Sept. 2011.

[87] V. Ambegaokar and B. I. Halperin, "Voltage Due to Thermal Noise in the dc Josephson Effect," *Phys. Rev. Lett.*, vol. 22, pp. 1364–1366, June 1969.

[88] J. C. Cuevas, J. Hammer, J. Kopu, J. K. Viljas, and M. Eschrig, "Proximity effect and multiple Andreev reflections in diffusive superconductor - normal-metal - superconductor junctions," *Phys. Rev. B*, vol. 73, p. 184505, May 2006.

Acknowledgements

By finishing this thesis an important part of my life is coming to an end. This thesis would not have been possible with many people to whom I would like to convey my immense gratitude at this point.

First , I would like to thank Prof. Laurens W. Molenkamp the chair of EP3 for giving me chance to work in the group and for giving suggestions and directions during our graphene group meetings.

I also would like to thank PD Dr. Charles Gould group leader of spintronics for supervising my thesis, helping with measurement problems, commenting on this thesis and also for insisting to follow strict scientific methedology.

I owe a huge debt of gratitude to Fabian Duerr one of the graphene group member for teaching me lithography and measurement techniques and also for the discussions and suggestions related to my research. I was really lucky to start my PhD when you were around. I also would like to thank our group member Oliver Herrmann for the help and suggestions during the time of this thesis. Even though it was only for a short time, I would like to thank Dr. Jerone Ostinga for his involvement in graphene group.

Nothing in the clean room would have worked as it should be if it was not for the 'superman' of the clean room Volkmar Hock!. I was quite confident in the cleanroom when you were around and very anxious when you were not. I am thankful for the tremendous patience you have shown whenever I dropped my sample in the sputtering chamber or messed up other clean room equipments. I still remember the time when you hit the sputtering chamber at a certain corner and make it work and saved my many days of work.

I am thankful to Dr. Tanja Borzenko for helping me whenever I had problems with the e-beam system or any other clean room related troubles. You have been quite helpful whenever there was something wrong with my fabrication processes.

I would like to take this time to express my gratitude to Philip Hoffman, Dr. Tsvetelina Naydenova, Dr. Jennifer Constantino for their hospitality and all other members of EP3 for helping me out whenever I asked for it.

I also would like to thank all the professors who taught me during my school, bachelor's and Master's. I would like to thank especially Dr. Suresh, Dr Ramakrishnan, Harikrishan

sir, Dr. Sunil and Dr. Aloysius since I wouldn't be here with out their help.

I would like to thank all my malayali friends Shivaji, Neeraj for commenting on my thesis and also for the scientific, philosophical and sometimes nonsensical discussions we had over Glenfiddich and Javaanse. Also Be-joy, Rajila, Sreedhar, Anil, Thaseem and Raveesh for all those nice trips that we had and also for the traditional kerala singing parties with beef and beer. Thank you all guys!. Life in Germany would have been really "dry" without you.

A lot of thanks to my badminton mates and also my soccer mates who have kept me active even in winter. Also I would like to thank my other German friends, My roommates, Iranian friends and MSc friends Pintu, Maji, Roy and anyone else's name I have missed.

Even though they are not here, I would still like to thank my friends back home Pakku, Chekenja, Maman and all the others to avoid any complaints later!.

I have never officially thanked my family for anything in my life but I think it is time. I am in huge debt to my mother Seena and my father Suresh Babu for supporting me in all the ways they can. Also my brother Jithu and my cousins Appu, Sarima and Vismaya for standing by me and for fetching me things whenever I was back home!. I would also like to thank other members of my family for their support.

Last but not least I would like to thank my *azizam* Marjan for keeping me warm in the coldest of times.